Cascaded Quadratic Soliton Compression in Waveguide Structures.

Guo, Hairun

Publication date:
2014

Document Version
Publisher's PDF, also known as Version of record

Cascaded Quadratic Soliton Compression in Waveguide Structures

PhD Thesis by
Hairun Guo

Group of Ultrafast Nonlinear Optics
Department of Photonics Engineering
Technical University of Denmark

September 26, 2014

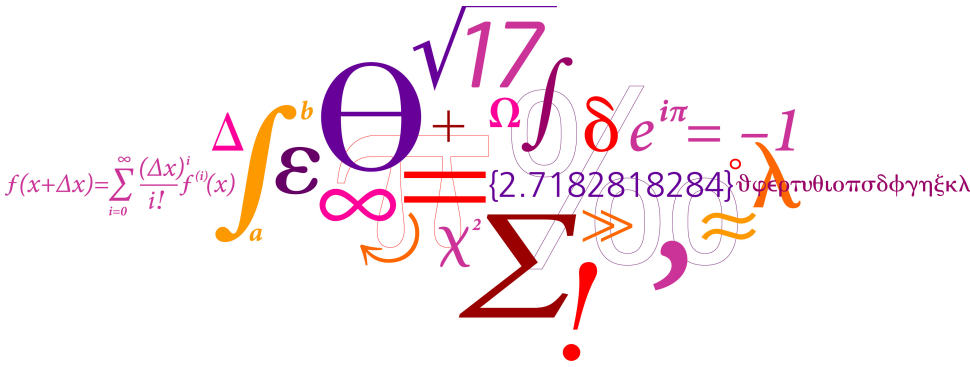

Preface

The work presented in this thesis has been carried out as my Ph.D. project in the period July 1st 2011 – June 30th 2014. The work took place at the Department of Photonics Engineering (DTU Fotonik), Technical University of Denmark. The Ph.D. project is funded by the basic funding of the Department of Photonics Engineering (DTU Fotonik) and supported by the Danish Council for Independent Research (274-08-0479, 11-106702, held by main supervisor Dr. Morten Bache) and the Marie Curie fellowship (COPULCO: 253289 held by co-supervisor Prof. Xianglong Zeng). The main supervisor Dr. Morten Bache, Associate Professor and Group Leader of the Ultrafast Nolinear Optics Group at DTU Fotonik, Technical University of Denmark. Two co-supervisors are Prof. Xianglong Zeng at Shanghai University and Dr. Binbin Zhou also from DTU Fotonik.

Acknowledgement

I would take this part to express my gratitude to those who has helped me during my Ph.D. study at DTU Fotonik.

I would first like to thank my main supervisor Prof. Morten Bache. Thank you for giving me the opportunity to work at DTU Fotonik as a Ph.D. student. Thank you for your fruitful discussions and suggestions to me always throughout the project, for your generously sharing your knowledge, and for your consistent supporting and encouragement that push me to move forward. You are a great supervisor as well as a wonderful friend. I am very happy to work with you and I do really learn a lot from you.

Warm gratitude to my co-supervisor Prof. Xianglong Zeng from Shanghai University. Thank you for recommending me to study here at Fotonik. Thank you for your insightful guidance that brings me to the nonlinear optics society and for inspiring me on a lot of research topics. It's nice to work with you during my Ph.D., especially the first two years when you also stayed at Fotonik.

Warm gratitude to my co-supervisor but also my friend Dr. Binbin Zhou. Thank you for helping me a lot on experiments, for sharing your experiences with me in the lab, and for your careful instructions to me in each experiment. I'm happy to learn experimental skills as well as tennis from you.

Many thanks to Dr. Yaohui Chen for fruitful discussions with me on Comsol simulations. Thanks to Dr. Yunhong Ding for helping me with the experiments on the Probe Station. Thanks to Dr. Xiaomin Liu for sharing me the femtosecond pulsed fiber laser during the early stage of my experiments. Thanks to Dr. Yiyu Ou for generous assistance on many things. Thanks to Prof. Ole Bang and Dr. Uffe Visbech Møller for fruitful discussions on my paper.

I would also like to thank all my friends in Denmark, colleagues in the lab and in the office. We together have spent a good time.

Last but not the least, I would like to thank my parents. Thank you for your unconditional love and support. I am sorry that I only had days with you in China in the past three years. But I hope this work will make you feel proud.

Abstract

The generation of few-cycle, high-intensity laser pulses is of great interests in a variety of research and application fields such as time-resolved spectroscopy, bio-chemical imaging with two-photon absorptions, medical treatment, material characterization, coherent supercontinuum generation and tera-hertz wave generation. Commercial pulsed lasers including the solid state system and the pulsed fiber laser have promised the generation of energetic femto-second pulses with the temporal duration around much more than tens of femto-seconds. Therefore, pulse compression technologies could be used to further push such multi-cycle pulses into few-cycle and even single-cycle.

In this thesis, we investigate the high order soliton compression in quadratic nonlinear waveguide structures, which is a one-step pulse compression scheme making use of the soliton regime – with the spontaneous cancelation between the Kerr nonlinear effects and the dispersive effects in the medium. A Kerr-like nonlinearity is produced through the cascaded phase mismatched quadratic process, e.g. the second harmonic generation process, which can be flexibly tuned in both the sign and the amplitude, making possible a strong and self-defocusing Kerr effect so that the soliton is created and the soliton self-compression happens in the normal dispersion region. Meanwhile, the chromatic dispersion in the waveguide is also tunable, understood as the dispersion engineering with structural designs. Therefore, compared to commonly used two-step compression scheme with e.g. hollow-core photonic crystal fibers plus a dispersion compensation component, our scheme, called the cascaded quadratic soliton compression (CQSC), provides a simpler setup with larger tunability on the nonlinearity, and could avoid the problem with the self-focusing Kerr effects when under the self-defocusing regime.

On the other hand, CQSC in quadratic waveguides seems highly complementary to that in quadratic bulk crystals. With bulk crystals dealing with high-energy, low-repetition-rate and large-beam-size pulses, quadratic waveguides could operate low-energy, high-repetition-rate pulsed lasers with the beam finely confined by the waveguide structure. Therefore, nano-joule, mega-hertz fiber laser pulses with $\sim$100 fs durations can be compressed to few-cycle.

We investigate quadratic waveguides with both small and large refractive index (RI) changes. Robust wafer bonding is proposed as a fabrication technology to achieve a waveguide with large RI change, which could substantively extend the guidance band of the waveguide in near- and mid-infrared ranges, and meantime evoke flexible dispersion engineering so that a broadband normal

dispersion region can be achieved.

Through numerical simulations as well as experiments, we find out that CQSC in small-RI-changed waveguides is mainly targeting the communication band in the near-infrared range, where the waveguide is naturally suitable for producing a self-defocusing Kerr-like cascaded nonlinearity so that quasi-phase-matching technology is not necessarily needed. In large-RI-changed waveguides, CQSC is extended to the mid-infrared range to generate single-cycle pulses with purely nonlinear interactions, since an all-normal dispersion profile could be achieved within the guidance band.

We believe that CQSC in quadratic waveguides is an effective pulse compression scheme with compact and simple setups, and could have potentials in many applications.

Resumé

Tilvejebringelsen af højintensitets impulser med varighed af få optiske cyklusser er af stor interesse for en mængde af forsknings- og anvendelsesområder, såsom tidsopløst spektroskopi, bio-kemisk afbildning med to-foton absorption, medicinsk behandling, karakterisering af materialer, kohærent superkontinuum generering og generering af terahertz-bølger. Kommercielle pulsede lasere inklusiv faststof-lasersystemer og pulserede fiberlasere kan give energirige femtosekund laserimpulser med tidslig varighed der er meget længere end 10 femtosekunder. Derfor kan pulskomprimeringsteknologier bruges til at bringe varigheden af sådanne multi-cyklus impulser ned til en varighed af få eller sågar en enkelt cyklisk periode af det elektromagnetiske felt.

I denne afhandling undersøger vi højere-ordens soliton pulskomprimering i kvadratisk ulineære bølgelederstrukturer. Dette er en enkelt-trins pulskomprimeringsteknik som udnytter solitonregimet, dvs. den spontane ophævelse af Kerr ulinearitetерne og de dispersive effekter i mediet. En Kerr-type ulinearitet bliver dannet gennem et fase-mismatch i en såkaldt kaskade kvadratisk ulineær proces, som fx anden-harmonisk generering, og den kan fleksibelt tunes mht. både fortegn og styrke. Dette gør det muligt at danne en kraftig selvdefokuserende Kerr ulinearitet således at solitonen kan dannes og soliton selvkomprimering kan ske i regimer med normal dispersion. På samme tid kan den kromatiske dispersion i bølgelederen også tunes, hvilket skal opfattes som tilrettelæggelse af dispersion via strukturelt design. Denne komprimeringsteknik kalder vi for "cascaded quadratic soliton compression" (CQSC), og når den sammenlignes med gængse to-trins komprimeringsteknikker, som fx hulkerne fotoniske krystalfibre plus en komponent til at kompensere for dispersionen, så vil den være enklere i opstillingen og med en større mulighed for at tune ulineariteten, og kan derfor undgå problemer med selv-fokuserende Kerr effekter ved at udnytte de selv-defokuserende effekter.

På den anden side virker CQSC i kvadratisk ulineære bølgeledere stærkt komplementære til den samme proces i kvadratiske bulk krystaller. Hvor bulk krystaller kan anvendes til impulser med høj energi, lav repetitionsrate og stor strålestørrelse, så vil kvadratiske bølgeledere kunne anvendes til impulser med lav energi, høj repetitionsrate og lille strålestørrelse omkranset af bølgelederens struktur. Derfor kan nano-Joule, mega-hertz fiberlaserimpulser med $\sim$100 fs varighed kunne komprimeres til få-cyklus varighed.

Vi undersøger kvadratiske bølgeledere med både små og store forskelle i brydningsindekset. Robust wafer bonding bliver foreslået som en fabrikation-

steknologi til at opnå en bølgeleder med en stor forskel i brydningsindekset, hvilket væsentligt vil udvide bølgelederens ledningsevne i de nær- og mellem-infrarøde områder. Samtidigt vil teknikken kunne fremkalde fleksibel tilrettelæggelse af dispersionen så normal dispersion kan opnås over et meget bredt bølgelængdeområde.

Igennem numeriske simulationer såvel som eksperimenter finder vi at CQSC i bølgeledere med en lille forskel i brydningsindeks hovedsageligt henvender sig til kommunikationsbåndet i det nær-infrarøde område, hvor bølgelederen er naturligt anlagt til at frembringe en selv-defokuserende Kerr-type kaskade ulinearitet så kvasi-fase-matche teknikker ikke nødvendigvis er krævet. I bølgeledere med store forskelle i brydningsindeks vil CQSC teknikken kunne udvides til brug i det mellem-infrarøde område, og enkelt-cyklus laserimpulser med rent ulineære vekselvirkninger kan dannes da det er muligt at designe en dispersionsprofil der kun har normal dispersion inden for det område hvor bølgelederen leder tabsfrit.

Vi føler at CQSC teknikken i kvadratisk ulineære bølgeledere er en effektiv pulskomprimeringsteknik som har en kompakt og enkel opstilling, og som har mange anvendelsesmuligheder.

Contents

Chapter 1

Introduction

1.1 Project Background

In the field of laser physics, the working mode of pulsed lasers implies that light energy can be packaged in a short time period so that the pulse peak intensity is much increased, compared to the continuous mode (i.e. the continuous-wave (CW) laser) on the same energy level [1, 2]. The minimal limitation of the pulse duration is one optical cycle, which is the time period $\tau = \lambda/c$ (where λ is the laser wavelength and c is the speed of light in vacuum). In near- and mid-infrared ranges, the generation of few-cycle laser pulses is of great interests as the pulse duration will be on the level of sub-ten femto-seconds (fs, 10^{-15} s) and the peak intensity could be up to 1 TW/cm^2 (TW, 10^{12} W), which is attractive in a variety of research and application fields including: 1) highly time-resolved spectroscopy where the femto-second laser pulse is used to probe the molecular vibrational mode [3–7]; 2) precise bio-chemical microscopy with tissues' multi-photon absorptions induced by high-intensity pulses [8–12]; 3) novel nonlinear optics where material higher order nonlinear responses could be excited; 4) laser micro-machining and sculpturing [13]; and 5) medical treatment such as the laser birthmark removal [14] and the laser-assisted in situ keratomileusis (LASIK) [15–17]. In frequency domain, such ultrashort pulses usually correspond to a broadband spectrum spanning hundreds of tera-hertz (THz, 10^{12} Hz), which is referred as the 6) supercontinuum generation (SCG) [18, 19]. Meanwhile, femto-second laser pulses are also applied in 7) the THz-wave generation [20, 21].

Nowadays, commercial solid-state laser systems, e.g. a titanium-sapphire (Ti:sapphire) laser followed by an optical parametric amplifier (OPA) [22, 23], have promised the generation of energetic femto-second laser pulses, with the tunability on laser wavelengths in near- and mid-infrared ranges. But the pulse duration is around sub-hundred femto-seconds, limited by the performance of the saturable absorber when making the mode-locking [24–28], and by the working bandwidth of the optical parametrical process [29, 30].

Temporal pulse compression [31–33] is then proposed as an subsequent scheme in order to push such multi-cycle pulses into few-cycle [34, 35], and as a result of energy conservation, the pulse peak intensity will be further increased. The image of the pulse compression is to slow down the leading edge of the pulse while speeding up the ending edge, during the pulse propagation. Physically, two components are required to compress an un-chirped pulse (the pulse with flat phase spectrum): 1) the frequency chirping process with which

the pulse spectrum will be broadened and the pulse leading and ending edges will be cast to different frequencies (i.e. a chirped pulse is formed); and 2) the group velocity dispersion (GVD) component under which light at different frequencies will have different group velocities, so the pulse shape can be manipulated (compressed). In practice, the frequency chirping is always achieved by the cubic Kerr nonlinearity produced by the material, which induces an intensity-related phase change (or refractive index (RI) change) and therefore chirps the pulse, known as the self-phase modulation (SPM) effects. When the pulse chirp is totally compensated by the GVD, the broadened spectrum actually indicates a shortened pulse duration, according to the bandwidth limit of the Fourier transform.

There are several schemes to accomplish the pulse compression, most of them are in the two-step process in accordance to the two components. For example, pulse compression with hollow-core photonic crystal fibers (PCFs) is a popular scheme [36–40] where the PCF is properly designed to first accomplish an ideal frequency chirping on pulses, namely a pulse spectral broadening with high coherence, broad bandwidth and purely linear chirp profile. Then in the second step, common optical devices with suitable GVD, such as a pair of diffraction gratings (a grating compressor), a prism pair, a chirped mirror or a chirped fiber Bragg grating, can be used to compensate the pulse chirp and accomplish the compression.

Besides, there is also a one-step scheme to accomplish the pulse compression, called the high order soliton compression [41–45], in which the GVD is inherently provided by the material or the fiber, and spontaneously compensates the frequency chirping during the pulse propagation. Soliton is studied and successfully explained soon after its discovery. It is described as a self-reinforcing and solitary wave packet formed with the cancelation of the dispersive and nonlinear effects in the medium. Moreover, if the nonlinearity is scaled larger than the dispersion (saying the dispersion length is longer than the nonlinearity length), high order solitons are formed which will experience a self-compression stage when being propagated. Also in PCFs, bright soliton pulses can be observed in the anomalous GVD region, and high-intensity pulses supported by the hollow-core PCF [46] could form a high order soliton and excite the soliton self-compression. In the normal GVD region, however, fibers will not support solitons but only give rise to the frequency chirping, so the two-step scheme is required to accomplish the compression. A smart design is the gas-filled

Kagomé hollow-core PCF [47–52], where the Kerr nonlinearity as well as the GVD profile of the fiber can be flexibly tuned by tuning the gas pressure or temperature. Therefore, both the one-step compression scheme in the soliton regime and the two-step scheme with normal GVD can be accomplished in the same setup. In fact, PCFs are becoming more and more relied on for supporting the soliton regime, finding applications of the pulse compression as well as the SCG (which is in the much higher order soliton regime), as they could enable precise and large tunability on the GVD profile, while still providing good confinement and guidance on the laser beam. Moreover, the synthesis of novel materials such as chalcogenides (e.g. As_2S_3) [53–58], fluoride glasses (e.g. ZBLAN) [59–62], tellurite [63–66] and heavy oxides could provide stronger Kerr nonlinearities and wider transparency windows in near- and mid-infrared ranges than the silica glass, making the fiber device quite compact with only centimeter lengths [67].

However, the material intrinsic cubic Kerr nonlinearity is always spatially self-focusing, which means the laser spatial beam will be self-compressed as well. This might give an opportunity to simultaneously accomplish both the spatial and the temporal pulse compression [68], but it also raises the risk of the pulse filamentation under a certain energy [69], which is a phenomenon that the laser beam spot becomes split with some fractions having extremely increased intensities. Filamentation is obviously unwanted as the unexpected high intensity may touch the damage threshold of the fiber material [70] or excite plasma (a much complicated and disturbing nonlinear process) in air or gases [71, 72].

1.1.1 Cascaded Quadratic Nonlinearity

On the other hand, in quadratic nonlinear crystals, the Kerr-like nonlinear effects was also demonstrated, during the cascaded phase mismatched process [73–75].

Normally, quadratic crystals are always used in applications of frequency conversions, such as the second harmonic generation (SHG) [76], the sum frequency generation (SFG) or the different frequency generation (DFG), which are in general called the three wave mixing processes (TWM). They are also basic components in achieving the optical parametrical processes leading to optical parametrical oscillators (OPOs) and OPAs. Phase matching is always required in these processes so that light energy can be continuously converted

to new frequencies [77]. Therefore, the crystal is always carefully configured, either by being precisely cut or tuning the angle (see. chapter B) to meet a critical phase matching condition between two axes of the birefringence [78], or through tuning the temperature or making use of quasi-phase-matching (QPM) technologies [79] to achieve a non-critical phase matching.

However, when e.g. the SHG is phase mismatched, the energy conversion between the fundamental wave (FW) and the second harmonic (SH) will become weak and periodically repeated, called the cascaded process, which means the SH that being converted from the FW will back convert. Although the FW can be considered un-depleted as the SH energy is very low, the repeated conversions and back conversions will gradually change the phase of the FW, giving rise to an intensity-related nonlinear phase shift, just like the cubic Kerr nonlinearity. Such a nonlinear response is called the cascaded quadratic nonlinearity.

Careful studies show that the cascaded quadratic nonlinearity is not purely instantaneous but in fact a delayed response [80], which can be separated into direct current (DC) component, first-order component and higher-order components [81, 82]. It is the DC component that exactly giving rise to the Kerr effects, to the frequency chirping, and namely to the SPM. The first-order component is corresponding to the self-steepening effects, which causes shock front on pulse shapes and asymmetry in the pulse spectrum.

More importantly, it was revealed that the cascaded quadratic nonlinearity can be flexibly tuned in both the amplitude and the sign, by tuning the phase mismatch parameter [73], making the Kerr effects strong or weak, self-focusing or self-defocusing. Meanwhile, the cascading induced self-steepening effects is also tunable in which the pulse shock front as well as the spectral asymmetry can be totally turned over [83]. Hence, the tunability in the cascaded quadratic nonlinearity is much larger than that in the gas in hollow-core PCFs.

On the other hand, high-order components of the cascaded response may also come up if the phase mismatch is tuned into a so-called non-stationary region [81, 84]. There the response spectrum will show divergent peaks which means strong and narrow-band resonant radiations will be stimulated that continuously transfer energy from the FW. Remaining in the stationary region, on the contrary, the cascaded response will be broadband and convergent.

Nowadays, cascading induced Kerr-like effects as well as the self-steepening effects has been widely applied in e.g. the self-defocusing pulse compression

[85–89], the SCG [89–92], the frequency comb generation [93, 94], the soliton mode-locking with normal GVD [95], the compensation of self-focusing Kerr nonlinearity [96] and the controlling of the pulse self-steepening performances [83].

1.1.2 Cascaded Quadratic Soliton Compression (CQSC)

Using the cascaded quadratic nonlinearity for pulse compressions can be both in the two-step process [87] and in the one-step process of the high order soliton compression. The latter is also called the *cascaded quadratic soliton compression (CQSC)*. Especially, it is attractive that the self-defocusing Kerr-like effects could be used so that problems with the self-focusing effects can be avoided. Meanwhile, crystals are known to have much higher damage thresholds than glasses, so ultra-high-intensity pulses can be operated in the CQSC. The self-defocusing Kerr effects also implies that the pulse compression is accomplished with the normal GVD, in oppose to cases in cubic Kerr materials.

In recent years, great progresses have been made in the CQSC in bulk crystals. For example: 1) energetic, few-cycle pulse compressions have been experimentally demonstrated in the near-infrared in crystals barium borate (BBO) [85,86] and lithium niobate (LN) [89]; 2) cascading induced pulse spectral broadening to octave-spanning SCGs has been observed in the mid-infrared range in the crystal lithium thioindate (LIS) [97]; 3) possible crystal materials and semiconductors that could provide a dominant self-defocusing cascaded nonlinearity have been reviewed and the operational wavelength range was revealed to be widely spread in near- and mid-infrared ranges [98]; and so on. The crystal is always compact with small lengths as the quadratic nonlinear susceptibility is quite large, promising a stronger cascaded Kerr-like nonlinearity than most Kerr materials.

The discovery of the cascaded quadratic nonlinearity as well as the CQSC is also meaningful to the nonlinear optics society as it opens our mind and extends the applications of quadratic nonlinear crystals and semiconductors, from traditional frequency conversions with restricted phase matching conditions to the quite general and broadband operational CQSCs.

However, the problem with the self-defocusing Kerr effects is that the laser beam will gradually get enlarged, in oppose to the self-focusing effects, and aggravate the spatial diffraction effects. Therefore, the effective length of the laser-crystal interaction is actually shortened. The crystal length is then sug-

gested to be shorter than the diffraction length of the laser beam (depth of focus of a gaussian beam). The input laser should also have a large beam spot so as to avoid the spatio-temporal effects when few-cycle pulses are generated.

1.2 Project Description

Therefore, based on above backgrounds, we propose the project "cascaded quadratic soliton compression in waveguide structures". The idea is to transplant the CQSC from a bulk crystal to a quadratic waveguide – an optical waveguide structure with materials having quadratic nonlinearities. Using waveguide is a good solution to overcome the spatial diffraction effects. It could also suppress the spatio-temporal effects as light is now propagated in forms of waveguide eigen-modes. Therefore, the interaction length between the laser and the crystal material could be increased, which enables the compression of long pulses that usually requires long crystal lengths.

We are aware that, CQSC in quadratic waveguides is highly complementary to that in bulk crystals. While bulk crystals are used to compress high-energy (1 μJ $\sim$ multiple milli-joules), low-repetition-rate, and large-beam-size laser pulses, quadratic waveguides could handle low-energy pulses (sub-nJ to tens nJ) with still ultra-high intensities as the beam size is highly compact in the waveguide core. Such features as low energy and fine confinement also enable the pulsed laser to have high repetition rate, implying the compression targeting nano-joule, mega-hertz, femto-second pulsed fiber lasers. Moreover, dispersion engineering is possible in quadratic waveguides, analogous to the function of PCFs, through the proper design of the waveguide structure, with which the GVD profile (more precisely, the waveguide dispersion profile) can be flexibly tailored instead of being fixed by the material dispersion in the bulk crystal. On the other hand, unlike simple light-crystal interactions in bulk crystals, nonlinear intra-mode interactions are evoked in quadratic waveguides, as multiple eigen-modes are always supported in high harmonics at high frequencies (short wavelengths).

In fact, quadratic waveguides have been well known and widely applied for decades. They are always used in integrated waveguide optics and optical communications for the purpose of frequency conversions [99], such as the DFG [100] and OPO, just like bulk crystals but with the operational wavelength or working bandwidth extended due to the dispersion engineering. Meanwhile,

they are also being studied for cascading [101,102], paving a way to the accomplishment of CQSC.

Usually, quadratic waveguides are fabricated by means of annealed proton exchange (APE) or Ti in-diffusion [103,104], which chemically diffuses dopants on the surface of a crystal (used as substrate) and form a channel with higher RI so that the laser light can be guided inside. The RI change between the core and the substrate in such waveguides are always small, which might limit the guidance bandwidth of the waveguide, and meanwhile, restrict the the flexibility of the dispersion engineering.

In the project, we will of course investigate the APE or Ti in-diffused quadratic waveguides as they are so commonly used and therefore worth to be demonstrated for the CQSC. But what's more important is that we will also investigate quadratic waveguides with novel fabrication technologies, e.g. the *wafer bonding* [105, 106], so that large RI change in the waveguide can be achieved. Then CQSC in quadratic waveguides will be expected to operate pulses with extended guidance bandwidth and with flexible dispersion engineering, making possible e.g. the few-cycle pulse compression in the mid-infrared range, as well as the SCG. In details, regime of the CQSC will be investigated; the physics of the nonlinear intra-mode interaction will be made clear; and self-defocusing soliton compressions in near- and mid-infrared ranges will be demonstrated through both simulations and experiments.

1.3 Achievements and Milestones

The achievements and milestones of this project are listed as follows:

- We developed a generalized numerical model, called the *nonlinear wave equation in frequency domain* (NWEF), which directly solves the dynamics of the electric field of the laser pulse when being propagated in the quadratic waveguide. All types of nonlinear interactions (SHG, DFG, SPM, Raman effects, etc.) as well as intra-mode interactions are automatically included as the equation holds the generalized and complete form of both linear and nonlinear (quadratic and cubic nonlinear) induced polarizations.

- We proposed the concept of the *soliton spectral coupling*, which gives an unified explanation to the formation of fundamental solitons, soliton

induced dispersive wave (DW) generations and soliton spectral tunneling effects (SST).

- We numerically demonstrated the CQSC in quadratic waveguides with a small RI change, with the operational wavelength range covering the communication band in the near-infrared range. In experiments, self-defocusing soliton induced SCGs were demonstrated in APE LN waveguides.

- We proposed the robust wafer bonding between the crystal and glass materials, which gives us opportunities to fabricate quadratic waveguides with large RI change. Numerical simulations proved the concept of the CQSC in such waveguides, which could actually operate laser pulses in the mid-infrared range.

1.4 Chapter Overview

After this chapter of a general introduction, in chapter 2, we will give the derivation of the numerical model NWEF which is considered as the basic simulation tool all over this thesis. Then, in chapter 3, we will review the CQSC in quadratic bulk crystals. In chapter 4, we will go through the topic CQSC in quadratic waveguides, including the waveguide mode analysis, dispersion engineering and nonlinearity estimation. Investigations cover waveguides with both small and large RI changes, and with both traditional APE structures and novel wafer bonded ridge structures. Chapter 5 gives conclusions and outlooks.

Bibliography

[1] B. Saleh and M. Teich, *Fundamentals of Photonics*, Wiley Series in Pure and Applied Optics (Wiley, 2007).

[2] J. Diels, W. Rudolph, P. Liao, and P. Kelley, *Ultrashort Laser Pulse Phenomena*, Optics and photonics (Elsevier Science, 2006).

[3] M. Groot and R. Van Grondelle, "Femtosecond time-resolved infrared spectroscopy," in "Biophysical Techniques in Photosynthesis," , vol. 26 of *Advances in Photosynthesis and Respiration*, T. J. Aartsma and J. Matysik, eds. (Springer Netherlands, 2008), pp. 191–200.

[4] L. Dhar, J. A. Rogers, and K. A. Nelson, "Time-resolved vibrational spectroscopy in the impulsive limit," Chem. Rev. **94**, 157–193 (1994).

[5] E. Tokunaga, T. Kobayashi, and A. Terasaki, "Frequency-domain interferometer for femtosecond time-resolved phase spectroscopy," Opt. Lett. **17**, 1131–1133 (1992).

[6] K. Iwata, T. Takaya, H. Hamaguchi, A. Yamakata, T. Ishibashi, H. Onishi, and H. Kuroda, "Carrier dynamics in TiO_2 and Pt/TiO_2 powders observed by femtosecond time-resolved near-infrared spectroscopy at a spectral region of 0.9-1.5 μm with the direct absorption method," J Phys. Chem. B **108**, 20233–20239 (2004).

[7] A. L. Smeigh, M. Creelman, R. A. Mathies, and J. K. McCusker, "Femtosecond time-resolved optical and raman spectroscopy of photoinduced spin crossover: Temporal resolution of low-to-high spin optical switching," J Am. Chem. Soc. **130**, 14105–14107 (2008).

[8] N. G. Horton, K. Wang, D. Kobat, C. G. Clark, F. W. Wise, C. B. Schaffer, and C. Xu, "In vivo three-photon microscopy of subcortical structures within an intact mouse brain," Nat. Photon. **7**, 205–209 (2013).

[9] K. Schenke-Layland, I. Riemann, U. A. Stock, and K. Konig, "Imaging of cardiovascular structures using near-infrared femtosecond multiphoton laser scanning microscopy," J. of Biomed. Opt. **10**, 24017(5) (2005).

[10] K. Konig, "Multiphoton microscopy in life sciences," J. Microsc. **200**, 83–104 (2000).

[11] T. Liu, S. Chu, C. Sun, B. Lin, P. Cheng, and I. Johnson, "Multiphoton confocal microscopy using a femtosecond Cr:forsterite laser," Scanning **23**, 249–254 (2001).

[12] B.-G. Wang and K.-J. Halbhuber, "Corneal multiphoton microscopy and intratissue optical nanosurgery by nanojoule femtosecond near-infrared pulsed lasers," Ann. Anat. **188**, 395–409 (2006).

[13] S. Rekštytė, M. Malinauskas, and S. Juodkazis, "Three-dimensional laser micro-sculpturing of silicone: towards bio-compatible scaffolds," Opt. Express **21**, 17028–17041 (2013).

[14] M. K. Loze and C. D. Wright, "Temperature distributions in laser-heated biological tissue with application to birthmark removal," J. Biomed. Opt. **6**, 74–85 (2001).

[15] S. G. Slade, "The use of the femtosecond laser in the customization of corneal flaps in laser in situ keratomileusis," Curr. Opin. Ophthalmol. **18**, 314–317 (2007).

[16] G. L. Sutton and P. Kim, "Laser in situ keratomileusis in 2010 – a review," Clin. Experiment. Ophthalmol. **38**, 192–210 (2010).

[17] M. Q. Salomao and S. E. Wilson, "Femtosecond laser in laser in situ keratomileusis," J. Cataract. Refract. Surg. **36**, 1024–1032 (2010).

[18] G. Agrawal, *Nonlinear Fiber Optics*, Academic Press (Academic Press, 2013).

[19] J. Dudley and J. Taylor, *Supercontinuum Generation in Optical Fibers* (Cambridge University Press, 2010).

[20] S. Fan, H. Takeuchi, T. Ouchi, K. Takeya, and K. Kawase, "Broadband terahertz wave generation from a MgO : $LiNbO_3$ ridge waveguide pumped by a 1.5 μm femtosecond fiber laser," Opt. Lett. **38**, 1654–1656 (2013).

[21] J. Li, L. Chai, J. Shi, B. Liu, B. Xu, M. Hu, Y. Li, Q. Xing, C. Wang, A. B. Fedotov, and A. M. Zheltikov, "Efficient terahertz wave generation from GaP crystals pumped by chirp-controlled pulses from femtosecond photonic crystal fiber amplifier," Appl. Phys. Lett. **104**, 031117(5) (2014).

[22] *http://www.spectra-physics.com/products/ultrafast-lasers/* (accessed June 30, 2014).

[23] *http://www.coherent.com/products/index.cfm?795/Ultrafast-Laser-Oscillators-and-Amplifiers* (accessed June 30, 2014).

[24] U. Keller, K. Weingarten, F. Kartner, D. Kopf, B. Braun, I. Jung, R. Fluck, C. Honninger, N. Matuschek, and J. derAu, "Semiconductor saturable absorber mirrors (SESAM's) for femtosecond to nanosecond pulse generation in solid-state lasers," IEEE J. Select. Topics Quantum Electron. **2**, 435–453 (1996).

[25] Q. Bao, H. Zhang, Y. Wang, Z. Ni, Y. Yan, Z. X. Shen, K. P. Loh, and D. Y. Tang, "Atomic-layer graphene as a saturable absorber for ultrafast pulsed lasers," Adv. Funct. Mater. **19**, 3077–3083 (2009).

[26] H. A. Haus, "Theory of mode locking with a fast saturable absorber," J. Appl. Phys. **46**, 3049–3058 (1975).

[27] D. Sutter, G. Steinmeyer, L. Gallmann, N. Matuschek, F. Morier-Genoud, U. Keller, V. Scheuer, G. Angelow, and T. Tschudi, "Semiconductor saturable-absorber mirror-assisted Kerr-lens mode-locked Ti:sapphire laser producing pulses in the two-cycle regime," Opt. Lett. **24**, 631–633 (1999).

[28] J. C. Antoranz, L. L. Bonilla, J. Gea, and M. G. Velarde, "Bistable limit cycles in a model for a laser with a saturable absorber," Phys. Rev. Lett. **49**, 35–38 (1982).

[29] A. Shirakawa, I. Sakane, and T. Kobayashi, "Pulse-front-matched optical parametric amplification for sub-10-fs pulse generation tunable in the visible and near infrared," Opt. Lett. **23**, 1292–1294 (1998).

[30] V. Petrov, F. Noack, and R. Stolzenberger, "Seeded femtosecond optical parametric amplification in the mid-infrared spectral region above 3 μm," Appl. Opt. **36**, 1164–1172 (1997).

[31] E. B. Treacy, "Optical pulse compression with diffraction gratings," IEEE J. Quantum Electron. **QE-5**, 454–458 (1969).

[32] L. F. Mollenauer, R. H. Stolen, and J. P. Gordon, "Experimental observation of picosecond pulse narrowing and solitons in optical fibers," Phys. Rev. Lett. **45**, 1095–1098 (1980).

[33] C. V. Shank, R. L. Fork, R. Yen, R. H. Stolen, and W. J. Tomlinson, "Compression of femtosecond optical pulses," Appl. Phys. Lett. **40**, 761–763 (1982).

[34] A. Baltuska, Z. Wei, M. S. Pshenichnikov, and D. A. Wiersma, "Optical pulse compression to 5 fs at a 1-MHz repetition rate," Opt. Lett. **22**, 102–104 (1997).

[35] M. Nisoli, S. D. Silvestri, O. Svelto, R. Szipöcs, K. Ferencz, C. Spielmann, S. Sartania, and F. Krausz, "Compression of high-energy laser pulses below 5 fs," Opt. Lett. **22**, 522–524 (1997).

[36] F. Gerome, K. Cook, A. K. George, W. J. Wadsworth, and J. C. Knight, "Delivery of sub-100 fs pulses through 8 m of hollow-core fiber using soliton compression," Opt. Express **15**, 7126–7131 (2007).

[37] L. Gallmann, T. Pfeifer, P. M. Nagel, M. J. Abel, D. M. Neumark, and S. R. Leone, "Comparison of the filamentation and the hollow-core fiber characteristics for pulse compression into the few-cycle regime," Appl. Phys. B Lasers Opt. **86**, 561–566 (2007).

[38] J. Laegsgaard and P. J. Roberts, "Dispersive pulse compression in hollow-core photonic bandgap fibers," Opt. Express **16**, 9628–9644 (2008).

[39] P. Bejot, B. E. Schmidt, J. Kasparian, J. P. Wolf, and F. Legare, "Mechanism of hollow-core-fiber infrared-supercontinuum compression with bulk material," Phys. Rev. A **81**, 063828(6) (2010).

[40] Y. Y. Wang, X. Peng, M. Alharbi, C. F. Dutin, T. D. Bradley, F. Gerome, M. Mielke, T. Booth, and F. Benabid, "Design and fabrication of hollow-core photonic crystal fibers for high-power ultrashort pulse transportation and pulse compression," Opt. Lett. **37**, 3111–3113 (2012).

[41] S. V. Chernikov, E. M. Dianov, D. J. Richardson, and D. N. Payne, "Soliton pulse compression in dispersion-decreasing fiber," Opt. Lett. **18**, 476–478 (1993).

[42] I. Koprinkov, A. Suda, P. Wang, and K. Midorikawa, "Self-compression of high-intensity femtosecond optical pulses and spatiotemporal soliton generation," Phys. Rev. Lett. **84**, 3847–3850 (2000).

[43] P. Colman, C. Husko, S. Combrie, I. Sagnes, C. W. Wong, and A. De Rossi, "Temporal solitons and pulse compression in photonic crystal waveguides," Nat. Photon. **4**, 862–868 (2010).

[44] S. A. Skobelev, D. V. Kartashov, and A. V. Kim, "Few-optical-cycle solitons and pulse self-compression in a Kerr medium," Phys. Rev. Lett. **99**, 203902(4) (2007).

[45] M. V. Tognetti and H. M. Crespo, "Sub-two-cycle soliton-effect pulse compression at 800 nm in photonic crystal fibers," J. Opt. Soc. Am. B **24**, 1410–1415 (2007).

[46] S. Bohman, A. Suda, M. Kaku, M. Nurhuda, T. Kanai, S. Yamaguchi, and K. Midorikawa, "Generation of 5 fs, 0.5 tw pulses focusable to relativistic intensities at 1 khz," Opt. Express **16**, 10684–10689 (2008).

[47] K. F. Mak, J. C. Travers, N. Y. Joly, A. Abdolvand, and P. S. J. Russell, "Two techniques for temporal pulse compression in gas-filled hollow-core Kagomé; photonic crystal fiber," Opt. Lett. **38**, 3592–3595 (2013).

[48] X. Chen, A. Jullien, A. Malvache, L. Canova, A. Borot, A. Trisorio, C. G. Durfee, and R. Lopez-Martens, "Generation of 4.3 fs, 1 mJ laser pulses via compression of circularly polarized pulses in a gas-filled hollow-core fiber," OPTICS LETTERS **34**, 1588–1590 (2009).

[49] J. C. Travers, W. Chang, J. Nold, N. Y. Joly, and P. S. J. Russell, "Ultrafast nonlinear optics in gas-filled hollow-core photonic crystal fibers [invited]," J. Opt. Soc. Am. B **28**, A11–A26 (2011).

[50] O. H. Heckl, C. J. Saraceno, C. R. E. Baer, T. Suedmeyer, Y. Y. Wang, Y. Cheng, F. Benabid, and U. Keller, "Temporal pulse compression in a xenon-filled Kagomé-type hollow-core photonic crystal fiber at high average power," Opt. Express **19**, 19142–19149 (2011).

[51] F. Emaury, C. F. Dutin, C. J. Saraceno, M. Trant, O. H. Heckl, Y. Y. Wang, C. Schriber, F. Gerome, T. Suedmeyer, F. Benabid, and U. Keller, "Beam delivery and pulse compression to sub-50 fs of a modelocked thin-disk laser in a gas-filled Kagomé-type HC-PCF fiber," Opt. Express **21**, 4986–4994 (2013).

[52] G. Epple, K. S. Kleinbach, T. G. Euser, N. Y. Joly, T. Pfau, P. S. J. Russell, and R. LÃűw, "Rydberg atoms in hollow-core photonic crystal fibres," Nat. Commun. **5**, 4132 (2014).

[53] I. D. Aggarwal and J. S. Sanghera, "Active and passive chalcogenide glass optical fibers for IR applications: A review," J. Non-Cryst. Solids **256**, 6–16 (1999).

[54] J. S. Sanghera, L. B. Shaw, and I. D. Aggarwal, "Chalcogenide glass-fiber-based mid-IR sources and applications," IEEE J. Sel. Topics Quantum Electron. **15**, 114–119 (2009).

[55] M. El-Amraoui, J. Fatome, J. C. Jules, B. Kibler, G. Gadret, C. Fortier, F. Smektala, I. Skripatchev, C. F. Polacchini, Y. Messaddeq, J. Troles, L. Brilland, M. Szpulak, and G. Renversez, "Strong infrared spectral broadening in low-loss As-S chalcogenide suspended core microstructured optical fibers," Opt. Express **18**, 4547–4556 (2010).

[56] M. Liao, C. Chaudhari, G. Qin, X. Yan, C. Kito, T. Suzuki, Y. Ohishi, M. Matsumoto, and T. Misumi, "Fabrication and characterization of a chalcogenide-tellurite composite microstructure fiber with high nonlinearity," Opt. Express **17**, 21608–21614 (2009).

[57] M. El-Amraoui, G. Gadret, J. C. Jules, J. Fatome, C. Fortier, F. Desevedavy, I. Skripatchev, Y. Messaddeq, J. Troles, L. Brilland, W. Gao, T. Suzuki, Y. Ohishi, and F. Smektala, "Microstructured chalcogenide optical fibers from as2s3 glass: towards new ir broadband sources," Opt. Express **18**, 26655–26665 (2010).

[58] N. Granzow, P. Uebel, M. A. Schmidt, A. S. Tverjanovich, L. Wondraczek, and P. S. J. Russell, "Bandgap guidance in hybrid chalcogenide-silica photonic crystal fibers," Opt. Lett. **36**, 2432–2434 (2011).

[59] C. Xia, M. Kumar, O. R. Kulkarni, M. N. Islam, F. L. Terry, and M. J. Freeman, "Mid-infrared supercontinuum generation to 4.5 μm in ZBLAN fluoride fibers by nanosecond diode pumping," Opt. Lett. **31**, 2553–2555 (2006).

[60] O. P. Kulkarni, V. V. Alexander, M. Kumar, M. J. Freeman, M. N. Islam, F. L. Terry, M. Neelakandan, and A. Chan, "Supercontinuum generation from similar to 1.9 to 4.5 μm in ZBLAN fiber with high average power generation beyond 3.8 μm using a thulium-doped fiber amplifier," J. Opt. Soc. Am. B **28**, 2486–2498 (2011).

[61] C. Xia, M. Kumar, M.-Y. Cheng, R. S. Hegde, M. N. Islam, A. Galvanauskas, H. G. Winful, F. L. Terry, M. J. Freeman, M. Poulain, and G. Maze, "Power scalable mid-infrared supercontinuum generation in

ZBLAN fluoride fibers with up to 1.3 watts time-averaged power," Opt. Express **15**, 865–871 (2007).

[62] Z. Chen, A. J. Taylor, and A. Efimov, "Coherent mid-infrared broadband continuum generation in non-uniform ZBLAN fiber tap," Opt. Express **17**, 5852–5860 (2009).

[63] P. Domachuk, N. A. Wolchover, M. Cronin-Golomb, A. Wang, A. K. George, C. M. B. Cordeiro, J. C. Knight, and F. G. Omenetto, "Over 4000 nm bandwidth of mid-IR supercontinuum generation in sub-centimeter segments of highly nonlinear tellurite PCFs," Opt. Express **16**, 7161–7168 (2008).

[64] M. Arnaudov, V. Dimitrov, Y. Dimitriev, and L. Markova, "Infrared spectral investigation of tellurites," Mater. Res. Bull. **17**, 1121–1129 (1982).

[65] L. Huang, A. Jha, S. Shen, and X. Liu, "Broadband emission in $Er^{3+} - Tm^{3+}$ codoped tellurite fibre," Opt. Express **12**, 2429–2434 (2004).

[66] X. Feng, W. H. Loh, J. C. Flanagan, A. Camerlingo, S. Dasgupta, P. Petropoulos, P. Horak, K. E. Frampton, N. M. White, J. H. V. Price, H. N. Rutt, and D. J. Richardson, "Single-mode tellurite glass holey fiber with extremely large mode area for infrared nonlinear applications," Opt. Express **16**, 13651–13656 (2008).

[67] O. Mouawad, J. Picot-Clemente, F. Amrani, C. Strutynski, J. Fatome, B. Kibler, F. Desevedavy, G. Gadret, J. C. Jules, D. Deng, Y. Ohishi, and F. Smektala, "Multioctave midinfrared supercontinuum generation in suspended-core chalcogenide fibers," Opt. Lett. **39**, 2684–2687 (2014).

[68] W. H. Renninger and F. W. Wise, "Optical solitons in graded-index multimode fibres," Nat. Commun. **4**, 1719 (2013).

[69] A. Couairon and A. Mysyrowicz, "Femtosecond filamentation in transparent media," Physics Reports **441**, 47–189 (2007).

[70] A. Couairon, L. Sudrie, M. Franco, B. Prade, and A. Mysyrowicz, "Filamentation and damage in fused silica induced by tightly focused femtosecond laser pulses," Phys. Rev. B **71**, 125435 (2005).

[71] A. Couairon, M. Franco, A. Mysyrowicz, J. Biegert, and U. Keller, "Pulse self-compression to the single-cycle limit by filamentation in a gas with a pressure gradient," Opt. Lett. **30**, 2657–2659 (2005).

[72] P. HoÌĹlzer, W. Chang, J. C. Travers, A. Nazarkin, J. Nold, N. Y. Joly, M. F. Saleh, F. Biancalana, and P. S. J. Russell, "Femtosecond nonlinear fiber optics in the ionization regime," Phys. Rev. Lett. **107**, 203901 (2011).

[73] R. DeSalvo, H. Vanherzeele, D. J. Hagan, M. Sheik-Bahae, G. Stegeman, and E. W. V. Stryland, "Self-focusing and self-defocusing by cascaded second-order effects in KTP," Opt. Lett. **17**, 28–30 (1992).

[74] M. L. Sundheimer, J. D. Bierlein, C. Bosshard, E. W. V. Stryland, and G. I. Stegeman, "Large nonlinear phase modulation in quasi-phase-matched KTP waveguides as a result of cascaded second-order processes," Opt. Lett. **18**, 1397–1399 (1993).

[75] G. I. Stegeman, M. Sheik-Bahae, E. V. Stryland, and G. Assanto, "Large nonlinear phase shifts in second-order nonlinear-optical processes," Opt. Lett. **18**, 13–15 (1993).

[76] P. A. Franken, A. E. Hill, C. W. Peters, and G. Weinreich, "Generation of optical harmonics," Phys. Rev. Lett. **7**, 118–119 (1961).

[77] R. Boyd, *Nonlinear Optics*, Nonlinear Optics Series (Elsevier Science, 2008).

[78] A. Fiore, V. Berger, E. Rosencher, P. Bravetti, and J. Nagle, "Phase matching using an isotropic nonlinear optical material," Nature **391**, 463–466 (1998).

[79] M. M. Fejer, G. A. Magel, D. H. Jundt, and R. L. Byer, "Quasi-phase-matched second harmonic generation: tuning and tolerances," IEEE J. Quantum Electron. **28**, 2631–2654 (1992).

[80] G. Valiulis, V. Jukna, and O. Jedrkiewicz, "Propagation dynamics and X-pulse formation in phase-mismatched second-harmonic generation." Phys. Rev. A **83**, 43834(14) (2011).

[81] M. Bache, O. Bang, and W. Krolikowski, "Limits to compression with cascaded quadratic soliton compressors," Optics Express **16**, 3273–3287 (2008).

[82] H. Guo, X. Zeng, B. Zhou, and M. Bache, "Soliton delay driven by cascading and Raman responses," in "2013 Conference on Lasers and Electro-Optics - International Quantum Electronics Conference," (Optical Society of America, 2013), p. IF_P_9.

[83] J. Moses and F. W. Wise, "Controllable self-steepening of ultrashort pulses in quadratic nonlinear media," Phys. Rev. Lett. **97**, 073903(4) (2006).

[84] M. Bache and O. Bang, "Nonlocal explanation of stationary and nonstationary regimes in cascaded soliton pulse compression," Opt. Lett. **32**, 2490–2492 (2007).

[85] S. Ashihara, J. Nishina, T. Shimura, and K. Kuroda, "Soliton compression of femtosecond pulses in quadratic media," J. Opt. Soc. Am. B **19**, 2505–2510 (2002).

[86] J. Moses and F. W. Wise, "Soliton compression in quadratic media: high-energy few-cycle pulses with a frequency-doubling crystal," Opt. Lett. **31**, 1881–1883 (2006).

[87] X. Liu, L. Qian, and F. Wise, "High-energy pulse compression by use of negative phase shifts produced by the cascade $\chi^{(2)}$:$\chi^{(2)}$ nonlinearity," Opt. Lett. **24**, 1777–1779 (1999).

[88] J. Moses, E. Alhammali, J. M. Eichenholz, and F. W. Wise, "Efficient high-energy femtosecond pulse compression in quadratic media with flat-top beams," Opt. Lett. **32**, 2469–2471 (2007).

[89] B. B. Zhou, A. Chong, F. W. Wise, and M. Bache, "Ultrafast and octave-spanning optical nonlinearities from strongly phase-mismatched quadratic interactions," Phys. Rev. Lett. **109**, 043902 (2012).

[90] T. Fuji, J. Rauschenberger, A. Apolonski, V. S. Yakovlev, G. Tempea, T. Udem, C. Gohle, T. W. Hänsch, W. Lehnert, M. Scherer, and F. Krausz, "Monolithic carrier-envelope phase-stabilization scheme," Opt. Lett. **30**, 332–334 (2005).

[91] C. R. Phillips, C. Langrock, J. S. Pelc, M. M. Fejer, I. Hartl, and M. E. Fermann, "Supercontinuum generation in quasi-phasematched waveguides," Opt. Express **19**, 18754–18773 (2011).

[92] C. R. Phillips, C. Langrock, J. S. Pelc, M. M. Fejer, J. Jiang, M. E. Fermann, and I. Hartl, "Supercontinuum generation in quasi-phase-matched $LiNbO_3$ waveguide pumped by a Tm-doped fiber laser system," Opt. Lett. **36**, 3912–3914 (2011).

[93] V. Ulvila, C. R. Phillips, L. Halonen, and M. Vainio, "High-power mid-infrared frequency comb from a continuous-wave-pumped bulk optical parametric oscillator," Opt. Express **22**, 10535–10543 (2014).

[94] V. Ulvila, C. R. Phillips, L. Halonen, and M. Vainio, "Frequency comb generation by a continuous-wave-pumped optical parametric oscillator based on cascading quadratic nonlinearities," Opt. Lett. **38**, 4281–4284 (2013).

[95] A. S. Mayer, C. R. Phillips, A. Klenner, and U. Keller, "Soliton modelocking via cascaded quadratic nonlinearities in a SESAM-modelocked Yb:CALGO laser," in "CLEO: 2014," (Optical Society of America, 2014), p. STu2E.3.

[96] C. Dorrer, R. Roides, J. Bromage, and J. D. Zuegel, "Self-phase modulation compensation in a regenerative amplifier using cascaded second-order nonlinearities," in "CLEO: 2014," (Optical Society of America, 2014), p. STu3I.1.

[97] B. Zhou, H. Guo, X. Liu, and M. Bache, "Octave-spanning mid-IR supercontinuum generation with ultrafast cascaded nonlinearities," in "CLEO: 2014," (Optical Society of America, 2014), p. JTu4A.24.

[98] M. Bache, H. Guo, and B. Zhou, "Generating mid-IR octave-spanning supercontinua and few-cycle pulses with solitons in phase-mismatched quadratic nonlinear crystals," Opt. Mater. Express **3**, 1647–1657 (2013).

[99] C. Langrock, S. Kumar, J. McGeehan, A. Willner, and M. Fejer, "All-optical signal processing using $\chi^{(2)}$ nonlinearities in guided-wave devices," Lightwave Technology, Journal of **24**, 2579–2592 (2006).

[100] O. Tadanaga, T. Yanagawa, Y. Nishida, H. Miyazawa, K. Magari, M. Asobe, and H. Suzuki, "Efficient 3-μm difference frequency generation using direct-bonded quasi-phase-matched $LiNbO_3$ ridge waveguides," Appl. Phys. Lett. **88**, 061101 (2006).

[101] R. Schiek, Y. Baek, and G. I. Stegeman, "Second-harmonic generation and cascaded nonlinearity in titanium-indiffused lithium niobate channel waveguides," J. Opt. Soc. Am. B **15**, 2255–2268 (1998).

[102] R. Schiek, H. Seibert, W. Sohler, M. L. Sundheimer, D. Y. Kim, Y. Baek, and G. I. Stegeman, "Direct measurement of cascaded nonlinearity in lithium niobate channel waveguides," Opt. Lett. **19**, 1949–1951 (1994).

[103] M. L. Bortz and M. M. Fejer, "Annealed proton-exchanged $LiNbO_3$ waveguides," Opt. Lett. **16**, 1844–1846 (1991).

[104] K. Gallo, J. Prawiharjo, N. Broderick, and D. Richardson, "Proton-exchanged $LiNbO_3$ waveguides for photonic applications," Proceedings of 2004 6th International Conference on Transparent Optical Networks **1**, 277–281 (2004).

[105] Y. Nishida, H. Miyazawa, M. Asobe, O. Tadanaga, and H. Suzuki, "0-db wavelength conversion using direct-bonded QPM-Zn:$LiNbO_3$ ridge waveguide," IEEE Photon. Technol. Lett. **17**, 1049–1051 (2005).

[106] P. Rabiei, J. Ma, S. Khan, J. Chiles, and S. Fathpour, "Heterogeneous lithium niobate photonics on silicon substrates," Opt. Express **21**, 25573–25581 (2013).

Chapter 2

Numerical Models for Pulse Propagation in Nonlinear Media

2.1 Introduction

In this chapter, several most frequent-used numerical models for pulse propagations in nonlinear media are presented, namely the nonlinear wave equation in frequency domain (NWEF), coupled wave equations (CWEs) and the nonlinear Schrödinger-like (NLS-like) equation. All these models, with corresponding mathematical equations, are derived from the common parent, Maxwell's equations, but with approximations at different levels. With the concentration on dielectric media (non-magnetic and no free charges), these equations mainly deal with the electric field, or field envelope of the pulsed laser light. Both quadratic and cubic nonlinearities are concerned and included in these models and media with waveguide structures are also taken into consideration.

2.2 Maxwell Wave Equation and Nonlinear Induced Polarizations

We start with Maxwell's equations and material equations shown below [1–3]:

$$\begin{aligned} \nabla \times \mathbf{E} &= -\frac{\partial \mathbf{B}}{\partial t} \\ \nabla \times \mathbf{H} &= -\frac{\partial \mathbf{D}}{\partial t} + \mathbf{J} \\ \nabla \bullet \mathbf{B} &= 0 \\ \nabla \bullet \mathbf{D} &= \rho \\ \nabla \bullet \mathbf{J} &= -\frac{\partial \rho}{\partial t} \end{aligned} \tag{2.1}$$

$$\begin{aligned} \mathbf{D} &= \varepsilon_0 \mathbf{E} + \mathbf{P} \\ \mathbf{B} &= \mu_0 \mathbf{H} + \mathbf{M} \\ \mathbf{J} &= \sigma \mathbf{E} \end{aligned} \tag{2.2}$$

"∇" is the Laplace operator, $\mathbf{E}$ and $\mathbf{H}$ indicate the electric field (unit: $\frac{\mathrm{V}}{\mathrm{m}}$) and magnetic field (unit: $\frac{\mathrm{A}}{\mathrm{m}}$) vectors, $\mathbf{D}$ and $\mathbf{B}$ indicate the electric and magnetic flux densities. $\mathbf{J}$ is the current density vector and ρ is the charge density, both representing the source for the electromagnetic field. ε_0 is the vacuum permittivity (unit: $\frac{\mathrm{F}}{\mathrm{m}}$) and μ_0 is the vacuum permeability (unit: $\frac{\mathrm{H}}{\mathrm{m}}$). $\mathbf{P}$ and $\mathbf{M}$ indicate the induced electric and magnetic polarizations.

In the absence of free charges and in a nonmagnetic medium, we have $\mathbf{M} = 0$, $\mathbf{J} = 0$ and $\rho = 0$. Hence Maxwell's equations are simplified to:

$$\begin{aligned} \nabla \times \mathbf{E} &= -\frac{\partial \mathbf{B}}{\partial t} \\ \nabla \times \mathbf{H} &= \frac{\partial \mathbf{D}}{\partial t} \end{aligned} \tag{2.3}$$

With the Fourier transform, $\tilde{F}(\omega) = \int_{-\infty}^{\infty} F(t)e^{-i\omega t}dt$ which matches the discrete Fourier transform (DFT) algorithm in *Matlab*, Eq.(2.3) can be written in frequency domain:

$$\begin{aligned} \nabla \times \tilde{\mathbf{E}} &= -i\omega\tilde{\mathbf{B}} = -i\omega\mu_0\tilde{\mathbf{H}} \\ \nabla \times \tilde{\mathbf{H}} &= i\omega\tilde{\mathbf{D}} = i\omega(\varepsilon_0\tilde{\mathbf{E}} + \tilde{\mathbf{P}}) \end{aligned} \tag{2.4}$$

The derivation of the Maxwell wave equation requires the following relationship:

$$\nabla \times (\nabla \times \tilde{\mathbf{E}}) = \nabla(\nabla \bullet \tilde{\mathbf{E}}) - \nabla^2\tilde{\mathbf{E}} \tag{2.5}$$

in which the left side can be extended as:

$$\begin{aligned} \nabla \times (\nabla \times \tilde{\mathbf{E}}) = \nabla \times (-i\omega\mu_0\tilde{\mathbf{H}}) &= -i\omega\mu_0 \cdot (\nabla \times \tilde{\mathbf{H}}) \\ = -i\omega\mu_0 \cdot i\omega(\varepsilon_0\tilde{\mathbf{E}} + \tilde{\mathbf{P}}) &= \omega^2\mu_0\varepsilon_0\tilde{\mathbf{E}} + \omega^2\mu_0\tilde{\mathbf{P}} \\ &= k_0^2(\omega)\tilde{\mathbf{E}} + \omega^2\mu_0\tilde{\mathbf{P}} \end{aligned} \tag{2.6}$$

The right-side term has:

$$\nabla(\nabla \bullet \tilde{\mathbf{E}}) - \nabla^2\tilde{\mathbf{E}} \approx -\nabla^2\tilde{\mathbf{E}} \tag{2.7}$$

which is supported if: 1) the high order induced electric polarizations (nonlinear induced polarizations) are considered as perturbations to the first order induced polarization (linear induced polarization), i.e. $\tilde{\mathbf{P}} = \tilde{\mathbf{P}}_L + \tilde{\mathbf{P}}_{NL} \approx \tilde{\mathbf{P}}_L = 2\pi\varepsilon_0\tilde{\boldsymbol{\chi}}^{(1)}\tilde{\mathbf{E}}$; 2) the relative permittivity $\varepsilon_r = 1 + 2\pi\tilde{\boldsymbol{\chi}}^{(1)}$ is independent on the spatial distribution, i.e. $\nabla \bullet \tilde{\mathbf{E}} = \nabla \bullet \tilde{\mathbf{D}}/\varepsilon_0\varepsilon_r = 0$.

Hence, in frequency domain, the Maxwell's wave equation governing the electric field is derived:

$$\nabla^2\tilde{\mathbf{E}} + k_0^2(\omega)\tilde{\mathbf{E}} + \omega^2\mu_0\tilde{\mathbf{P}} = 0 \tag{2.8}$$

In time-domain, it is:

$$\nabla^2\mathbf{E} - \frac{1}{c^2}\frac{\partial^2\mathbf{E}}{\partial t^2} - \mu_0\frac{\partial^2\mathbf{P}}{\partial t^2} = 0 \tag{2.9}$$

The induced polarization $\tilde{\mathbf{P}}$ can be expanded as the sum of contributions of different orders, i.e:

$$\mathbf{P} = \mathbf{P}^{(1)} + \mathbf{P}^{(2)} + \mathbf{P}^{(3)} + \cdots + \mathbf{P}^{(m)} \tag{2.10}$$

and the generalized expression of both the linear induced polarization $\mathbf{P}^{(1)} = \mathbf{P}_L$ and the nonlinear induced polarization $\mathbf{P}^{(m)}$ is:

$$\begin{aligned}
&\mathbf{P}^{(m)} \\
&= \varepsilon_0 \int_{-\infty}^{\infty} dt_1 \int_{-\infty}^{\infty} dt_2 \cdots \int_{-\infty}^{\infty} dt_m \boldsymbol{\chi}^{(m)}(t_1, t_2, \cdots, t_m) \\
&\qquad | \ \mathbf{E}(t - t_1)\mathbf{E}(t - t_2) \cdots \mathbf{E}(t - t_m) \\
&= \varepsilon_0 \int_{-\infty}^{\infty} dt_1 \int_{-\infty}^{\infty} dt_2 \cdots \int_{-\infty}^{\infty} dt_m \boldsymbol{\chi}^{(m)}(t - t_1, t - t_2, \cdots, t - t_m) \\
&\qquad | \ \mathbf{E}(t_1)\mathbf{E}(t_2) \cdots \mathbf{E}(t_m) \\
&= \varepsilon_0 \int_{-\infty}^{\infty} d\omega_1 \int_{-\infty}^{\infty} d\omega_2 \cdots \int_{-\infty}^{\infty} d\omega_m \tilde{\boldsymbol{\chi}}^{(m)}(\omega_1, \omega_2, \cdots, \omega_m) \\
&\qquad | \ \tilde{\mathbf{E}}(\omega_1)\tilde{\mathbf{E}}(\omega_2) \cdots \tilde{\mathbf{E}}(\omega_m) e^{it \sum \omega_i}
\end{aligned} \tag{2.11}$$

where:

$$\begin{aligned}
&\tilde{\boldsymbol{\chi}}^{(m)}(\omega_1, \omega_2, \cdots \omega_m) \\
&\qquad = \frac{1}{(2\pi)^m} \int_{-\infty}^{\infty} dt_1 \int_{-\infty}^{\infty} dt_2 \cdots \int_{-\infty}^{\infty} dt_m \\
&\qquad\qquad \times \boldsymbol{\chi}^{(m)}(t_1, t_2, \cdots t_m) e^{-i \sum \omega_i t_i}
\end{aligned} \tag{2.12}$$

$\boldsymbol{\chi}^{(m)}$ is the temporal response function of the material, also called the susceptibility in frequency domain, which is a (m+1)-rank tensor. The calculations among the electric fields are dyadic product which result in an m-rank tensor. "|" indicate the multiple tensor product between two tensors, i.e. a (m+1)-rank tensor and a m-rank tensor (or dyadic tensor). Therefore, the induced

polarization $\mathbf{P}^{(m)}$ is a vector. In frequency domain, it is:

$$\begin{aligned}\tilde{\mathbf{P}}^{(m)}(\omega) &= \int_{-\infty}^{+\infty} \mathbf{P}^{(m)} e^{-i\omega t} dt \\ &= \varepsilon_0 \int_{-\infty}^{\infty} d\omega_1 \cdots \int_{-\infty}^{\infty} d\omega_m \tilde{\boldsymbol{\chi}}^{(m)}(\omega_1, \cdots, \omega_m) \\ &\qquad \mid \tilde{\mathbf{E}}(\omega_1) \cdots \tilde{\mathbf{E}}(\omega_m) \int_{-\infty}^{+\infty} e^{-i(\omega - \sum \omega_i)t} dt \\ &= 2\pi\varepsilon_0 \int_{-\infty}^{\infty} d\omega_1 \cdots \int_{-\infty}^{\infty} d\omega_m \tilde{\boldsymbol{\chi}}^{(m)}(\omega_1, \cdots, \omega_m) \\ &\qquad \mid \tilde{\mathbf{E}}(\omega_1) \cdots \tilde{\mathbf{E}}(\omega_m) \delta(\omega - \sum \omega_i)\end{aligned} \tag{2.13}$$

Here, the delta function $\delta(\omega)$ implies that the induced polarization always corresponds to the frequency which equals to the sum frequency of the contributing electric fields.

If setting $\Omega = \sum \omega_i$, i.e. $d\Omega = d\omega_i$ and $\int_{-\infty}^{+\infty} \delta(\omega - \Omega) d\Omega = 1$, Eq.(2.13) further becomes:

$$\begin{aligned}&\tilde{\mathbf{P}}^{(m)}(\Omega) \\ &\qquad = 2\pi\varepsilon_0 \int_{-\infty}^{\infty} d\omega_1 \int_{-\infty}^{\infty} d\omega_2 \cdots \int_{-\infty}^{\infty} d\omega_{m-1} \\ &\qquad\qquad \times \tilde{\boldsymbol{\chi}}^{(m)}(\omega_1, \omega_2, \cdots, \Omega - \sum\nolimits_1^{m-1} \omega_i) \\ &\qquad\qquad \mid \mathbf{E}(\omega_1)\mathbf{E}(\omega_2) \cdots \mathbf{E}(\Omega - \sum\nolimits_1^{m-1} \omega_i)\end{aligned} \tag{2.14}$$

where $m \geq 2$ and $\tilde{\mathbf{P}}^{(1)}(\Omega) = 2\pi\varepsilon_0 \tilde{\boldsymbol{\chi}}^{(1)}(\Omega) \bullet \tilde{\mathbf{E}}(\Omega)$.

Since $\mathbf{P}^{(m)}$ is a vector, it can be written as a sum of its components, each casting to one dimension in a orthogonal system, i.e. $\mathbf{P}^{(m)} = \sum \hat{j} P_j^{(m)}$. Analogously, The nonlinear response tensor $\boldsymbol{\chi}^{(m)}$ has $\boldsymbol{\chi}^{(m)} = \sum \hat{j} \mathbf{R}_j^{(m)}$ and $\mathbf{R}_j^{(m)}$ is an m-rank tensor, i.e.:

$$\mathbf{R}_j^{(m)} = \sum_{\alpha_1 \cdots \alpha_m} \left[\left(\prod_{s=1}^{m} \hat{\alpha}_s \right) \cdot \chi_{j;\alpha_1 \cdots \alpha_m}^{(m)} \right] \tag{2.15}$$

where $j, \alpha_1, \cdots, \alpha_m$ are dimension marks. The electric field also has $\mathbf{E} = \sum \hat{j} E_j$.

Thus, the component of the induced polarization $P_j^{(m)}$ is written as:

$$\begin{aligned} & P_j^{(m)}(t) \\ & = \varepsilon_0 \int_{-\infty}^{\infty} dt_1 \int_{-\infty}^{\infty} dt_2 \cdots \int_{-\infty}^{\infty} dt_m \\ & \quad \times \mathbf{R}_j^{(m)}(t-t_1, t-t_2, \cdots, t-t_m) | \mathbf{E}(t_1)\mathbf{E}(t_2)\cdots\mathbf{E}(t_m) \\ & = \varepsilon_0 \sum_{\alpha_1 \cdots \alpha_m} \left\{ \int_{-\infty}^{\infty} dt_1 \cdots \int_{-\infty}^{\infty} dt_m \right. \\ & \quad \left. \times \chi_{j;\alpha_1\cdots\alpha_m}^{(m)}(t-t_1, \cdots, t-t_m) \cdot E_{\alpha_1}(t_1)\cdots E_{\alpha_m}(t_m) \right\} \end{aligned} \tag{2.16}$$

In frequency domain, it is:

$$\begin{aligned} & \tilde{P}_j^{(m)}(\Omega) \\ & = 2\pi\varepsilon_0 \sum_{\alpha_1 \cdots \alpha_m} \left\{ \int_{-\infty}^{\infty} d\omega_1 \cdots \int_{-\infty}^{\infty} d\omega_{m-1} \right. \\ & \quad \times \tilde{\chi}_{j;\alpha_1\cdots\alpha_m}^{(m)}(\omega_1, \cdots, \omega_{m-1}, \Omega - \sum\nolimits_1^{m-1} \omega_i) \\ & \quad \left. \times \tilde{E}_{\alpha_1}(\omega_1)\cdots\tilde{E}_{\alpha_{m-1}}(\omega_{m-1})\tilde{E}_{\alpha_m}(\Omega - \sum\nolimits_1^{m-1} \omega_i) \right\} \end{aligned} \tag{2.17}$$

where $m \geq 2$ and $\tilde{P}_j^{(1)}(\Omega) = 2\pi\varepsilon_0 \sum_{\alpha_1} \left\{ \tilde{\chi}_{j;\alpha_1}^{(1)}(\Omega)\tilde{E}_{\alpha_1}(\Omega) \right\}$. $\tilde{\chi}_{j;\alpha_1\cdots\alpha_m}^{(m)}$ corresponds to one component of the tensor $\tilde{\boldsymbol{\chi}}^{(m)}$, in which $\tilde{\chi}_{j;\alpha_1}^{(1)}$ belongs to the two-dimensional matrix $\tilde{\boldsymbol{\chi}}^{(1)}$.

Therefore, each component of the electric field $\tilde{E}_j$ has a wave equation which, in frequency domain, reads:

$$\nabla^2\tilde{E}_j + k_0^2(\omega)\tilde{E}_j + \omega^2\mu_0\tilde{P}_j = 0; \tilde{P}_j = \tilde{P}_j^{(1)} + \tilde{P}_j^{(2)} + \cdots + \tilde{P}_j^{(m)} \tag{2.18}$$

In particular, in uniaxial and biaxial crystals as well as cubic/isotropic materials, matrix $\tilde{\boldsymbol{\chi}}^{(1)}$ only has diagonal elements and $\tilde{P}_j^{(1)}(\Omega) = 2\pi\varepsilon_0\tilde{\chi}_{j;j}^{(1)}(\Omega)\tilde{E}_j(\Omega)$. By combining $\tilde{P}_j^{(1)}$ with $k_0^2\tilde{E}_j$, the wave equation becomes:

$$\nabla^2\tilde{E}_j + k_j^2(\omega)\tilde{E}_j + \omega^2\mu_0\tilde{P}_{j,NL} = 0; \tilde{P}_{j,NL} = \tilde{P}_j^{(2)} + \cdots + \tilde{P}_j^{(m)} \tag{2.19}$$

where $k_j^2(\omega) = k_0^2(1 + 2\pi\tilde{\chi}_{j;j}^{(1)})$ is the spatial phase in which the refractive index is defined as $n_j = \sqrt{1 + 2\pi\tilde{\chi}_{j;j}^{(1)}}$.

2.3 Nonlinear Wave Equation in Frequency Domain (NWEF)

2.3.1 1+1D NWEF

In a bulk medium, the electric field has three spatial components, i.e E_x, E_y and E_z, in which E_z is always neglected with the paraxial approximation. So the axis z is defined as the propagation axis along which the propagation dynamics of the light is described. E_x and E_y have both the spatial and propagation dynamics. However, in the assumption of the plane-wave propagation (assuming a large beam diameter), the spatial dynamics is supposed to be uniform so that it is neglected as well. Therefore, the Laplace operator in the Maxwell wave equation Eq.(2.19) is degraded to be only with respect to the axis z since the spatial terms are zeros, i.e. $\nabla^2 \to \frac{\partial^2}{\partial z^2}$. Thus, Eq.(2.19) is degraded to the 1+1D Maxwell wave equation:

$$\frac{\partial^2}{\partial z^2}\tilde{E}_j + k_j^2(\omega)\tilde{E}_j + \omega^2\mu_0\tilde{P}_{j,NL} = 0 \tag{2.20}$$

Moreover, by factoring out the fast dependence of the propagation coordinate from the electric field for all the frequencies, i.e.: [4]

$$\tilde{E}_j(z,\omega) = \tilde{U}_j(z,\omega)e^{-ik_j(\omega)z} \tag{2.21}$$

the wave equation governing the slowly varying spectral envelope, $\tilde{U}_j$, is obtained:

$$\frac{\partial^2}{\partial z^2}\tilde{U}_j - 2ik_j(\omega)\frac{\partial}{\partial z}\tilde{U}_j + \omega^2\mu_0\tilde{P}_{j,NL}e^{ik_jz} = 0 \tag{2.22}$$

Then, with the slowly varying spectral amplitude approximation (SVSAA) [5], i.e. $\left|\frac{\partial}{\partial z}\tilde{U}_j\right| \ll \left|k_j\tilde{U}_j\right|$ and $\frac{\partial^2}{\partial z^2}\tilde{U}_j \ll \frac{\partial}{\partial z}k_j\tilde{U}_j$, the first term in the above equation can be removed, making:

$$\frac{\partial}{\partial z}\tilde{U}_j = -i\frac{\omega^2\mu_0}{2k_j(\omega)}\tilde{P}_{j,NL}e^{ik_jz} \tag{2.23}$$

Then,by back replacing the envelope with the electric field, the famous reduced Maxwell wave equation (containing only the first-order derivative with respect to z of the electric field) is derived [6–8]:

$$\frac{\partial\tilde{E}_j}{\partial z} + ik_j(\omega)\tilde{E}_j = -i\frac{\omega^2\mu_0}{2k_j(\omega)}\tilde{P}_{j,NL} \tag{2.24}$$

Equation (2.24) is also called the nonlinear wave equation in frequency domain (NWEF), provided with a detailed interpretation of the nonlinear induced polarization term $\tilde{P}_{j,NL}$. Among all types of the nonlinear induced polarization, second-order and third order nonlinear induced polarizations are most concerned. The second-order nonlinear induced polarization is the source of the quadratic nonlinearity, giving rise to three-wave-mixing (TWM) processes such as second harmonic generations (SHGs), sum frequency generations (SFGs) and different frequency generations (DFGs). The response is always considered to be instantaneous:

$$\chi^{(2)}_{j;\alpha_1\alpha_2}(t_1,t_2) = \bar{\chi}^{(2)}_{j;\alpha_1\alpha_2}\delta(t_1)\delta(t_2) \tag{2.25}$$

where $\bar{\chi}^{(2)}_{j;\alpha_1\alpha_2}$ is a constant indicating the response intensity. By using Eq.(2.12), the susceptibility in frequency domain is:

$$\tilde{\chi}^{(2)}_{j;\alpha_1\alpha_2}(\omega_1,\omega_2) = \tfrac{1}{(2\pi)^2}\bar{\chi}^{(2)}_{j;\alpha_1\alpha_2} \tag{2.26}$$

which is actually constant for all the frequencies ω_1 and ω_2. Hence, the second-order nonlinear induced polarization $P^{(2)}_j$ has a simple expression, i.e. [9]:

$$P^{(2)}_j(t) = \varepsilon_0 \sum_{\alpha_1\alpha_2}\left\{\bar{\chi}^{(2)}_{j;\alpha_1\alpha_2}E_{\alpha_1}E_{\alpha_2}\right\} \tag{2.27}$$

$$\begin{aligned}\tilde{P}^{(2)}_j(\omega) &= \varepsilon_0 \sum_{\alpha_1\alpha_2}\left\{\bar{\chi}^{(2)}_{j;\alpha_1\alpha_2}\tilde{E}_{\alpha_1}\tfrac{\otimes}{2\pi}\tilde{E}_{\alpha_2}\right\} \\ &= \varepsilon_0 \sum_{\alpha_1\alpha_2}\left\{\bar{\chi}^{(2)}_{j;\alpha_1\alpha_2}F\left[E_{\alpha_1}E_{\alpha_2}\right]\right\}\end{aligned} \tag{2.28}$$

The third-order nonlinear induced polarization backs the cubic nonlinearity, in which the response is not fully instantaneous but a combination of a instantaneous response fraction (i.e. the electronic response) and a delayed response fraction (i.e. the vibrational Raman response):

$$\chi^{(3)}_{j;\alpha_1\alpha_2\alpha_3}(t_1,t_2,t_3) = \bar{\chi}^{(3)}_{j;\alpha_1\alpha_2\alpha_3}R(t_1)\delta(t_2-t_1)\delta(t_3) \tag{2.29}$$

where $R(t) = (1-f_R)\delta(t) + f_R h_R(t)$ and $\int_{-\infty}^{\infty} h_R(t)dt = 1$. f_R indicates the amount of the Raman fraction. $h_R(t)$ is the temporal Raman response function. The remaining instantaneous response will give rise to the four-wave-mixing (FWM) processes such as the Kerr effects including the self-phase modulation (SPM) and the cross-phase modulation (XPM), and third harmonic generations

(THGs). In frequency domain, the susceptibility is:

$$\tilde{\chi}^{(3)}_{j;\alpha_1\alpha_2\alpha_3}(\omega_1,\omega_2,\omega_3) = \frac{1}{(2\pi)^3}\bar{\chi}^{(3)}_{j;\alpha_1\alpha_2\alpha_3}\left[(1-f_R)+f_R\tilde{h}_R(\omega_1+\omega_2)\right] \quad (2.30)$$

Hence, the third-order nonlinear induced polarization $P_j^{(3)}$ reads, in time domain:

$$P_j^{(3)}(t) = \varepsilon_0 \sum_{\alpha_1\alpha_2\alpha_3}\Big\{\bar{\chi}^{(3)}_{j;\alpha_1\alpha_2\alpha_3}\left[(1-f_R)E_{\alpha_1}E_{\alpha_2}E_{\alpha_3} + f_R(h_R\otimes(E_{\alpha_1}E_{\alpha_2}))E_{\alpha_3}\right]\Big\} \quad (2.31)$$

and in frequency domain:

$$\begin{aligned}\tilde{P}_j^{(3)}(\omega) &= \varepsilon_0 \sum_{\alpha_1\alpha_2\alpha_3}\Big\{\bar{\chi}^{(3)}_{j;\alpha_1\alpha_2\alpha_3}\Big[(1-f_R)(\tilde{E}_{\alpha_1}\tfrac{\otimes}{2\pi}\tilde{E}_{\alpha_2}\tfrac{\otimes}{2\pi}\tilde{E}_{\alpha_3}) \\ &\qquad +f_R(\tilde{h}_R(\tilde{E}_{\alpha_1}\tfrac{\otimes}{2\pi}\tilde{E}_{\alpha_2}))\tfrac{\otimes}{2\pi}\tilde{E}_{\alpha_3}\Big]\Big\} \\ &= \varepsilon_0 \sum_{\alpha_1\alpha_2\alpha_3}\Big\{\bar{\chi}^{(3)}_{j;\alpha_1\alpha_2\alpha_3}\left[(1-f_R)F\left[E_{\alpha_1}E_{\alpha_2}E_{\alpha_3}\right]\right. \\ &\qquad \left. +f_R F\left[E_{\alpha_3}F^{-1}\left[\tilde{h}_R F\left[E_{\alpha_1}E_{\alpha_2}\right]\right]\right]\right]\Big\}\end{aligned} \quad (2.32)$$

Finally, by replacing $\tilde{P}_{j,NL}$ in Eq.(2.24) with their interpretations Eq.(2.28) and Eq.(2.32), the 1+1D NWEF is derived:

$$\begin{aligned}&\frac{\partial\tilde{E}_j}{\partial z} + ik_j(\omega)\tilde{E}_j \\ &\quad = -i\frac{\omega^2}{2c^2k_j(\omega)}\sum_{\alpha_1\alpha_2}\left(\bar{\chi}^{(2)}_{j;\alpha_1\alpha_2}F\left[E_{\alpha_1}E_{\alpha_2}\right]\right) \\ &\qquad -i\frac{\omega^2}{2c^2k_j(\omega)}\sum_{\alpha_1\alpha_2\alpha_3}\Big\{\bar{\chi}^{(3)}_{j;\alpha_1\alpha_2\alpha_3}\left[(1-f_R)\,F\left[E_{\alpha_1}E_{\alpha_2}E_{\alpha_3}\right]\right. \\ &\qquad\qquad \left. +f_R F\left[E_{\alpha_3}F^{-1}\left[\tilde{h}_R F\left[E_{\alpha_1}E_{\alpha_2}\right]\right]\right]\right]\Big\}\end{aligned} \quad (2.33)$$

It is noted that the NWEF directly governs the light electric field (component) rather than the field envelope. In nature, the electric field is in time domain a real-valued wave. Using the Fourier transform will cast it to a frequency domain spanning $(-\infty,+\infty)$, where the field spectrum at positive frequencies is complex conjugate to that at negative frequencies. Meanwhile, the wave

vector $k_j(\omega)$ as well as the nonlinear induced polarization $\tilde{P}_{j,NL}$ also shows the property of complex conjugate in such a physical frequency domain since both linear and nonlinear temporal responses are realistic and with casuality. Fundamentally, the NWEF automatically includes all types of quadratic and cubic nonlinear interactions (SHG, THG, SPM, etc.) as it holds the general form of expression of the nonlinear induced polarizations. The anisotropy of the nonlinearity is also taken into consideration. Mathematically, the equation can be numerically solved by employing the split-step Fourier method together with the Runge-Kutta algorithm.

2.3.2 NWEF in Waveguides

When media have waveguide structures, the pulsed laser light will be properly guided by the waveguide eigen-modes. Since eigen-modes have the property of orthogonality among each other, each mode is one separated dimension. Therefore, the electric field is the sum of all these modes just as it is the sum of the orthogonal spatial components in bulk media. The dimension mark j is redefined as the mode mark. Moreover, each mode (component) is defined as the combination of the transverse spatial distribution and the propagation dynamics, i.e. [10]:

$$\begin{aligned}\tilde{E}_j(x,y,z,\omega) &= \tilde{B}_j(x,y,\omega)\tilde{A}_j(z,\omega) \\ &= \tilde{B}_j(x,y,\omega)\tilde{U}_j(z,\omega)e^{-i\beta_j(\omega)z}\end{aligned} \tag{2.34}$$

where $\tilde{B}_j$ is the eigen-mode distribution which is normalized to have:

$$\iint dxdy \cdot \tilde{B}_j = 1 \tag{2.35}$$

$\tilde{A}_j$ indicates the electric field amplitude which reflects the propagation dynamics and holds the electric field unit $\frac{\mathrm{V}}{\mathrm{m}}$, and β_j indicates the mode propagation constant.

Now, Eq.(2.19) can be expanded to:

$$\begin{aligned}\tilde{U}_j e^{-i\beta_j(\omega)z}\left(\frac{\partial^2}{\partial x^2}+\frac{\partial^2}{\partial y^2}+k_j^2-\beta_j^2\right)\tilde{B}_j \\ +\tilde{B}_j e^{-i\beta_j(\omega)z}\left(\frac{\partial^2}{\partial z^2}-i2\beta_j\frac{\partial}{\partial z}\right)\tilde{U}_j+\omega^2\mu_0\tilde{P}_{j,NL}=0\end{aligned} \tag{2.36}$$

By recalling that all eigen-modes in a waveguide have:

$$(\tfrac{\partial^2}{\partial x^2}+\tfrac{\partial^2}{\partial y^2}+k_j^2-\beta_j^2)=0 \tag{2.37}$$

and using the SVSAA, we get the reduced Maxwell equation regarding the waveguide, i.e.:

$$\frac{\partial \tilde{E}_j}{\partial z} + i\beta_j(\omega)\tilde{E}_j = -i\frac{\omega^2\mu_0}{2\beta_j(\omega)}\tilde{P}_{j,NL} \tag{2.38}$$

Compared with the 1+1D wave equation Eq.(2.24), the only change of the mathematical expression in Eq.(2.38) is the replacement of the spatial propagation constant k_j with mode propagation constant β_j. However, it should be noticed that, besides dispersion properties, nonlinear induced polarizations are also changed by having the waveguide structure, which will be revealed soon. Moreover, it is also the propagation dynamics that is most concerned rather than the electric field component as a whole. Therefore, by making spatial integral on both sides of the equation, the transverse spatial distribution is degenerated and the equation is further derived to govern the field amplitude $\tilde{A}_j$ solely:

$$\iint_{\infty} dxdy\tilde{B}_j^* \left(\frac{\partial}{\partial z} + i\beta_j\right)\tilde{E}_j = -i\frac{\omega^2\mu_0}{2\beta_j}\iint_{\infty} dxdy\tilde{B}_j^*\tilde{P}_{j,NL} \tag{2.39}$$

$$\frac{\partial \tilde{A}_j}{\partial z} + i\beta_j(\omega)\tilde{A}_j = -i\frac{\omega^2\mu_0}{2\beta_j(\omega)}\iint_{\infty} dxdy\tilde{B}_j^*\tilde{P}_{j,NL} \tag{2.40}$$

Then, we interpret the nonlinear induced polarization in the above equation. For the second-order nonlinear induced polarization, we employ Eq.(2.17) and expand it with the definition of the electric field component, i.e.:

$$\begin{aligned}
&\iint_{\infty} dxdy\tilde{B}_j^*\tilde{P}_j^{(2)} \\
&\quad = 2\pi\varepsilon_0 \sum_{\alpha_1\alpha_2} \int_{-\infty}^{\infty} \Big\{ d\omega_1 \tilde{A}_{\alpha_1}(\omega_1)\tilde{A}_{\alpha_2}(\Omega-\omega_1) \\
&\qquad \times \iint_{\infty} dxdy\tilde{\chi}^{(2)}_{j;\alpha_1\alpha_2}(x,y,\omega_1,\Omega-\omega_1) \\
&\qquad \times \tilde{B}_j^*(x,y,\Omega)\tilde{B}_{\alpha_1}(x,y,\omega_1)\tilde{B}_{\alpha_2}(x,y,\Omega-\omega_1)\Big\}
\end{aligned} \tag{2.41}$$

where the nonlinear susceptibility is space-dependent with variables (x, y). A

spacial integral factor can be defined, which is [10]:

$$\begin{aligned}
&\tilde{\Theta}^{(2)}_{j;\alpha_1\alpha_2}(\omega_1,\omega_2) \\
&\quad= \iint_{\infty} dxdy\tilde{\chi}^{(2)}_{j;\alpha_1\alpha_2}(x,y,\omega_1,\omega_2) \\
&\qquad\times \tilde{B}^*_j(x,y,\omega_1+\omega_2)\tilde{B}_{\alpha_1}(x,y,\omega_1)\tilde{B}_{\alpha_2}(x,y,\omega_2) \\
&\quad= \frac{1}{(2\pi)^2}\iint_{\infty} dxdy\bar{\chi}^{(2)}_{j;\alpha_1\alpha_2}(x,y) \\
&\qquad\times \tilde{B}^*_j(x,y,\omega_1+\omega_2)\tilde{B}_{\alpha_1}(x,y,\omega_1)\tilde{B}_{\alpha_2}(x,y,\omega_2)
\end{aligned} \tag{2.42}$$

with which the second-order nonlinear induced polarization is:

$$\begin{aligned}
&\iint_{\infty} dxdy\tilde{B}^*_j\tilde{P}^{(2)}_j \\
&\qquad= 2\pi\varepsilon_0\sum_{\alpha_1\alpha_2}\int_{-\infty}^{\infty} d\omega_1\tilde{\Theta}^{(2)}_{j;\alpha_1\alpha_2}(\omega_1,\Omega-\omega_1)\tilde{A}_{\alpha_1}(\omega_1)\tilde{A}_{\alpha_2}(\Omega-\omega_1)
\end{aligned} \tag{2.43}$$

Moreover, in frequency domain, it can be assumed that the mode distribution $\tilde{B}_j$ is slowly varying compared to the $\tilde{A}_j$, namely the slowly varying mode distribution approximation (SVMDA). Thus, the spatial integral factor is considered as constant $\tilde{\Theta}^{(2)}_{j;\alpha_1\alpha_2}(\omega_1,\omega_2) \approx \frac{1}{(2\pi)^2}\bar{\Theta}^{(2)}_{j;\alpha_1\alpha_2}$. The second-order induced polarization is then simplified to:

$$\begin{aligned}
\iint_{\infty} dxdy\tilde{B}^*_j\tilde{P}^{(2)}_j &= \varepsilon_0\sum_{\alpha_1\alpha_2}\left\{\bar{\Theta}^{(2)}_{j;\alpha_1\alpha_2}\tilde{A}_{\alpha_1}\underset{2\pi}{\otimes}\tilde{A}_{\alpha_2}\right\} \\
&= \varepsilon_0\sum_{\alpha_1\alpha_2}\left\{\bar{\Theta}^{(2)}_{j;\alpha_1\alpha_2}F\left[A_{\alpha_1}A_{\alpha_2}\right]\right\}
\end{aligned} \tag{2.44}$$

Analogously, the third-order nonlinear induced polarization could be written as:

$$\begin{aligned}
&\iint_{\infty} dxdy\tilde{B}^*_j\tilde{P}^{(3)}_j \\
&\qquad= \varepsilon_0\sum_{\alpha_1\alpha_2\alpha_3}\Big\{\bar{\Theta}^{(3)}_{j;\alpha_1\alpha_2\alpha_3}\left[(1-f_R)F\left[A_{\alpha_1}A_{\alpha_2}A_{\alpha_3}\right]\right. \\
&\qquad\qquad\left.+f_RF\left[A_{\alpha_3}F^{-1}\left[\tilde{h}_RF\left[A_{\alpha_1}A_{\alpha_2}\right]\right]\right]\right]\Big\}
\end{aligned} \tag{2.45}$$

where

$$\begin{aligned}
&\tilde{\Theta}^{(3)}_{j;\alpha_1\alpha_2\alpha_3}(\omega_1,\omega_2,\omega_3)\\
&=\iint_{\infty} dxdy\tilde{\chi}^{(3)}_{j;\alpha_1\alpha_2\alpha_3}(x,y,\omega_1,\omega_2,\omega_3)\\
&\quad\times\tilde{B}^{*}_{j}(x,y,\sum\nolimits_{n}\omega_n)\tilde{B}_{\alpha_1}(x,y,\omega_1)\tilde{B}_{\alpha_2}(x,y,\omega_2)\tilde{B}_{\alpha_3}(x,y,\omega_3)\\
&=\frac{\left[1-f_R+f_R\tilde{h}_R(\omega_1+\omega_2)\right]}{(2\pi)^3}\iint_{\infty} dxdy\bar{\chi}^{(3)}_{j;\alpha_1\alpha_2\alpha_3}\\
&\quad\times\tilde{B}^{*}_{j}(x,y,\sum\nolimits_{n}\omega_n)\tilde{B}_{\alpha_1}(x,y,\omega_1)\tilde{B}_{\alpha_2}(x,y,\omega_2)\tilde{B}_{\alpha_3}(x,y,\omega_3)\\
&\approx\frac{1}{(2\pi)^3}\bar{\Theta}^{(3)}_{j;\alpha_1\alpha_2\alpha_3}\left[1-f_R+f_R\tilde{h}_R(\omega_1+\omega_2)\right]
\end{aligned}\tag{2.46}$$

Integrals $\tilde{\Theta}^{(2)}_{j;\alpha_1\alpha_2}$ and $\tilde{\Theta}^{(3)}_{j;\alpha_1\alpha_2\alpha_3}$ are named "nonlinear modal susceptibilities" which not only include the nonlinear susceptibilities ($\tilde{\chi}^{(2)}_{j;\alpha_1\alpha_2}$, $\tilde{\chi}^{(3)}_{j;\alpha_1\alpha_2\alpha_3}$) reflecting the material properties, but also account the contribution of the mode overlap within the waveguide structure.

Finally, by replacing the nonlinear induced polarizations with their interpretations, NWEF dealing with waveguide structures is derived:

$$\begin{aligned}
&\frac{\partial\tilde{A}_j}{\partial z}+i\beta_j(\omega)\tilde{A}_j\\
&\quad=-i\frac{\omega^2}{2c^2\beta_j(\omega)}\sum_{\alpha_1\alpha_2}\left\{\bar{\Theta}^{(2)}_{j;\alpha_1\alpha_2}F\left[A_{\alpha_1}A_{\alpha_2}\right]\right\}\\
&\qquad-i\frac{\omega^2}{2c^2\beta_j(\omega)}\sum_{\alpha_1\alpha_2\alpha_3}\left\{\bar{\Theta}^{(3)}_{j;\alpha_1\alpha_2\alpha_3}\left[(1-f_R)F\left[A_{\alpha_1}A_{\alpha_2}A_{\alpha_3}\right]\right.\right.\\
&\qquad\qquad\left.\left.+f_RF\left[A_{\alpha_3}F^{-1}\left[\tilde{h}_RF\left[A_{\alpha_1}A_{\alpha_2}\right]\right]\right]\right]\right\}
\end{aligned}\tag{2.47}$$

2.3.3 Analytic Electric Field and Spectrum in Positive Frequency Domain

Although the physical frequency of the electric field (component) spans the whole frequency domain $(-\infty,+\infty)$ and the spectrum is supposed to have the property of complex conjugate, in realistic detections, it is only the spectrum at positive frequencies that is recorded while a blank remains at negative frequencies. Fundamentally, such a real detected spectrum is actually the analytic signal of the realistic electric field, which is verified here.

The spectrum of the electric field can be separated into two fractions, i.e. the positive-frequency spectrum (ω^+) and the negative-frequency spectrum (ω^-), and each spectral fraction further has the real part, $\tilde{E}^R$, and the imaginary part, $\tilde{E}^I$, reads:

$$\tilde{E}_j = \frac{1}{2}(\tilde{E}_j^R(\omega^+) + i\tilde{E}_j^I(\omega^+)) + \frac{1}{2}(\tilde{E}_j^R(\omega^-) + i\tilde{E}_j^I(\omega^-)) \tag{2.48}$$

where $\tilde{E}_j^R(\omega^+) = \tilde{E}_j^R(\omega^-)$, $\tilde{E}_j^I(\omega^+) = -\tilde{E}_j^I(\omega^-)$, $\omega^+ = -\omega^-$.

Then, with the inverse Fourier transform, the electric field is written as:

$$\begin{aligned} E_j =& \frac{1}{2}(E_j^{RR} + iE_j^{RI} + iE_j^{IR} + E_j^{II}) \\ &+ \frac{1}{2}(E_j^{RR} - iE_j^{RI} - iE_j^{IR} + E_j^{II}) = E_j^{RR} + E_j^{II} \end{aligned} \tag{2.49}$$

where

$$\begin{aligned} E_j^{RR} &= \int_0^\infty d\omega \tilde{E}_j^R(\omega^+) cos(\omega^+ t) \\ E_j^{RI} &= \int_0^\infty d\omega \tilde{E}_j^R(\omega^+) sin(\omega^+ t) \\ E_j^{IR} &= \int_0^\infty d\omega \tilde{E}_j^I(\omega^+) cos(\omega^+ t) \\ E_j^{II} &= -\int_0^\infty d\omega \tilde{E}_j^I(\omega^+) sin(\omega^+ t) \end{aligned} \tag{2.50}$$

Since $sin(\omega^+ t) = H[cos(\omega^+ t)]$ and $-cos(\omega^+ t) = H[sin(\omega^+ t)]$, where $H[f(t)]$ is the Hilbert transform:

$$H[f(t)] = \pi^{-1} p.v. \int_{-\infty}^{+\infty} d\tau f(t-\tau)/\tau \tag{2.51}$$

it is obvious to have: $E_j^{RI} = H[E_j^{RR}]$ and $E_j^{IR} = H[E_j^{II}]$.

Therefore, the real detected spectrum, the first right-side term in Eq.(2.48), corresponding to the first right-side term in Eq.(2.49) in time domain, is actually the analytic signal of the electric field, i.e.:

$$\begin{aligned} F^{-1}[\tilde{E}_j(\omega^+)] &= \frac{1}{2} F^{-1}\left[(\tilde{E}_j^R(\omega^+) + i\tilde{E}_j^I(\omega^+))\right] \\ &= \frac{1}{2}(E_j^{RR} + E_j^{II} + iH[E_j^{RR} + E_j^{II}]) \\ &= \frac{1}{2}(E_j + iH[E_j]) \end{aligned} \tag{2.52}$$

2.4 Coupled Wave Equations (CWEs)

Group of coupled wave equations (CWEs) [11] can be derived based on the NWEF, which targets at one or multiple specific nonlinear interactions, such as SHG, THG, SPM, etc. The critical approximation in CWEs is that different harmonics within an electric field component don't have significant spectral overlap among each other. With such an approximation, the electric field can be divided by harmonics such as the fundamental wave (FW), the second harmonic (SH) with doubled frequency, and so on. Meanwhile, each harmonic can be further considered consisting of an envelope, a carrier wave and a spatial phase term. For example, the FW can be written as:

$$E_{j,1}(z,t) = \frac{1}{2}\left(U_{j,1}(z,t)e^{i\omega_1 t - ik_{j;j}(\omega_1)z} + c.c.\right) \tag{2.53}$$

and then the SH is:

$$E_{j,2}(z,t) = \frac{1}{2}\left(U_{j,2}(z,t)e^{i\omega_2 t - ik_{j;j}(\omega_2)z} + c.c.\right) \tag{2.54}$$

where $\omega_2 = 2\omega_1$, *c.c.* represents the complex conjugate term since the electric field is real-valued.

Considering the noncritical SHG process in which the FW and SH share the same polarization direction, e.g. both are extraordinary wave ($j = e$), the electric field is therefore written as:

$$\begin{aligned} E_e =& \frac{1}{2}\left(U_{e,1}(t)e^{i\omega_1 t - ik_e(\omega_1)z} + c.c.\right) \\ &+ \frac{1}{2}\left(U_{e,2}(t)e^{i2\omega_2 t - ik_e(\omega_2)z} + c.c.\right) \end{aligned} \tag{2.55}$$

In frequency domain, it is:

$$\begin{aligned} \tilde{E}_e =& \frac{1}{2}\left(\tilde{U}_{e,1}(\omega-\omega_1)e^{-ik_e(\omega_1)z} + \tilde{U}^*_{e,1}(-\omega-\omega_1)e^{ik_e(\omega_1)z}\right) \\ &+ \frac{1}{2}\left(\tilde{U}_{e,2}(\omega-\omega_2)e^{-ik_e(\omega_2)z} + \tilde{U}^*_{e,2}(-\omega-\omega_2)e^{ik_e(\omega_2)z}\right) \end{aligned} \tag{2.56}$$

Nonlinear induced polarizations Eq.(2.28) and Eq.(2.32) are expanded to: (with the Raman term being excluded)

$$\begin{aligned} \tilde{P}^{(2)}_e = \varepsilon_0 \bar{\bar{\chi}}^{(2)}_{e;ee} \Bigg(& \frac{1}{2}U^*_{e,1}U_{e,2}e^{i\omega_1 t - iz[k_e(\omega_2)-k_e(\omega_1)]} \\ &+ \frac{1}{4}U^2_{e,1}e^{i\omega_2 t - i2k_e(\omega_1)z} + \cdots\Bigg) \end{aligned} \tag{2.57}$$

$$\begin{aligned}\tilde{P}_e^{(3)} =&\varepsilon_0\bar{\chi}_{e;eee}^{(3)}\left[\left(\frac{3}{8}|U_{e,1}|^2+\frac{3}{4}|U_{e,2}|^2\right)U_{e,1}e^{i\omega_1 t-ik_e(\omega_1)z}\right.\\&\left.\left(\frac{3}{4}|U_{e,1}|^2+\frac{3}{8}|U_{e,2}|^2\right)U_{e,2}e^{i\omega_2 t-ik_e(\omega_2)z}+\cdots\right]\end{aligned}\tag{2.58}$$

In these expanded equations, terms regarding the same harmonic can be gathered together, i.e. the FW should have the carrier wave term $e^{i\omega_1 t}$ and the SH has $e^{i\omega_2 t}$. Remember that there should be no overlap between the FW and the SH, so the NWEF can be separated into two equations, governing the FW and the SH, respectively:

$$\begin{aligned}&\frac{\partial\tilde{U}_{e,1}(\omega-\omega_1)}{\partial z}e^{-ik_e(\omega_1)z}+i\left[k_e(\omega)-k_e(\omega_1)\right]\tilde{U}_{e,1}(\omega-\omega_1)e^{-ik_e(\omega_1)z}\\=&-i\frac{\omega\bar{\chi}_{e;ee}^{(2)}}{cn_e(\omega)}\cdot F\left[\frac{1}{2}U_{e,1}^*U_{e,2}e^{i\omega_1 t-iz[k_e(\omega_2)-k_e(\omega_1)]}\right]\\=&-i\frac{\omega\bar{\chi}_{e;eee}^{(3)}}{cn_e(\omega)}\cdot F\left[\left(\frac{3}{8}|U_{e,1}|^2+\frac{3}{4}|U_{e,2}|^2\right)U_{e,1}e^{i\omega_1 t-ik_e(\omega_1)z}\right]\end{aligned}\tag{2.59}$$

$$\begin{aligned}&\frac{\partial\tilde{U}_{e,2}(\omega-\omega_2)}{\partial z}e^{-ik_e(\omega_2)z}+i\left[k_e(\omega)-k_e(\omega_2)\right]\tilde{U}_{e,2}(\omega-\omega_2)e^{-ik_e(\omega_2)z}\\=&-i\frac{\omega\bar{\chi}_{e;ee}^{(2)}}{cn_e(\omega)}\cdot F\left[\frac{1}{4}U_{e,1}^2e^{i\omega_2 t-i2k_e(\omega_1)z}\right]\\=&-i\frac{\omega\bar{\chi}_{e;eee}^{(3)}}{cn_e(\omega)}\cdot F\left[\left(\frac{3}{4}|U_{e,1}|^2+\frac{3}{8}|U_{e,2}|^2\right)U_{e,2}e^{i\omega_2 t-ik_e(\omega_2)z}\right]\end{aligned}\tag{2.60}$$

By seting $\Omega=\omega-\omega_1$, the dispersion term $k_e(\omega)-k_e(\omega_1)$ is Taylor expanded to:

$$k_e(\omega)-k_e(\omega_1)=\sum\nolimits_{m=1}^{\infty}\frac{(-i)^m(i\Omega)^m\cdot k_e^{(m)}(\omega=\omega_1)}{m!}\tag{2.61}$$

Thus, using inverse Fourier transform, the CWEs Eq.(2.59) and Eq.(2.60) can be written in the time domain with a more simplified expression, i.e.:

$$\begin{aligned}&\frac{\partial U_{e,1}(z,t)}{\partial z}+i\left[\sum\nolimits_{m=1}^{\infty}\frac{(-i)^m\cdot k_e^{(m)}(\omega=\omega_1)}{m!}\left(\frac{\partial}{\partial t}\right)^m\right]U_{e,1}\\&\quad=-i\frac{\bar{\chi}_{e;ee}^{(2)}}{cn_e(\omega_1)}\left(\omega_1-i\frac{\partial}{\partial t}\right)\cdot\left(\frac{1}{2}U_{e,1}^*U_{e,2}e^{-iz[k_e(\omega_2)-2k_e(\omega_1)]}\right)\\&\quad=-i\frac{\bar{\chi}_{e;eee}^{(3)}}{cn_e(\omega_1)}\left(\omega_1-i\frac{\partial}{\partial t}\right)\cdot\left(\left(\frac{3}{8}|U_{e,1}|^2+\frac{3}{4}|U_{e,2}|^2\right)U_{e,1}\right)\end{aligned}\tag{2.62}$$

$$\begin{aligned}
&\frac{\partial U_{e,2}(z,t)}{\partial z} + i\left[\sum\nolimits_{m=1}^{\infty} \frac{(-i)^m \cdot k_e^{(m)}(\omega=\omega_2)}{m!}\left(\frac{\partial}{\partial t}\right)^m\right] U_{e,2} \\
&\quad = -i\frac{\bar{\chi}_{e;ee}^{(2)}}{cn_e(\omega_2)}\left(\omega_2 - i\frac{\partial}{\partial t}\right)\cdot\left(\frac{1}{2}U_{e,1}^2 e^{-iz[2k_e(\omega_1)-k_e(\omega_2)]}\right) \\
&\quad = -i\frac{\bar{\chi}_{e;eee}^{(3)}}{cn_e(\omega_2)}\left(\omega_2 - i\frac{\partial}{\partial t}\right)\cdot\left(\left(\frac{3}{4}|U_{e,1}|^2 + \frac{3}{8}|U_{e,2}|^2\right)U_{e,2}\right)
\end{aligned} \tag{2.63}$$

Furthermore, in a moving frame with the speed same to the group velocity of the FW, i.e. $\tau = t - k_e^{(1)} z$, full CWEs regarding the quadratic SHG as well as the cubic Kerr and Raman effects are derived, i.e.:

$$\begin{aligned}
&\left(\frac{\partial}{\partial z} + iD_{e,1}\right)U_{e,1}(\tau,z) \\
&= -i\frac{\bar{\chi}_{e;ee}^{(2)}}{cn_e(\omega_1)}\left(\omega_1 - i\frac{\partial}{\partial \tau}\right)\cdot\left[\frac{1}{2}U_{e,1}^* U_{e,2} e^{-i\Delta k z}\right] \\
&\quad -i\frac{\bar{\chi}_{e;eee}^{(3)}}{cn_e(\omega_1)}\left(\omega_1 - i\frac{\partial}{\partial \tau}\right)\cdot\left\{(1-f_R)\left[\left(\frac{3}{8}|U_{e,1}|^2 + \frac{3}{4}|U_{e,2}|^2\right)U_{e,1}\right]\right. \\
&\qquad \left. + f_R\cdot\left[\frac{1}{4}h_R(\tau)\otimes\left(|U_{e,1}|^2 + |U_{e,2}|^2\right)U_{e,1}\right]\right\}
\end{aligned} \tag{2.64}$$

$$\begin{aligned}
&\left(\frac{\partial}{\partial z} - d_{12}\frac{\partial}{\partial \tau} + iD_{e,2}\right)U_{e,2}(\tau,z) \\
&= -i\frac{\bar{\chi}_{e;ee}^{(2)}}{cn_e(\omega_2)}\left(\omega_2 - i\frac{\partial}{\partial \tau}\right)\cdot\left[\frac{1}{4}U_{e,1}^2 e^{i\Delta k z}\right] \\
&\quad -i\frac{\bar{\chi}_{e;eee}^{(3)}}{cn_e(\omega_2)}\left(\omega_2 - i\frac{\partial}{\partial \tau}\right)\cdot\left\{(1-f_R)\left[\left(\frac{3}{4}|U_{e,1}|^2 + \frac{3}{8}|U_{e,2}|^2\right)U_{e,2}\right]\right. \\
&\qquad \left. + f_R\cdot\left[\frac{1}{4}h_R(\tau)\otimes\left(|U_{e,1}|^2 + |U_{e,2}|^2\right)U_{e,2}\right]\right\}
\end{aligned} \tag{2.65}$$

where the dispersion term $D_{e,1,2} = \sum_{m=2}^{\infty} \frac{(-i)^m \cdot k_e^{(m)}(\omega=\omega_{1,2})}{m!}\left(\frac{\partial}{\partial \tau}\right)^m$, the group velocity mismatch is defined as $d_{12} = k_e^{(1)}(\omega_1) - k_e^{(1)}(\omega_2)$, the phase mismatch is defined as $\Delta k = k_e(\omega_2) - 2k_e(\omega_1)$.

Above CWEs can also be scaled to the dimensionless form with following definitions:

$$\begin{aligned}
L_{D,1} &= sgn(k_1^{(2)})\frac{T_{in,1}}{k_1^{(2)}} \\
I_{in,1} &= U_1^2(z=0,\tau=0)\left(\frac{\varepsilon_0 n_1 c}{2}\right)
\end{aligned} \tag{2.66}$$

$$\xi = \frac{z}{L_{D,1}},\ \hat{\tau} = \frac{\tau}{T_{in,1}},\ \hat{\omega}_{1,2} = \omega_{1,2}T_{in,1},\ \eta = \frac{n_1}{n_2} \tag{2.67}$$

$$\begin{aligned}\hat{d}_{12} &= d_{12}\frac{L_{D,1}}{T_{in,1}},\ \Delta\hat{k} = \Delta k \cdot L_{D,1} \\ \hat{D}_{1,2} &= L_{D,1} \cdot \sum\nolimits_{m=2}^{\infty} \frac{(-i)^m \cdot k_{1,2}^{(m)}}{m! \cdot T_{in,1}^m}\left(\frac{\partial}{\partial\hat{\tau}}\right)^m\end{aligned} \tag{2.68}$$

$$\hat{U}_1 = \sqrt{\frac{U_1^2\frac{\varepsilon_0 n_1 c}{2}}{I_{in,1}}},\ \hat{U}_2 = \sqrt{\frac{U_2^2\frac{\varepsilon_0 n_2 c}{2}}{I_{in,1}}} \tag{2.69}$$

$$\kappa_{quad} = \frac{L_{D,1}\left(\frac{I_{in,1}}{\varepsilon_0 n_1 c/2}\right)^{\frac{1}{2}} \cdot \left(\frac{\bar{\chi}_{e;ee}^{(2)}}{2}\right) \cdot \omega_1}{c(n_2 n_1)^{\frac{1}{2}}}$$

$$\kappa_{cubic} = \frac{3}{8}\frac{L_{D,1}\frac{I_{in,1}}{\varepsilon_0 n_1 c/2} \cdot \bar{\chi}_{e;eee}^{(3)} \cdot \omega_1}{c n_1} \tag{2.70}$$

where the subscript "e" is omitted, $L_{D,1}$ is known as the dispersion length, $T_{in,1}$ indicates the pump pulse duration, $I_{in,1}$ is the peak intensity of the pump pulse, $k_{1,2}^{(m)} = k_e^{(m)}(\omega_{1,2})$. It is noted that all these parameters are dimensionless, which will bring convenience in the following derivation of the nonlinear Schrödinger-like (NLS-like) equation.

The dimensionless CWEs are:

$$\begin{aligned}&(i\frac{\partial}{\partial\xi} - \hat{D}_1)\hat{U}_1(\hat{\tau},\xi) \\ &\quad= +\kappa_{quad}\left(1 - \frac{i}{\hat{\omega}_1}\frac{\partial}{\partial\hat{\tau}}\right)\cdot\left[\hat{U}_1^*\hat{U}_2 e^{-i\Delta\hat{k}\xi}\right] \\ &\qquad+\kappa_{cubic}\left(1 - \frac{i}{\hat{\omega}_1}\frac{\partial}{\partial\hat{\tau}}\right)\cdot\left\{(1-f_R)\left[\left(|\hat{U}_1|^2 + 2\eta|\hat{U}_2|^2\right)\hat{U}_1\right]\right. \\ &\qquad\qquad\left.+f_R\cdot\left[\frac{2}{3}h_R(\hat{\tau})\otimes\left(|\hat{U}_1|^2 + \eta|\hat{U}_2|^2\right)\hat{U}_1\right]\right\}\end{aligned} \tag{2.71}$$

$$\begin{aligned}&(i\frac{\partial}{\partial\xi} - i\hat{d}_{12}\frac{\partial}{\partial\hat{\tau}} - \hat{D}_2)\hat{U}_2(\hat{\tau},\xi) \\ &\quad= +\kappa_{quad}\left(1 - \frac{i}{\hat{\omega}_2}\frac{\partial}{\partial\hat{\tau}}\right)\cdot\left[\hat{U}_1^2 e^{i\Delta\hat{k}\xi}\right] \\ &\qquad+\kappa_{cubic}\left(1 - \frac{i}{\hat{\omega}_2}\frac{\partial}{\partial\hat{\tau}}\right)\cdot 2\eta^2\left\{(1-f_R)\left[\left(2\eta^{-1}|\hat{U}_1|^2 + |\hat{U}_2|^2\right)\hat{U}_2\right]\right. \\ &\qquad\qquad\left.+f_R\cdot\left[\frac{2}{3}h_R(\hat{\tau})\otimes\left(\eta^{-1}|\hat{U}_1|^2 + |\hat{U}_2|^2\right)\hat{U}_2\right]\right\}\end{aligned} \tag{2.72}$$

CWEs can also be numerically solved by the split-step Fourier method. The advantage of using CWEs is that these envelope equations don't have serious requirement of the sampling points on the electric field, which may hugely

speed up the simulation. On the other hand, besides the critical approximation, CWEs always have limited harmonics and limited types of nonlinear interactions being investigated. Although more equations may be added to extend the investigation, the system actually becomes quite complicated.

2.5 Nonlinear Schrödinger-like (NLS-like) Equation

In a largely phase mismatched SHG, namely $\Delta k \cdot L \gg 2\pi$ where L is the length of the medium, the conversion between the FW and the SH is very weak. So there are no strong SH being generated. Instead, the light converted from the FW to the SH will after a short propagation length back-convert. This process will repeatedly occur along the crystal (cascading) and thereby induce a nonlinear, intensity dependent phase shift on the FW, called the cascaded quadratic nonlinearity. In the assumption of an undepleted FW, the SH is further defined as, $\hat{U}_2 = \varphi(\hat{\tau})e^{i\Delta k}$. Using such ansatz in Eq.(2.72) and eliminating the cubic nonlinearity, we have:

$$\hat{U}_2(\hat{\tau},\xi) = -\frac{\kappa_{quad}}{\Delta\hat{k}}\left(1 - \frac{i}{\hat{\omega}_2}\cdot\frac{\partial}{\partial\hat{\tau}}\right)\left(h_c(\hat{\tau}) \otimes \hat{U}_1^2\right)\cdot e^{i\Delta\hat{k}\xi} \tag{2.73}$$

where

$$\begin{aligned} F[h_c(\hat{\tau})] = \tilde{h}_c(\hat{\Omega}) &= \frac{\Delta\hat{k}}{\Delta\hat{k}_{casc}} \\ \Delta\hat{k}_{casc}(\hat{\Omega}) &= k(\frac{\hat{\Omega}+\hat{\omega}_2}{T_{in,1}}) - 2(k_1 + k_1^{(1)}\cdot\frac{\hat{\Omega}}{2}) \end{aligned} \tag{2.74}$$

Physically, the denominator $\Delta\hat{k}_{casc}$ reflects the phase mismatch between a "solitary" FW with dispersionless phase and the SH, and $\Delta\hat{k}_{casc} = 0$ implies the phase matching, which is different to the commonly known $\Delta\hat{k}$ in a SHG that both the FW and SH have dispersive phases. $\Delta\hat{k}_{casc} = 0$ also leads to a divergent $\tilde{h}_c(\hat{\omega})$ which is unfortunately unacceptable in a simulation. To avoid the divergence, a loss factor may be added to the SH equation and the response is modified to have a convergent form, reads: $\tilde{h}_c(\hat{\Omega}) = \frac{\Delta\hat{k}}{\Delta\hat{k}_{casc}+i\alpha}$, where $\alpha < 0$ indicates a loss term, $-\alpha\hat{U}_2$, is inserted in the left side of Eq.(2.72).

Using Eq.(2.73) in the FW equation Eq.(2.71) gives a single function governing the FW in the largely phase mismatched SHG process, namely the

nonlinear Schrödinger-like (NLS-like) equation:

$$\begin{aligned}
&(i\frac{\partial}{\partial\xi}-\hat{D}_1)\hat{U}_1(\hat{\tau},\xi)\\
=&-\frac{\kappa_{quad}^2}{\Delta\hat{k}}\left(1-\frac{i}{\hat{\omega}_1}\cdot\frac{\partial}{\partial\hat{\tau}}\right)\cdot\left[\hat{U}_1^*\left(1-\frac{i}{\hat{\omega}_2}\cdot\frac{\partial}{\partial\hat{\tau}}\right)\left(h_c(\hat{\tau})\otimes\hat{U}_1^2\right)\right]\\
&+\kappa_{cubic}\left(1-\frac{i}{\hat{\omega}_1}\cdot\frac{\partial}{\partial\hat{\tau}}\right)\cdot\left\{(1-f_R)\left[\left(|\hat{U}_1|^2+2\eta\frac{\kappa_{quad}^2}{\Delta\hat{k}^2}|\hat{U}_1|^4\right)\hat{U}_1\right]\right.\\
&\left.+f_R\cdot\left[\frac{2}{3}h_R(\hat{\tau})\otimes\left(|\hat{U}_1|^2+\eta\frac{\kappa_{quad}^2}{\Delta\hat{k}^2}|\hat{U}_1|^4\right)\hat{U}_1\right]\right\}
\end{aligned}\tag{2.75}$$

in which the Kerr SPM effects on the right side can be abstracted out as:

$$\left(-\frac{\kappa_{quad}^2}{\Delta\hat{k}}+\kappa_{cubic}\right)|\hat{U}_1|^2\hat{U}_1 \tag{2.76}$$

The pre-factor is understood as the dimensionless soliton number which is resulted from the competition between the cascaded quadratic nonlinearity, $N_{casc}^2=sgn(\Delta\hat{k})\frac{\kappa_{quad}^2}{\Delta\hat{k}}$, and the material cubic nonlinearity, $N_{cubic}^2=\kappa_{cubic}$. The nonlinear refractive index representing the intensity related nonlinear phase change on the FW is:

$$\begin{aligned}
n_{2,casc}&=-\frac{2\left(\frac{\bar{\chi}_{e;ee}^{(2)}}{2}\right)^2\omega_1}{\varepsilon_0c^2n_2n_1^2\Delta k}\\
n_{2,cubic}&=\frac{3\bar{\chi}_{e;eee}^{(3)}}{4\varepsilon_0cn_1^2}
\end{aligned}\tag{2.77}$$

where the "$-$" sign indicates that the cascaded quadratic nonlinearity shows self-defocusing when having a positive-valued Δk.

Therefore:

$$\begin{aligned}
N_{casc}^2&=\frac{\omega_1}{c}L_{D,1}I_{in,1}\,|n_{2,casc}|\\
N_{cubic}^2&=\frac{\omega_1}{c}L_{D,1}I_{in,1}n_{2,cubic}
\end{aligned}\tag{2.78}$$

Moreover, the FW can be decomposed to the amplitude and phase terms, i.e.: $\hat{U}_1=\mathscr{A}(\xi,\hat{\tau})e^{i\phi(\xi,\hat{\tau})}$, and their dynamics can be concluded as:

$$\frac{\partial\mathscr{A}}{\partial\xi}=\left(\frac{4N_{casc}^2-3N_{cubic}^2}{\hat{\omega}_1}+2\hat{\tau}_cN_{casc}^2\right)\mathscr{A}^2\frac{\partial\mathscr{A}}{\partial\hat{\tau}}+\text{HOD} \tag{2.79}$$

$$\begin{aligned}\frac{\partial\phi}{\partial\xi} = N_{eff}^2\mathscr{A}^2 - 2\hat{\tau}_R N_{cubic}^2\mathscr{A}\frac{\partial\mathscr{A}}{\partial\hat{\tau}} \\ + \left(\frac{2N_{casc}^2 - N_{cubic}^2}{\hat{\omega}_1} + 2\hat{\tau}_c N_{casc}^2\right)\mathscr{A}^2\frac{\partial\phi}{\partial\hat{\tau}} + \text{HOD}\end{aligned} \tag{2.80}$$

where:

$$N_{eff}^2 = N_{casc}^2 - N_{cubic}^2 \tag{2.81}$$

$$\begin{aligned}\hat{\tau}_c &= -i\int d\hat{\tau}\cdot\hat{\tau}\cdot h_c(\hat{\tau}) = \tilde{h}_c'(0) = \frac{\hat{d}_{12}}{\Delta\hat{k}} \\ \hat{\tau}_R &= f_R\int d\hat{\tau}\cdot\hat{\tau}\cdot h_R(\hat{\tau}) = if_R\cdot\tilde{h}_R'(0) = -f_R\text{Im}[\tilde{h}_R'(0)]\end{aligned} \tag{2.82}$$

Here, the cascaded and Raman responses are all expanded to the first order while higher order terms (HOD) are neglected. In the amplitude equation, the second term in the right-side bracket indicates that the cascaded response, or more precisely the first-order response, actually induces self-steepening effects on the pulse amplitude, which will give rise to pulse shock front and with the existence of dispersion, makes change on the pulse group velocity (GV). In the phase equation, on the other hand, the first term on the right side indicates the overall SPM effects resulted from the nonlinearity competition. The second term implies that the first order of the Raman response will give rise to shock front on the pulse phase, namely the phase shift or, in frequency domain, the frequency shift. The third term can be neglected when the pulse is solitary, namely the phase profile is flat over the delay axis so that the derivative is zero.

2.6 Conclusion

As a conclusion, in this chapter we derived three numerical models for estimating pulse propagating dynamics in nonlinear media. Starting from the Maxwell equation, the forward Maxwell equation is first derived with minimal approximations (SVSAA), which is further expanded to the NWEF with interpretations of the nonlinear induced polarizations. NWEF directly deals with the electric field (component) and automatically include all types of quadratic and cubic nonlinear interactions, making it a generalized model which has been widely used nowadays. Then, with the approximation that different harmonics within the electric field do not have spectral overlap, which is equivalent to the commonly known slowly varying envelope approximation (SVEA), CWEs regarding the noncritical SHG process is derived. The envelope dynamics of the FW and the SH are both formulated. Cubic Kerr effects (SPM and XPM) and

the Raman effects are also included in the equations. It should be noticed that CWEs have limited harmonics as well as limited types of nonlinear interactions being investigated. The third model is the NLS-like equation which is derived in the largely phase mismatched SHG process. With such a condition, there are no strong SH being generated, but instead, the weak and repeated light conversion between the FW and the SH will induce a nonlinear phase shift on the FW, called the cascaded quadratic nonlinearity which performs just like the material Kerr nonlinearity that gives rise to the SPM effect. In the dimensionless form, the soliton number marking the efficiency of the SPM effect is concluded, which is actually the sum of the cascaded and Kerr nonlinearities.

To make simulations, all three models are programmed and numerically solved. On Matlab platform, each model is wrapped as a solver, see appendix for the codes.

Bibliography

[1] A. Yariv and P. Yeh, *Photonics: Optical Electronics in Modern Communications*, The Oxford Series in Electrical and Computer Engineering (Oxford University Press, Incorporated, 2007).

[2] R. Boyd, *Nonlinear Optics*, Nonlinear Optics Series (Elsevier Science, 2008).

[3] G. Agrawal, *Nonlinear Fiber Optics*, Academic Press (Academic Press, 2013).

[4] M. Conforti, F. Baronio, and C. De Angelis, "Ultrabroadband optical phenomena in quadratic nonlinear media," IEEE Photon. J. **2**, 600–610 (2010).

[5] M. Kolesik, P. Townsend, and J. Moloney, "Theory and simulation of ultrafast intense pulse propagation in extended media," IEEE J. Sel. Topics Quantum Electron. **18**, 494–506 (2012).

[6] R. K. Bullough, P. M. Jack, P. W. Kitchenside, and R. Saunders, "Solitons in laser physics," Physica Scripta **20**, 364 (1979).

[7] A. Husakou and J. Herrmann, "Supercontinuum generation of higher-order solitons by fission in photonic crystal fibers," Phys. Rev. Lett. **87**, 203901 (2001).

[8] M. Conforti, F. Baronio, and C. De Angelis, "Nonlinear envelope equation for broadband optical pulses in quadratic media," Phys. Rev. A **81**, 053841 (2010).

[9] M. Conforti, F. Baronio, and C. De Angelis, "Modeling of ultrabroadband and single-cycle phenomena in anisotropic quadratic crystals," J. Opt. Soc. Am. B **28**, 1231–1237 (2011).

[10] C. Phillips, C. Langrock, J. Pelc, M. Fejer, I. Hartl, and M. Fermann, "Supercontinuum generation in quasi-phasematched waveguides," Opt. Express **19**, 18754–18773 (2011).

[11] M. Bache, "Scaling laws for soliton pulse compression by cascaded quadratic nonlinearities," J. Opt. Soc. Am. B **24**, 2752–2762 (2007).

Chapter 3

CQSC in Quadratic Nonlinear Bulk Crystals

3.1 Introduction

In this chapter, we numerically investigate the cascaded quadratic soliton compression (CQSC) in nonlinear bulk crystals, by using the NWEF models derived in chapter 2. As is made clear in chapter 1, CQSC is accomplished under a self-defocusing nonlinearity contributed by the cascaded quadratic nonlinearity and with the normal dispersion. Basically, there are varieties of nonlinear crystals that could produce strong and self-defocusing cascaded quadratic nonlinearities with decent nonlinear susceptibilities [1], and having materials cubic Kerr nonlinearities being counterbalanced, namely $|n_{2,casc}| > n_{2,cubic}$ or $N^2_{casc} > N^2_{cubic}$ in the dimensionless form. Here, three crystals are investigated, i.e. the most used quadratic crystals barium borate (BBO) and lithium niobate (LN) focusing on the visible and near infrared range (near-IR), and a novel crystal lithium thioindate (LIS) targeting applications in the mid-infrared range (mid-IR). Different types of configurations of the crystal are employed aiming at exploiting the largest quadratic susceptibility. The tunability of the cascading is also studied, which indicates the tuning on both the amplitude of the SPM effect of an over-all self-defocusing nonlinearity and the cascading induced self-steepening effect. As the result of CQSC, high-intensity, few-cycle or even single-cycle, solitary laser pulses are generated in both near-IR and mid-IR, accompanied with supercontinuum generations and dispersive wave generations at even longer wavelengths.

3.2 CQSC in Barium Borate (BBO) Crystal

CQSCs in BBO crystals have been widely reported, both numerically and experimentally [2–4]. The crystal is always cut for critical quadratic nonlinear interactions, namely the so-called type-I (e;oo) or type-II (o;eo) interaction, in which the extraordinary ("e") wave has the refractive index (or the spatial phase) dependent on the angle (θ) between the incident light beam and the crystal optic axis, see section B. Such a configuration makes use of the largest quadratic nonlinear susceptibility in BBO, i.e. $d_{22} = \bar{\chi}^{(2)}_{y;yy}/2$ with:

$$\bar{\chi}^{(2)}_{e;oo/o;eo} = 2\left[-d_{22}cos(\theta)sin(3\varphi) + d_{31}sin(\theta)\right] \tag{3.1}$$

where $d_{31} = \bar{\chi}^{(2)}_{z;xx}/2$. (x, y, z) is the principal axis of the crystal in which the axis z marks the optic axis. φ is the rotation angle with respect to z. Besides tuning the susceptibility, the variable θ also plays the role in tuning the

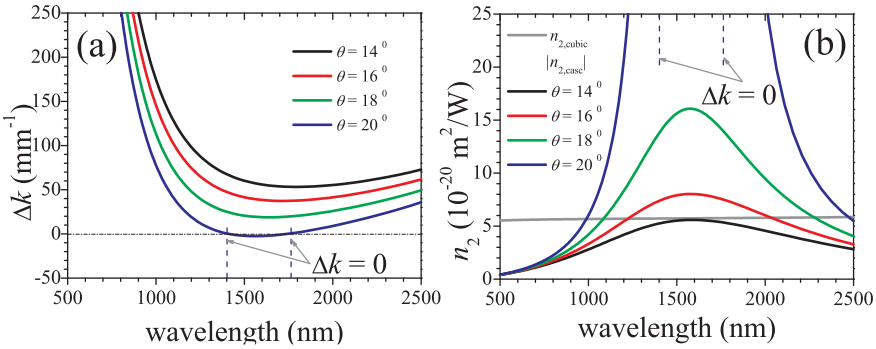

Fig. 3.1: tunability of the phase mismatch Δk and the cascaded quadratic nonlinearity (shown in $n_{2,casc}$) as a function of FW wavelength, under different angle values. Quadratic and cubic susceptibilities used are $d_{22} = 2.2$ (pm/V), $d_{31} = -0.16$ (pm/V), $\bar{\chi}^{(3)}_{o;ooo} = 550$ (pm^2/V^2) [5]. $\varphi = -\frac{\pi}{2}$. The Sellmeier function of the birefringence of BBO is obtained from the handbook [6].

phase mismatch Δk and therefore tunes the cascaded quadratic nonlinearity (as $n_{2,casc} \propto \Delta k^{-1}$). The competing nonlinearity is the material intrinsic Kerr nonlinearity on the FW which is an ordinary ("o") wave, so the corresponding susceptibility is the angle-independent $\bar{\chi}^{(3)}_{o;ooo}$.

Figure 3.1 shows the tunability of Δk as well as $n_{2,casc}$, by tuning the angle θ. With an increase of θ, Δk is reduced and may even find phase matching. Although the susceptibility $\bar{\chi}^{(2)}_{e;oo/o;eo}$ is also reduced through the Cosine function in Eq.(3.1), the cascaded quadratic nonlinearity is getting increased and a wavelength band with the cascading winning over the Kerr nonlinearity, i.e. $|n_{2,casc}| > n_{2,cubic}$, emerges. Therefore, overall self-defocusing nonlinearity is produced within the band.

It should be noticed that when approaching to the phase matching position, see the case with $\theta = 20^0$ where $\Delta k = 0$ is found at both 1400 nm and 1764 nm, the estimation of $n_{2,casc}$, mathematically becoming infinity, is not accurate since the cascading (which requires the condition of the largely phase mismatch) is no longer promised. Nevertheless, when $\Delta k < 0$, the cascading actually contributes to the self-focusing effects. Therefore, an effective estimation on the self-defocusing $n_{2,casc}$ actually requires the positive-valued Δk far away from the phase matching position.

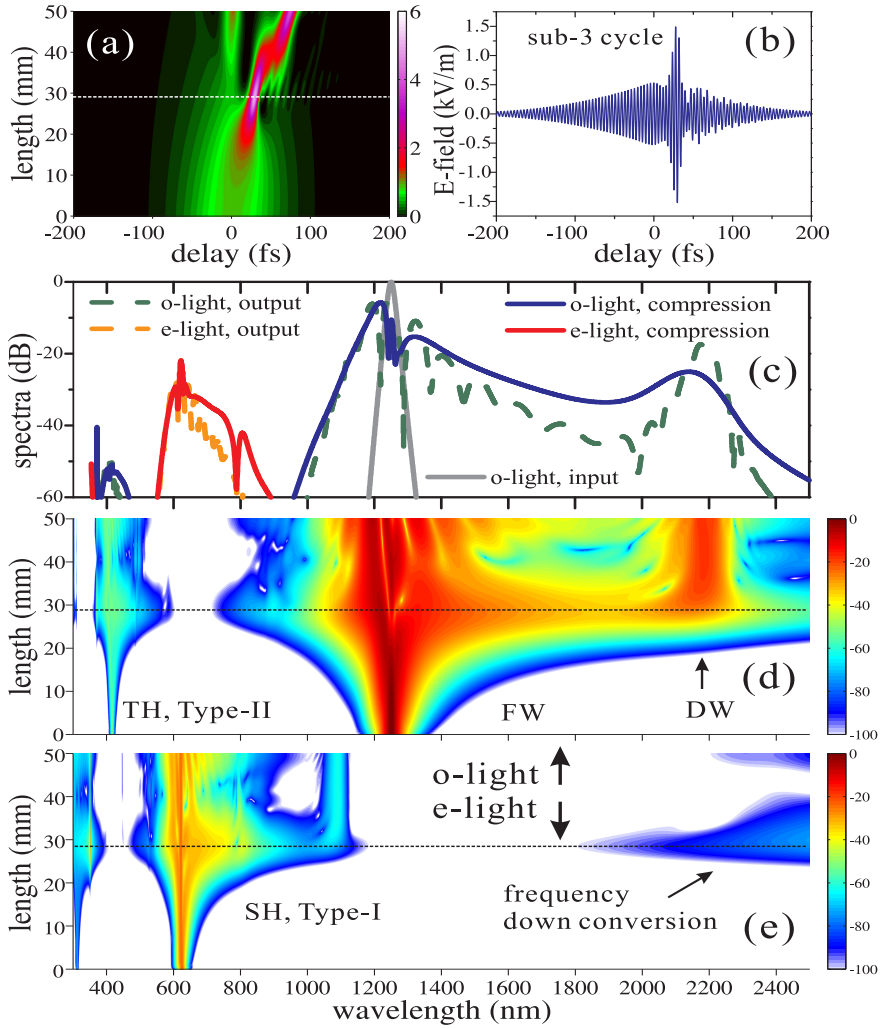

Fig. 3.2: CQSC in BBO cut for critical quadratic nonlinear interaction; $\theta = 18^0$, $\varphi = -\frac{\pi}{2}$, $I_{in,1} = 100$ GW/cm^2, FWHM $= 100$ fs, pump wavelength is 1250 nm, $f_R = 0$, soliton number $N_{eff} \approx 5.0$; (a) pulse temporal evolution with the dashed line marking the compression position; (b) the electric-field (E-field) of the pulsed laser at the compression position; (c) spectra of both ordinary (o-) and extraordinary light (e-light) at input, compression and output positions; (d) spectral evolution of o-light; (e) spectral evolution of e-light.

On the other hand, CQSC requires the normal dispersion so that the non-

linear phase shift induced by the self-defocusing SPM can be cancelled and the solitary pulses can be created. By calculating the group velocity dispersion (GVD) as a function of the frequency, i.e. the parameter $k^{(2)}_{o;o}(\omega)$, the normal dispersion range of the ordinary wave in BBO ($k^{(2)}_{o;o} > 0$) is found covering short wavelengths and being stopped at a zero dispersion wavelength (ZDW) of around 1480nm, which means the operational wavelength of CQSC is limited below such a ZDW.

For example, in the case with $\theta = 18^0$, the operational wavelength range for the CQSC is ($1070 \sim 1480$ nm) though the window of the overall-self-defocusing nonlinearity is up to 2260 nm, and with $\theta = 20^0$ the range is ($990 \sim 1400$ nm) stopped by the phase matching wavelength.

Another concern is on the cascading phase mismatch Δk_{casc} [7, 8], which might find sideband phase matching between a dimensionless solitary FW and the SH [9]. With strong normal dispersion and having $\Delta k > 0$ over the whole wavelength range, the cascading phase mismatch can be estimated as:

$$\Delta k_{casc}(\omega) \approx \Delta k(\omega) + \frac{1}{2} k^{(2)}_{o;o}(2\omega - 2\omega_1)^2 + HOD > 0 \tag{3.2}$$

where ω_1 indicates the wavelength of the pump pulsed laser. Thus, the cascaded response will be ultra-broadband in spectrum and fast decayed in time, namely the quasi-instantaneous response which will lead to a clean pulse profile in the CQSC.

Figure 3.2 shows the numerical simulation of CQSC in the BBO crystal cut for the critical interaction, i.e. $\theta = 18^0$ and $\varphi = -\frac{\pi}{2}$. To track the dynamics of the birefringence of the crystal, a group of NWEF consisting of two equations governing both "o" and "e" waves is employed. f_R is set to zero since BBO has weak Raman response between the birefringence. The pump pulsed laser is at 1250 nm. The pulse duration is 100 fs at full width and half maximum (FWHM). With such a configuration, the soliton number N_{eff} is estimated to be around 8.8.

With a crystal length of 3 cm, the laser pulse is compressed to have sub-3-cycle duration while the peak intensity is increased by around 6 times, see Fig. 3.2(a,b). In spectrum, significant spectral broadening is observed by the SPM effect of the overall self-defocusing nonlinearity, see Fig. 3.2(c,d). At the compression position where the pulse spectrum is most broadened, dispersive wave (DW) is evoked due to perturbations of high order dispersion (such as the third-order dispersion), which will be further discussed in the following

chapter. The frequency (wavelength) position of the DW is predicted by the phase matching condition [10]:

$$k(\omega_r) = k(\omega_1) + k^{(1)}(\omega_r - \omega_1) + \frac{|\gamma I_{in,1}|}{2} \tag{3.3}$$

where ω_r indicates the DW frequency. The first right-side term the equation again reflects the dispersionless solitary FW. $\gamma = \frac{\omega_1}{c}(n_{2,casc} + n_{2,Kerr})$ indicates the nonlinear factor.

Besides the SPM effects, cascading induced self-steepening is found on the FW pulse [11], according to Eq.(2.76), which gives rise to pulse shock front, frequency shift as well as the group velocity (GV) change (pulse delay change in the temporal evolution Fig. 3.2(a)).

It is also noticed that "e" SH is generated through the type-I interaction, and the energy is low due to the phase mismatch, see Fig. 3.2(e). The SH looks exactly like a slight copy from the FW, with features of the spectral broadening and the DW generation both duplicated. Moreover, higher order harmonics such as the third harmonic (TH) and frequency down conversions are observed as well. These harmonics are actually generated through mixed interactions, e.g., the TH is generated through both the type-II interaction (with "o" FW and "e" SH) and the direct THG with the FW, the forth harmonic is generated through the type-I SFG (with "o" FW and "o" TH) and the type-0 (e;ee) SHG with the SH. It is the NWEF model that automatically includes all the possible harmonic generations and frequency mixing processes, making the simulation more generalized with all the details included. It is also verified that CQSC is quite solid in principle as potential harmonic generations do not impact the pulse compression as well as the generation of few-cycle laser pulses.

3.3 CQSC in Lithium Niobate (LN) Crystal

LN is another candidate for CQSC [14]. Unlike the BBO crystal, LN makes use of the non-critical quadratic nonlinear interaction, in which the polarization direction as well as the propagation direction of the incident laser beam is along the principal axis. Since the largest quadratic susceptibility in LN is $d_{33} = \bar{\chi}^{(2)}_{e;ee}/2$, the crystal is always z-cut ($\theta = 90^0$) and has light propagation in "e" waves so that a type-0 (e;ee) interaction making full use of $\bar{\chi}^{(2)}_{e;ee}$ is configured.

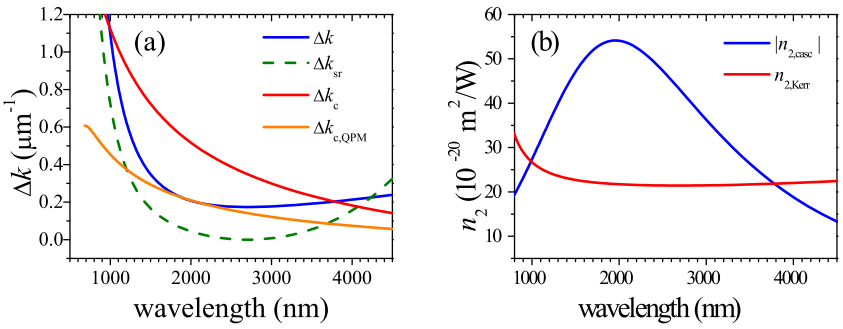

Fig. 3.3: the phase mismatch and nonlinearities as a function of the wavelength in z-cut LN; the quadratic susceptibility used is $d_{33} = 25$ pm/V at 1064 nm [12] and Miller scaling is used to estimate value at other wavelengths, $n_{2,Kerr}$ is calculated with the two-band model [13, 14]; the Sellmeier equation for LN is obtained from the handbook [6].

The phase mismatch Δk is then fixed. The tunability on cascading is achieved by inducing the quasi-phase-matching (QPM) on such a ferroelectric crystal through the periodic poling on the optic axis. With QPM, the phase mismatch is effectively tuned to:

$$\Delta k_{eff} = \Delta k - \frac{2\pi}{\Lambda} \tag{3.4}$$

where Λ indicates the QPM poling pitch. Δk_{eff} is called the effective phase mismatch.

However, it should be noticed that using QPM will impose a pre-factor, e.g. $\frac{2}{\pi}$ for the first order QPM, on the quadratic susceptibility, and therefore reduce the cascaded quadratic nonlinearity. In order to compensate such a decrease and even increase the nonlinearity, the phase mismatch should be tuned much smaller with $\Delta k_{eff} < \frac{4}{\pi^2}\Delta k$ [15].

On the other hand, LN is reported to have quite strong Raman response [12], $f_R > 50\%$, so the competing Kerr nonlinearity is $n_{2,Kerr} = (1 - f_R)n_{2,cubic}$, in which the cubic susceptibility is $\bar{\chi}^{(3)}_{e;eee}$. $n_{2,Kerr}$ is always characterized through the Z-Scan measurement with the crystal two-photon absorption (TPA) phenomenon in the crystal. It can also be formulated through a two-band model describing the TPA [13].

Figure 3.3 shows both the phase mismatch and competing nonlinearities in

a z-cut LN. The bulk LN, without QPM, is found naturally suitable as stronger self-defocusing cascaded quadratic nonlinearity is produced than the material Kerr nonlinearity over a broadband wavelength range, i.e. $|n_{2,casc}| > n_{2,Kerr}$ within the range $990 \sim 3750$ nm, see Fig. 3.3(b). Scaled in the phase mismatch parameter, the victory of the cascaded nonlinearity means that the phase mismatch is below an upper threshold Δk_c which lies behind the equation that $n_{2,casc}(\Delta k = \Delta k_c) + n_{2,Kerr} = 0$, see the red line in Fig. 3.3(a). Meanwhile, the cascading phase matching condition is also checked, which draws a lower threshold Δk_{sr} for the phase mismatch, implying that phase matching is supposed to be found with:

$$\Delta k_{casc,sr}(\Omega = \omega_c - 2\omega_1) = 0 \tag{3.5}$$

which leads to a resonant cascaded response and ω_c is the resonance frequency. The resonance will cause oscillations in pulse temporal profile and therefore degrade the CQSC.

Therefore, the condition for non-resonant and high-quality CQSC can be concluded as [7]:

$$\Delta k_{sr} < \Delta k < \Delta k_c \tag{3.6}$$

The bulk LN naturally fulfills such a condition so it is an excellent candidate. When using QPM, Δk_c is getting much smaller, but there is still space between two thresholds so that Δk_{eff} can be tuned in between to accomplish the CQSC.

It is also relevant that the normal dispersion of the "e" wave in z-cut LN stops at around 1920 nm. Therefore, the operational wavelength range for the CQSC in LN is ($990 \sim 1920$ nm) covering the whole communication band.

Figure 3.4 shows the CQSC in a 5-mm long z-cut LN. The pump wavelength is at 1300 nm. FWHM of the pump laser pulse is 50 fs, the pulse peak intensity is up to 200 GW/cm^2, the soliton number is around 2.8. The simulation is also done by the NWEF model.

Analogous to the case in BBO, this time, CQSC gives single-cycle pulse generation after the propagation of 1.5 mm (Fig. 3.4(a,b)) and the spectrum is extremely broadened over octaves (Fig. 3.4(c,d)). Since both the FW and SH are "e" waves and share the same polarization direction, the SH actually helps raise the blue side of such a supercontinuum. DW generation can still be observed, which raises the red side of the spectrum.

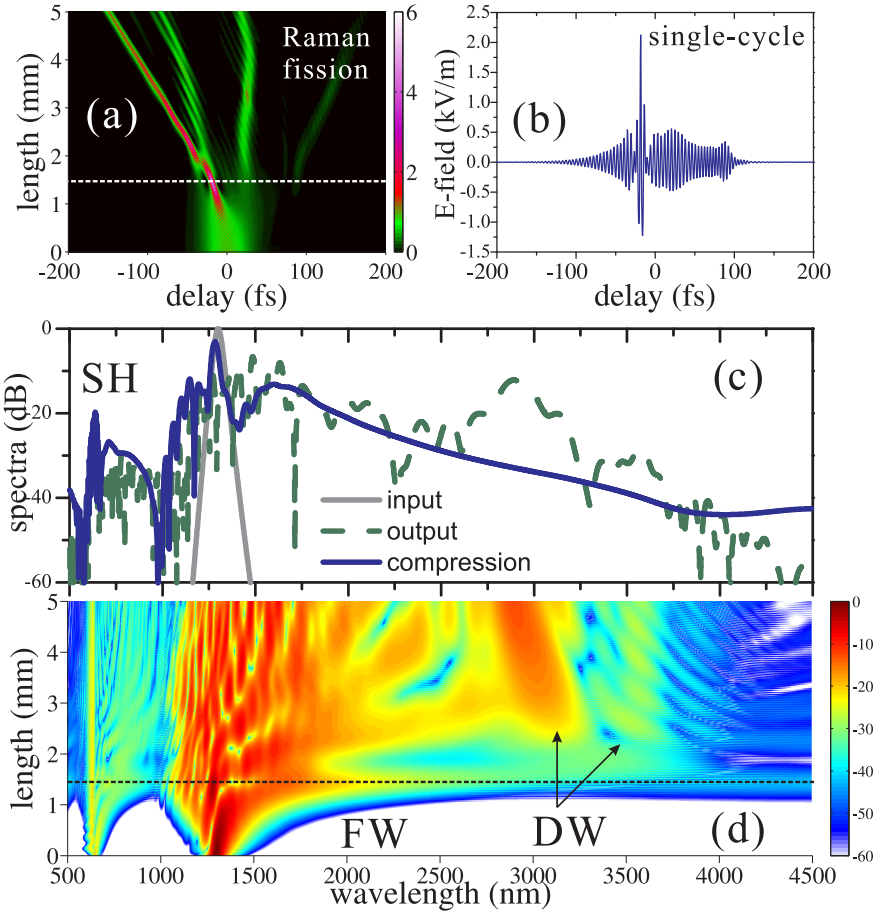

Fig. 3.4: CQSC in z-cut LN; $I_{in,1} = 200$ GW/cm^2, FWHM = 50 fs, pump wavelength is 1300 nm, $f_R = 70$, the Raman response function is from the paper, soliton number $N_{eff} \approx 2.8$; (a) pulse temporal evolution with the dashed line marking the compression position; (b) the electric-field (E-field) of the pulsed laser at the compression position; (c) spectra of e-light at input, compression and output positions; (d) spectral evolution of e-light.

The differences are: 1) the strong Raman fraction in the LN causes modulation instability on the pulse and results in pulse split phenomenon, called the Raman fission effects. With the soliton number large than unity, the pulse after the compression position is split into 3 branches; 2) the pulse spectrum is mainly red-shifted instead of the blue shift in the BBO case, and the pulse

temporal delay is also changed to the opposite direction with the GV getting increased. Meanwhile, the DW is blue shifted with the FW being red-shifted, following the phase matching condition; 3) the interaction length in the LN is much shorter as both GVD and the quadratic susceptibility are much larger than the BBO.

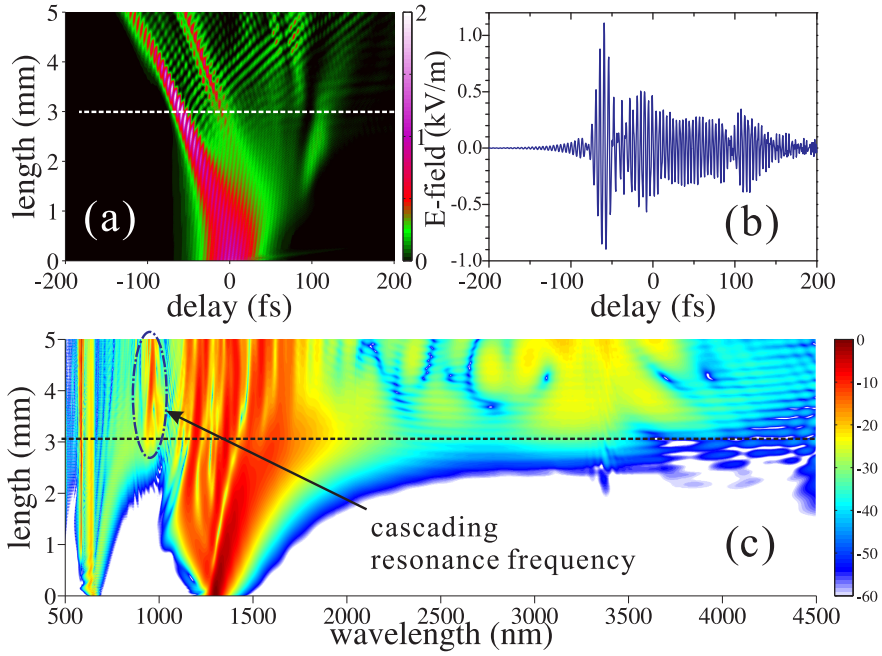

Fig. 3.5: CQSC in z-cut periodic poling LN; QPM pitch is 28 μm; pump pulse are the same to Fig. 3.4; soliton number $N_{eff} \approx 1.6$; (a) pulse temporal evolution with the dashed line marking the compression position; (b) the electric-field (E-field) of the pulsed laser at the compression position; (c) spectral evolution of e-light.

Pulse propagation in LN with a QPM structure is also investigated, see Fig. 3.5. The QPM pitch is 28 μm with which the phase mismatch is tuned from the original value $\Delta k = 501$ mm^{-1} to $\Delta k_{eff} = 277$ mm^{-1}, but it still can not compensate the decrease on the quadratic susceptibility. Therefore, with the same pump laser pulse, the cascaded quadratic nonlinearity is reduced and the soliton number in this case is around 1.6.

With a reduced soliton number, the pulse compression as well as the spectral

broadening are both degraded and longer propagation distance is required to meet the compression position. On the other hand, Δk_{eff} is actually below the lower threshold which is $\Delta k_{sr} = 283$ mm^{-1}, which then gives rise to extra resonance in the spectrum because of the cascading phase matching. The pulse temporal profile is significantly degraded by the impact of resonance induced strong oscillations. When the phase mismatch is located in such a resonant area, resonance frequencies can be predicted by solving the phase matching equation, see Fig. 3.6.

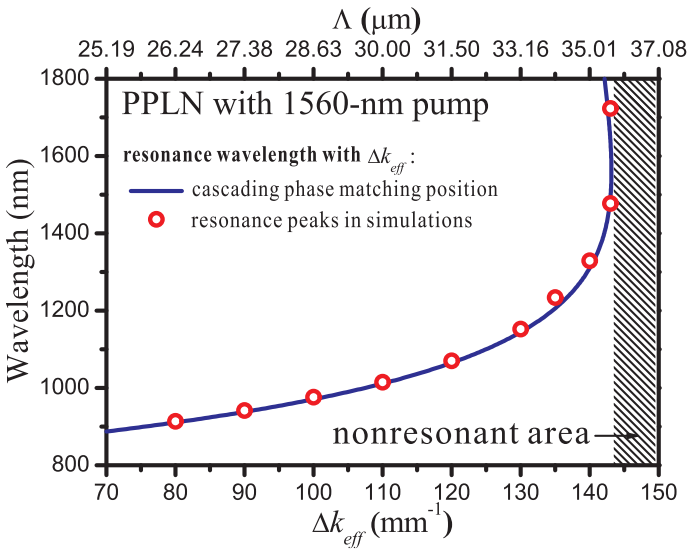

Fig. 3.6: calculated and numerically labeled resonance frequencies as a function of effective phase mismatch or QPM pitch, with the pump pulsed laser at 1560 nm

3.4 CQSC in Lithium Thioindate (LIS) Crystal

The scenario of CQSC also works in mid-IR, provided that 1) the quadratic nonlinear materials, crystals or semiconductors, have decent quadratic nonlinearity in mid-IR that could produce strong and self-defocusing cascaded nonlinearity; 2)the normal dispersion range of the material extends into the mid-IR. Novel crystals have been investigated and possible candidates are concluded in the paper [1]. Crystal LIS is listed as one of them, in which the

cascaded quadratic nonlinearity could counterbalance the Kerr nonlinearity within the mid-IR ($1.7 \sim 8.8$ μm), when being z-cut and configured for the interaction $(e; ee)$, see Fig. 3.7. Quadratic and cubic susceptibilities involved are $d_{33} = \bar{\chi}^{(2)}_{z;zz}$ and $\bar{\chi}^{(3)}_{z;zzz}$. Meanwhile, the normal dispersion in the crystal extends to 3.5 μm, making the CQSC possible at important mid-IR wavelengths such as at 2 μm targeting the thulium based lasers and at 3 μm for the Er:YAG based lasers. LIS is also ferroelectric, so the QPM can be used to gift the tunability on the cascading.

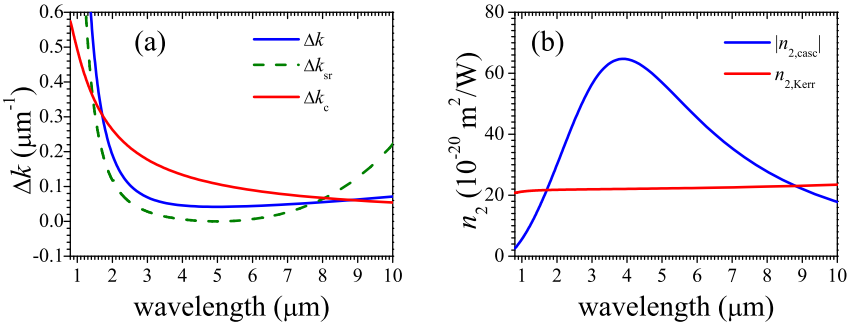

Fig. 3.7: the phase mismatch and nonlinearities as a function of the wavelength in LIS cut for the interaction $(e; ee)$; quadratic and cubic susceptibilities used are $d_{33} = \bar{\chi}^{(2)}_{z;zz}/2 = 15.6$ (pm/V), $\bar{\chi}^{(3)}_{z;zzz} = 4444$ (pm^2/V^2). $f_R = 20\%$. The Sellmeier function of the birefringence of BBO is obtained from the handbook [6].

Figure 3.8 shows the CQSC in LIS. The pump pulsed laser is at wavelength 3000 nm. The FWHM of the pulse is 150 fs in accordance to some commercial laser systems, the pulse peak intensity is 300 GW/cm^2. The soliton number is estimated to be 15.8. Single cycle pulse generation with clean profile is once more accomplished by the CQSC. During the spectral broadening, especially the first stage from input position to the compression position, the FW spectrum is quite symmetric, no blue or red shift. This is understood that the cascading induced blue-shift regime is balanced by the material Raman induced red shift. Correspondingly, the pulse temporal profile is symmetric as well, and the self-steepening induced shock front is well suppressed. Far in the mid-IR (5.8 μm) find we the DW generation, which is broadband with the generation efficiency around 5%.

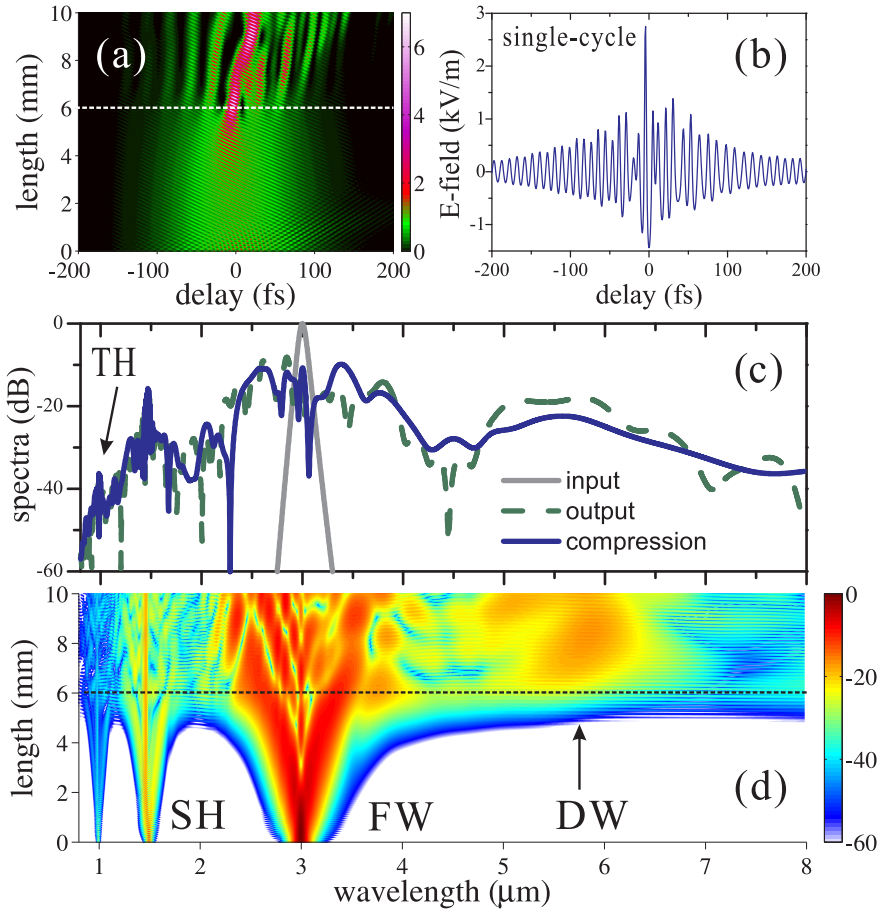

Fig. 3.8: CQSC in LIS with the interaction $(e; ee)$; $I_{in,1} = 300$ GW/cm^2, FWHM = 150 fs, pump wavelength is 3000 nm, $f_R = 20$, the Raman response function is from [16], soliton number $N_{eff} \approx 15.8$; (a) pulse temporal evolution with the dashed line marking the compression position; (b) the electric-field (E-field) of the pulsed laser at the compression position; (c) spectra of e-light at input, compression and output positions; (d) spectral evolution of e-light.

3.5 Conclusion

As a conclusion, in this chapter, we investigated CQSC in three quadratic nonlinear bulk materials, i.e. BBO, LN and LIS. CQSC can be achieved through

different types of configurations of quadratic interactions, but all concentrating on exploiting the largest quadratic nonlinear susceptibilities so that strong cascaded quadratic nonlinearities can be produced. In all three crystals, the material Kerr nonlinearity is counterbalanced by the cascaded quadratic nonlinearity and the overall self-defocusing nonlinearity is produced, which, combined with normal dispersion, could support the CQSC.

The cascaded quadratic nonlinearity is also tunable by tuning the phase mismatch parameter, which can be achieved by: 1) in the configuration for critical interactions, tuning the angle of incident beam with respect to the optic axis to change the phase (the refractive index); 2) in ferroelectric crystals, employing QPM technology to periodically poling the optic axis and induce adjustment on the phase mismatch. It should be noted that using QPM will narrow the space for tuning the phase mismatch, as QPM induces a pre-factor on the quadratic susceptibility which reduces the upper threshold of the phase mismatch, namely decrease the cascaded nonlinearity.

The tunability of the cascading not only reflects on changing the amplitude of the SPM effects of the self-defocusing nonlinearity, but also indicates the tuning on the cascading induced self-steepening effects that gives rise to pulse shock front as well as frequency shift. Such a frequency shift regime will then add to or suppress the material intrinsic frequency regime such as the Raman induced spectral red shift.

As commonly known near-IR crystals, BBO and LN support CQSC mainly in near-IR covering the communication band. LIS is investigated as a novel mid-IR crystal, which could find CQSC for mid-IR wavelengths such as 2 μm and 3 μm. With CQSC, the generation of high intensity and few-cycle (or even single-cycle) laser pulses are always promised, and correspondingly, the pulse spectrum is extremely broadened spanning more than one octaves, namely the supercontinuum generation. With the perturbation of high order dispersion, DW generations are observed with energy converted further to longer wavelengths.

The NWEF model is proved to be generalized as all possible harmonic generations and frequency mixing processes are presented by the simulation. On the other hand, higher order harmonics other than the FW and the SH did not impact the solitary pulse formation and compression, implying that the scenario of the CQSC is quite solid in principle.

Bibliography

[1] M. Bache, H. Guo, and B. Zhou, "Generating mid-IR octave-spanning supercontinua and few-cycle pulses with solitons in phase-mismatched quadratic nonlinear crystals," Opt. Mater. Express **3**, 1647–1657 (2013).

[2] S. Ashihara, J. Nishina, T. Shimura, and K. Kuroda, "Soliton compression of femtosecond pulses in quadratic media," J. Opt. Soc. Am. B **19**, 2505–2510 (2002).

[3] J. Moses and F. W. Wise, "Soliton compression in quadratic media: high-energy few-cycle pulses with a frequency-doubling crystal," Opt. Lett. **31**, 1881–1883 (2006).

[4] M. Bache, O. Bang, and W. Krolikowski, "Limits to compression with cascaded quadratic soliton compressors," Optics Express **16**, 3273–3287 (2008).

[5] M. Bache, H. Guo, B. Zhou, X. Zeng, and X. Zeng, "The anisotropic Kerr nonlinear refractive index of the beta-barium borate ($\beta - BaB_2O_4$) nonlinear crystal," Opt. Mater. Express **3**, 357–382 (2013).

[6] D. Nikogosyan, *Nonlinear Optical Crystals: A Complete Survey* (Springer-Science, 2006).

[7] M. Bache and O. Bang, "Nonlocal explanation of stationary and nonstationary regimes in cascaded soliton pulse compression," Opt. Lett. **32**, 2490–2492 (2007).

[8] G. Valiulis, V. Jukna, and O. Jedrkiewicz, "Propagation dynamics and X-pulse formation in phase-mismatched second-harmonic generation." Phys. Rev. A **83**, 43834(14) (2011).

[9] B. Zhou, H. Guo, and M. Bache, "Soliton-induced nonlocal resonances observed through high-intensity tunable spectrally compressed second-harmonic peaks," arXiv e-print .

[10] M. Bache, O. Bang, and B. Zhou, "Optical Cherenkov radiation by cascaded nonlinear interaction: an efficient source of few-cycle energetic near- to mid-IR pulses," Opt. Express **19**, 22557–22562 (2011).

[11] J. Moses and F. W. Wise, "Controllable self-steepening of ultrashort pulses in quadratic nonlinear media," Phys. Rev. Lett. **97**, 073903(4) (2006).

[12] M. Bache and R. Schiek, "Review of measurements of kerr nonlinearities in lithium niobate: the role of the delayed raman response," arXiv e-print p. 1211.1721 (2012).

[13] M. Sheik-Bahae, D. C. Hutchings, D. J. Hagan, and E. W. Van Stryland, "Dispersion of bound electronic nonlinear refraction in solids," IEEE J. Quantum Electron. **27**, 1296–1309 (1991).

[14] B. B. Zhou, A. Chong, F. W. Wise, and M. Bache, "Ultrafast and octave-spanning optical nonlinearities from strongly phase-mismatched quadratic interactions," Phys. Rev. Lett. **109**, 043902 (2012).

[15] M. Conforti, "Exact cascading nonlinearity in quasi-phase-matched quadratic media," Opt. Lett. **39**, 2427–2430 (2014).

[16] S. Fossier, S. Salaün, J. Mangin, O. Bidault, I. Thénot, J.-J. Zondy, W. Chen, F. Rotermund, V. Petrov, P. Petrov, J. Henningsen, A. Yelisseyev, L. Isaenko, S. Lobanov, O. Balachninaite, G. Slekys, and V. Sirutkaitis, "Optical, vibrational, thermal, electrical, damage, and phase-matching properties of lithium thioindate," J. Opt. Soc. Am. B **21**, 1981–2007 (2004).

Chapter 4

CQSC in Quadratic Nonlinear Waveguides

4.1 Introduction

In this chapter, cascaded quadratic soliton compressions (CQSC) in quadratic nonlinear waveguides are studied. Quadratic (nonlinear) waveguides are well known as they not only inherit the nonlinear properties from the material, but also have optical waveguide structures that could provide guidance and confinement on the laser light beam. Basically, the waveguide is formed with the refractive index (RI) changed along a propagation channel in the material against the surrounding cladding (e.g. air or substrate materials), by means of physical or chemical methods, so that light is guided and propagated inside the channel with the principle of total-internal reflection. For the CQSC, with good confinement provided by the waveguide on the pulsed laser beam, the efficiency of nonlinear interactions will be promoted and effects of light spatial diffractions be suppressed. Therefore, laser pulses with nano-joule (nJ) energy and high repetition rate can be operated, which are complementary solutions to CQSCs in bulk materials that operate high-energy, large-beam-size pulsed lasers.

On the other hand, the dispersion engineering is possible through the design on the waveguide structure (size, profile and RI), which will give tunability of the dispersive effect of the waveguide on laser pulses. Especially, the waveguide mode is enabled to have multiple zero dispersion wavelengths (ZDWs), which could lead to novel nonlinear phenomena such as the soliton spectral tunneling (SST) effect. With a more extreme dispersion engineering, the normal dispersion range can be largely extended towards long wavelengths beyond the material ZDW and even an all-normal dispersion profile can be achieved, which could extend the CQSC into the near-infrared range (near-IR) and mid-infrared range (mid-IR), since the overall self-defocusing nonlinearity is always broadband (chapter 3) far beyond the material ZDW.

The quadratic waveguides that will be investigated in this chapter are mainly based on the lithium niobate (LN) crystal, not only because LN, as a bulk crystal, has shown great potentials in the CQSC (chapter 3), but also because LN waveguides are in fact very common devices today, except for CQSC applications. The chapter is mainly divided into two parts. First, in section 4.2, LN waveguides with small RI change are investigated, which is exactly the case in commonly used LN waveguides. The proof of concept of CQSC in such waveguides could extensively extend the applications of LN waveguides, and meanwhile, with mature fabrication technologies behind the LN waveguide, the

concept will easily be converted to reality. In the other part, section 4.3, the vision is shifted to waveguides with large RI change where the dispersion engineering will largely make effects. The GVD profile of the waveguide mode will then be flexibly tailored to 1) have multiple ZDWs with which the SST effect will be observed and discussed, and 2) show all-normal dispersion within the waveguide guidance band and extended CQSCs in mid-IR will be investigated.

4.2 LN Waveguides with Small Refractive Index (RI) Change

As one of the most commonly used quadratic waveguides, LN waveguides are usually fabricated by means of annealed proton exchange (APE) or titanium (Ti) in-diffusion, which chemically diffuses dopant into the crystal and forms slight refractive index (RI) change ($\ll 10\%$) along a strip channel where light is guided. Such waveguides have been widely used in integrated waveguide optics and optical communications for frequency conversions [1], and QPM is always employed to achieve the phase matching in nonlinear interactions. Meanwhile, they are also being studied for the cascaded response [2, 3], e.g. studying the contribution of the cascaded quadratic nonlinearity in a supercontinuum generation (SCG) [4] or a Kerr frequency comb generation [5], paving a way to the accomplishment of the CQSC. From the perspective of theoretical analyse, however, it is difficult to quantitatively characterize the waveguide modes as well as the dispersion properties of these waveguides, as the waveguide profile is quite uncertain with gradient RI change.

4.2.1 CQSC in Wafer Bonded LN Ridge Waveguides

In recent years, a novel type of LN waveguide is being developed, which is fabricated by means of the *wafer bonding* [6]. For example, with surface ion implantation, a LN wafer is directly bonded on a lithium tantalate (LT) substrate and the whole structure is subsequently diced to form a ridge waveguide profile, see Fig. 4.1. Compared to APE or Ti in-diffused waveguides, LN/LT waveguides have a clear profile with step RI change so that they can be accurately analysed.

This section presents that, with the quadratic susceptibility inherited from the material, the LN/LT ridge waveguide could also produce a strong cas-

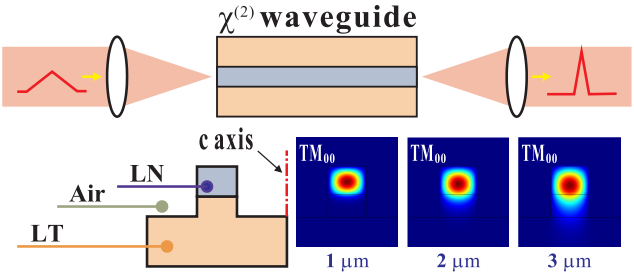

Fig. 4.1: Diagram of cascaded quadratic soliton compression in a LN ridge waveguide; fundamental mode (TM_{00}) distributions at different wavelengths (1, 2 and 3 μm) are also shown, with structure marked as S-1; c axis is the optic axis of the crystal, i.e. the crystallographic z-axis.

caded quadratic nonlinearity through a noncritical phase mismatched second harmonic generation (SHG) process, with which the material Kerr nonlinearity could be counterbalanced and an overall self-defocusing nonlinearity is produced. Meanwhile, with the small RI change in the waveguide, the dispersion properties are kept close to the material as well. Therefore, the CQSC is accomplishable in the LN/LT waveguide just as it works in the bulk LN. Moreover, QPM is no longer necessary as the phase mismatch inherently lies between the two thresholds of the CQSC, which supports a dominant and non-resonant cascaded nonlinearity.

First, the eigen-modes of the waveguide are calculated, including both mode distributions B_j and propagation constants β_j, by using the software *COMSOL Multiphysics*. Examples of fundamental TM_{00} mode distributions at different wavelengths are shown in Fig. 4.1. In Fig. 4.2(a) we show effective RIs of extraordinary eigenmodes (with the electric field polarized along the crystallographic z-axis). As guided modes, they should have the effective RI lying between the substrate RI and the core RI. Since the LN core and the LT substrate have small RI change, the confinement of the waveguide is quite weak and the eigen-modes are restricted to a narrow strip of the effective RIs, which results in two consequences: 1) the mode effective RIs and mode cutoff wavelengths will become sensitive to the waveguide (core) size; 2) the effective RI profiles (especially for the fundamental TM_{00} mode) as well as the dispersion properties remain close to the material profile as there is little room for variation.

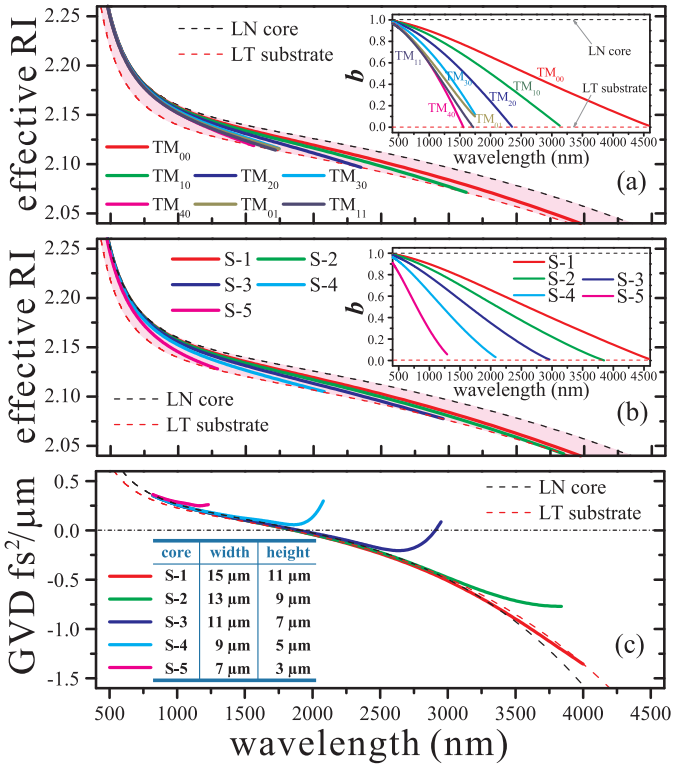

Fig. 4.2: Dispersion properties of the LN ridge waveguide; (a) effective RIs of eigen-modes, in the waveguide structure S-1; (b) fundamental mode effective RIs of different waveguide structures; inserts in (a, b) show normalized effective RIs in which the material dispersion is removed; (c) GVD profiles of the fundamental mode in different waveguide structures; detailed waveguide sizes are shown as insert.

A normalized propagation constant is defined to help remove the material dispersion and to better illustrate the eigenmodes in the waveguide [7]:

$$b = (n_{\text{eff}}^2 - n_{\text{sub}}^2)/(n_{\text{core}}^2 - n_{\text{sub}}^2) \tag{4.1}$$

where n_{eff}, n_{core} and n_{sub} are the mode effective RI, the LN core RI and the LT substrate RI, respectively. Figure Fig. 4.2(b) shows that with a decreasing core size the fundamental mode is strongly impacted and its cutoff wavelength is shortened as the waveguide confinement is further reduced. Meanwhile, the

GVD ($\beta^{(2)} = d^2\beta/d\omega^2$) profiles tend to follow the material profile except for a deflection around the cutoff wavelength, see Fig. 4.2(c), as there the effective RI is approaching and turning into the substrate RI and a large waveguide dispersion is produced. For structures S-1, S-2 and S-3, the fundamental mode will have both normal and anomalous GVD regions, transiting at a single zero dispersion wavelength (ZDW) which is close to the material ZDW around 1900 nm. Fundamental modes in structures S-4 and S-5 have very short cutoff wavelengths so that they just have normal GVD regions.

We estimate the nonlinearities in the waveguide. The cascaded quadratic nonlinearity is represented as the nonlinear coefficient [8]:

$$\gamma_{\text{casc}} = \frac{\omega}{c}\frac{n_{2,\text{casc}}}{A_{\text{eff,SHG}}} \tag{4.2}$$

which is analogous to the material Kerr nonlinearity scaled as [14]:

$$\gamma_{\text{Kerr}} = \frac{\omega}{c}\frac{n_{2,\text{Kerr}}}{A_{\text{eff,SPM}}} \tag{4.3}$$

where $A_{\text{eff,SHG}}$ and $A_{\text{eff,SPM}}$ are effective mode areas corresponding to the cascaded nonlinearity and the Kerr nonlinearity, respectively. It should be noted that $A_{\text{eff,SHG}}$ actually stems from the (cascaded phase mismatched) second harmonic generation (SHG) process and therefore has a different definition to the commonly known $A_{\text{eff,SPM}}$ from a Kerr self-phase modulation (SPM) process. A dispersive $A_{\text{eff,SHG}}$ referring to the SHG within the TM_{00} mode is defined as [8]:

$$A_{\text{eff,SHG}}(\omega_1) = \frac{(\iint dxdy|\tilde{B}_{\text{TM}_{00}}(\omega_2)|^2)(\iint dxdy|\tilde{B}_{\text{TM}_{00}}(\omega_1)|^2)^2}{(\iint dxdy\tilde{B}^*_{\text{TM}_{00}}(\omega_2)\tilde{B}^2_{\text{TM}_{00}}(\omega_1))^2} \tag{4.4}$$

where $\tilde{B}_{\text{TM}_{00}}$ is the eigen-mode distribution of the TM_{00} mode, ω_1 and ω_2 are angular frequencies of the fundamental wave (FW) and the second harmonic (SH). $A_{\text{eff,SHG}}$ as a function of the pump wavelength is illustrated in Fig. 4.3(a), which is quite close to the $A_{\text{eff,SPM}}$ referring to the Kerr SPM process within the TM_{00} mode. Other effective mode areas stemming from interactions among high-order modes (also phase mismatched) are much larger than the two shown due to the orthogonality among different modes, and the corresponding nonlinear factors γ are therefore largely reduced and negligible.

Compared to the definitions of nonlinear modal susceptibilities in chapter 2 (Eq.(2.41) and Eq.(2.45)), effective mode areas calculated here are actually

the contributions of mode overlap to the susceptibilities while the material susceptibilities are abstracted out of the integral as they are considered constant, i.e.:

$$\begin{aligned}\bar{\Theta}^{(2)}_{\mathrm{j};\alpha_1\alpha_2} &= \bar{\chi}^{(2)}\theta^{(2)}_{\mathrm{j};\alpha_1\alpha_2} \\ \bar{\Theta}^{(3)}_{\mathrm{j};\alpha_1\alpha_2\alpha_3} &= \bar{\chi}^{(3)}\theta^{(3)}_{\mathrm{j};\alpha_1\alpha_2\alpha_3}\end{aligned} \tag{4.5}$$

where:

$$\begin{aligned}&\theta^{(2)}_{\mathrm{j};\alpha_1\alpha_2}(\omega_1+\omega_2) \\ &\qquad = \iint_{\mathrm{core}} dxdy\tilde{B}^*_{\mathrm{j}}(x,y,\omega_1+\omega_2)\tilde{B}_{\alpha_1}(x,y,\omega_1)\tilde{B}_{\alpha_2}(x,y,\omega_2)\end{aligned} \tag{4.6}$$

$$\begin{aligned}&\theta^{(3)}_{\mathrm{j};\alpha_1\alpha_2\alpha_3}(\omega_1+\omega_2+\omega_3) \\ &= \iint_{\mathrm{core}} dxdy\tilde{B}^*_{\mathrm{j}}(x,y,\sum\nolimits_{\mathrm{n}}\omega_n)\tilde{B}_{\alpha_1}(x,y,\omega_1)\tilde{B}_{\alpha_2}(x,y,\omega_2)\tilde{B}_{\alpha_3}(x,y,\omega_3)\end{aligned} \tag{4.7}$$

and,

$$\begin{aligned}A_{\mathrm{eff,SHG}} &= \left(\theta^{(2)}_{\mathrm{TM_{00};TM_{00},TM_{00}}}\right)^{-2} \\ A_{\mathrm{eff,SPM}} &= \left(\theta^{(3)}_{\mathrm{TM_{00};TM_{00},TM_{00},TM_{00}}}\right)^{-1}\end{aligned} \tag{4.8}$$

Figure Fig. 4.3(b) shows that the negative nonlinear cascading factor γ_{casc} for the TM_{00} mode is stronger than the Kerr nonlinear factor γ_{Kerr} over a broad wavelength span (1100 - 3000 nm). Such a broadband self-defocusing nonlinearity is actually built up due to the large susceptibility d_{33} of the LN material which gives rise to a dominant $n_{2,\mathrm{casc}}$. However, recall that such a self-defocusing nonlinearity should work with the normal dispersion to create solitary waves, so the window of operation is actually from 1100 nm to the ZDW at 1900 nm. Within such a a "compression window" [10] the phase-mismatch parameter is actually below the critical value Δk_{c} referring the balance between the cascaded and the Kerr nonlinearity, see Fig. 4.3(c). Meanwhile, the phase mismatch stands above the lower threshold Δk_{th} in the non-resonant area, which means the cascaded response is broadband and fast decayed to support few-cycle pulse generations with clean profiles.

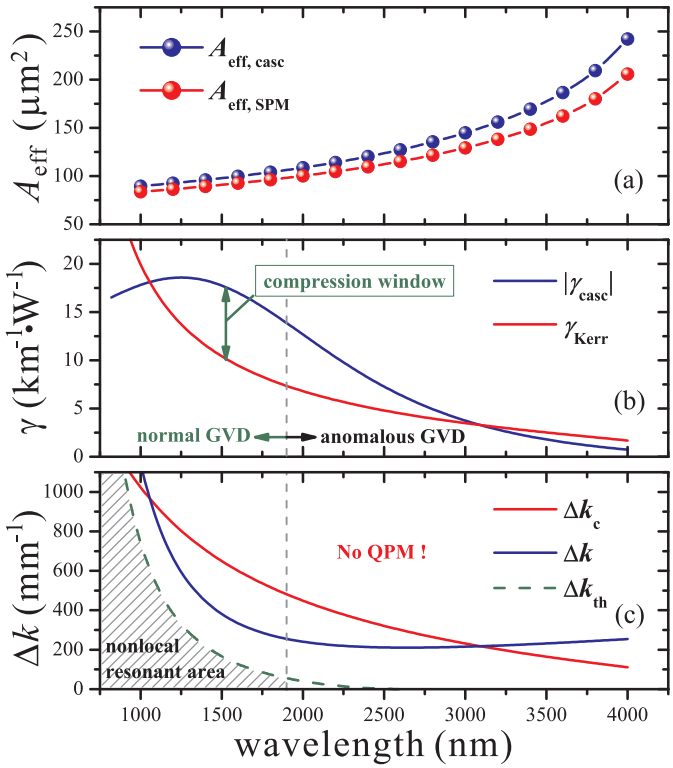

Fig. 4.3: Nonlinearities in the LN ridge waveguide with structure S-1; (a) effective mode area corresponding to the cascaded SHG process and Kerr SPM process in the fundamental mode TM_{00} ; (b) the nonlinear factor of the cascaded quadratic nonlinearity as well as the Kerr nonlinearity, a compression window is shown from 1100 nm to 1900 nm in which a dominant self-defocusing nonlinearity is achieved; (c) equivalently, the phase mismatch is below the critical value Δk_c marking the onset of a self-focusing nonlinearity, and it is non-resonant as it stays above the nonlocal resonant area (marked area).

It is impressive that, unlike most LN waveguides using QPM to make the phase matching, the presented LN ridge waveguide provides the phase mismatch which inherently lies between the two thresholds just like the case in the bulk LN. Therefore, the CQSC is naturally supported.

Summarizing, the overall nonlinearity is $\gamma_{\text{eff}} = \gamma_{\text{casc}} + \gamma_{\text{Kerr}}$. The nonlinear length of the waveguide is then calculated as $L_{\text{N}} = |P_{\text{in}} \cdot \gamma_{\text{eff}}|^{-1}$, where P_{in} is

the peak power of the pump laser pulse. Furthermore, with the dispersion length $L_{\mathrm{D}} = T_{\mathrm{in}}^2/|\beta^{(2)}|$ (T_{in} indicates the pulse duration), the soliton number N_{eff} can be finally estimated as $N_{\mathrm{eff}}^2 = L_{\mathrm{D}}/L_{\mathrm{N}}$.

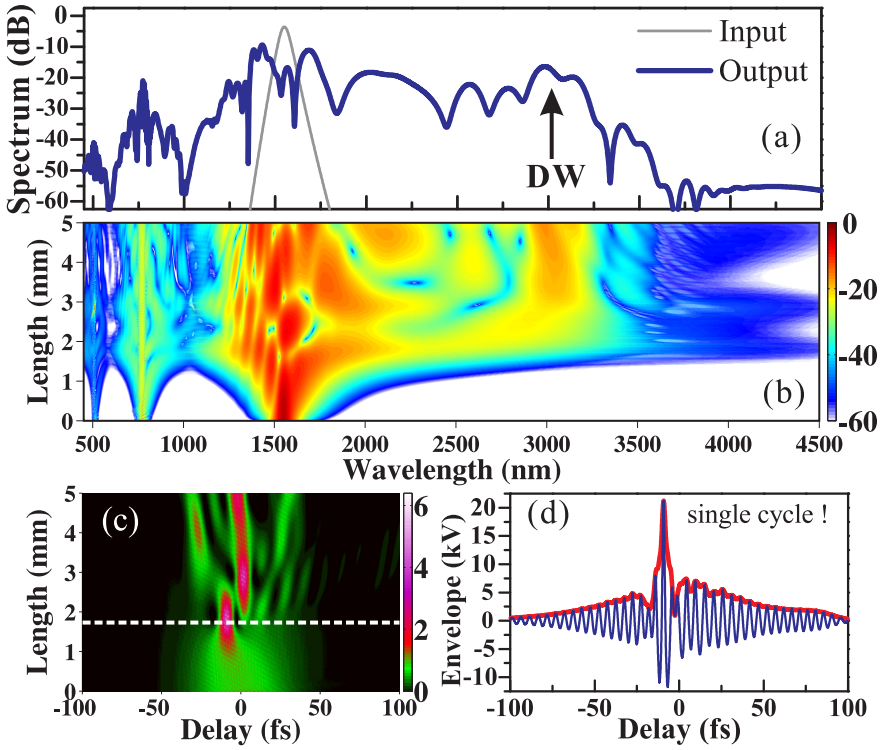

Fig. 4.4: Numerical simulation of the CQSC in the LN ridge waveguide with structure S-1, pumped at 1550 nm; the pump pulse has a FWHM of 50 fs, $P = 200$ kW giving a pulse energy of 10 nJ; $\gamma_{\mathrm{casc}} = -17.6\ \mathrm{km^{-1}W^{-1}}$ and $\gamma_{\mathrm{Kerr}} = 9.9\ \mathrm{km^{-1}W^{-1}}$, giving $N_{eff} \approx 3.7$; (a) pulse spectrum at the input and the output; (b) pulse spectral evolution (in dB scale); (c) pulse temporal evolution with the self-compression position marked by the white dashed line (scaled to the peak power of the input pulse); (d) physical real-valued electric field amplitude of the self-compressed pulse.

Then, the CQSC in the LN ridge waveguide is numerically modeled by the NWEF. As is discussed in chapter 2, in waveguides, the NWEF is actually governing the propagation dynamics of the pulse electric field amplitude while

the pulse transverse distribution is described in form of waveguide eigenmode distributions. Figure 4.4 shows the CQSC at 1550 nm where the total self-defocusing nonlinearity γ_{eff} is maximum. The pump laser pulse has 10-nJ energy, 50-fs full width at half maximum (FWHM) and it is coupled into the TM_{00} mode. During the propagation, the pulse spectrum evolves with SPM-induced spectral broadening. Meanwhile, a soliton-induced dispersive wave (DW) is generated in the opposite GVD range at around 3000 nm due to the perturbation of higher-order dispersion, see Fig. 4.4(a,b). Combined with the normal dispersion, the ultra-broad spectrum leads to the formation of a single-cycle self-compressed solitary pulse. In Fig. 4.4(c), the pulse profile is significantly compressed while its peak power is enhanced over 6 times. After the compression, the pulse is split into several branches due to the Raman fission effects. Fig. 4.4(d) shows the electric field amplitude of the the compressed pulse, with clean and single-cycle profile. Actually, at other wavelengths and in the other structures, S2 to S5, the scenario of the CQSC also works only if the pump pulsed laser is within the compression window as illustrated above.

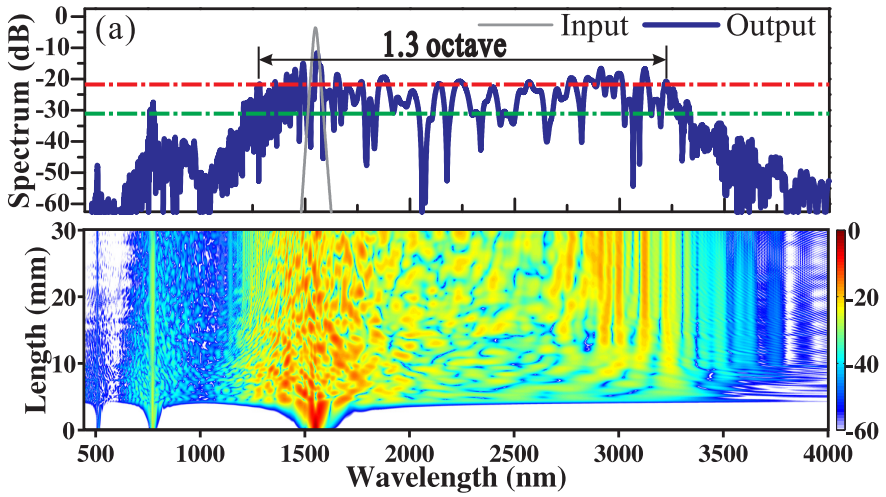

Fig. 4.5: Supercontinuum generation in the waveguide S-1 pumped at 1550 nm; the pump pulse has 30-nJ energy, 150-fs FWHM; the soliton order is $N = 11.1$; (a) pulse supercontinuum spectrum at the input and the output (the red dashed line marks the -10 dB range of the output spectrum, the green dashed line marks the -20 dB range); (b) pulse spectral evolution.

Aside from the pulse compression, such a waveguide can also be applied for the SCG. By launching a longer pulse with more energy, namely 150-fs FWHM and 30-nJ energy, the soliton number is increased correspondingly to 11.10 and a supercontinuum spectrum covering 1300 $\sim$ 3200 nm with 1.3 octave bandwidth (at -10 dB) is accomplished, as shown in Fig. 4.5. As opposed to SCG in photonic crystal fibers [11], here the combination of self-defocusing nonlinearities and solitary pulse formation in the normal dispersion regime leads to the blue edge of the spectrum being supported by the cascading induced pulse self-steepening, while the red-edge formation occurs due to the Raman induced pulse splitting in the nonlinear regime, and soliton-induced DW generation in the linear long-wavelength regime in the anomalous dispersion range.

Beyond above investigations regarding the LN/LT waveguide, a general concept is concluded as: CQSC can be fully transplanted from the bulk LN to a LN waveguide when the waveguide has small RI change that both the dispersion and cascaded quadratic nonlinearity are kept similar to the material: the ZDW is quite close and the operational wavelength range of the CQSC is similar. The difference is that the pulse energy of the pump laser is much reduced thanks to the tight confinement or small effective mode areas provided by the waveguide.

Therefore, with small RI changes, CQSCs in common APE or Ti in-diffused LN waveguides can also be accomplished.

4.2.2 Experiments of CQSC in APE LN Waveguides

In this section, the experimental investigation of CQSC in QPM-free APE LN waveguides is presented. Pulse spectral broadening induced by the SPM of the self-defocusing nonlinearity is observed and the octave-spanning supercontinuum generation at communication band is accomplished. Detailed pulse spectral evolutions are also studied, which reveals the physics of the cascading-induced self-defocusing regime.

The waveguide chip in following experiments is provided by the Institute of Applied Optics, Friedrich Schiller University Jena, as a corporation. Waveguides are fabricated by APE on the surface of a congruent LN (CLN) they are all z-cut for type-0 interactions. The waveguide buried core has a depth of 4.1 μm and 4 types of width, i.e. 6 μm, 7 μm, 8 μm and 9 μm. The RI change in such a waveguide is as small as $\Delta n = 0.03$, at 1550 nm. Therefore, the waveguide inherits strong and self-defocusing cascaded nonlinearity from the

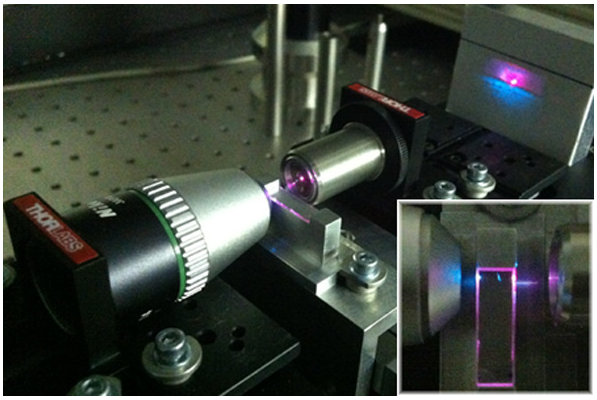

Fig. 4.6: Experiment set up with laser pulses spatially coupled in and out the APE LN waveguide through lenses.

LN material. The small RI change also implies that the waveguide is almost single-mode in near-infrared. The length of the waveguide is $L = 5$ mm.

The experiment set up is shown in Fig. 4.6. The pump pulse is generated from a commercial Ti:sapphire regenerative amplifier and a travelling wave optical parametric amplifier (TOPAs). The pulse has full width at half maximum $\tau_{\mathrm{FWHM}} = 50$ fs and the wavelength is tunable from 1250 nm to 1650 nm. The pulse repetition rate f_{rep} is 1 kHz. The pump beam is spatially coupled into the waveguide by using an objective lens (*Nikon* $\times 20/0.5$) and the output beam is collected by using an aspheric lens (*Thorlab*, $f = 8.0$ mm, $NA = 0.5$). We measure that the coupling loss is around 10 dB, which partially arises from the interface reflection on lenses as well as on waveguide ends, and from the beam profile mismatch between the input beam and the waveguide eigen mode distribution (i.e. the fundamental $\mathrm{TM}_0 0$ mode). The output pulse spectrum is measured by a spectrometer (*OceanOptics*, NIRQuest512-2.5). Pump power and the output power are detected by a power meter so that they are average power P_{avg} values. The pulse peak power P_{peak} is estimated as $P_{\mathrm{peak}} = P_{\mathrm{avg}}/(\tau_{\mathrm{FWHM}} \cdot f_{\mathrm{rep}})$ and therefore the pulse energy is $E = P_{\mathrm{peak}} \cdot \tau_{\mathrm{FWHM}}$.

Figure 4.7 shows the robust supercontinuum generations with pump sources at different wavelengths. Tuned from 1250 nm to 1500 nm, each pump could evoke a supercontinuum. These spectra are all detected when the output power has $P_{\mathrm{avg,out}} \approx 10$ μW, corresponding to a pulse energy of 10 nJ. The spectral broadening could easily exceed 600 nm, when taking the 20-dB measurement,

and at 30-dB level, the bandwidth is more than one octave from $1 \sim 2$ μm. Remember that the waveguide is as compact as 5-mm long, such a spectral broadening is of much higher efficiency compared to a highly nonlinear optical fiber.

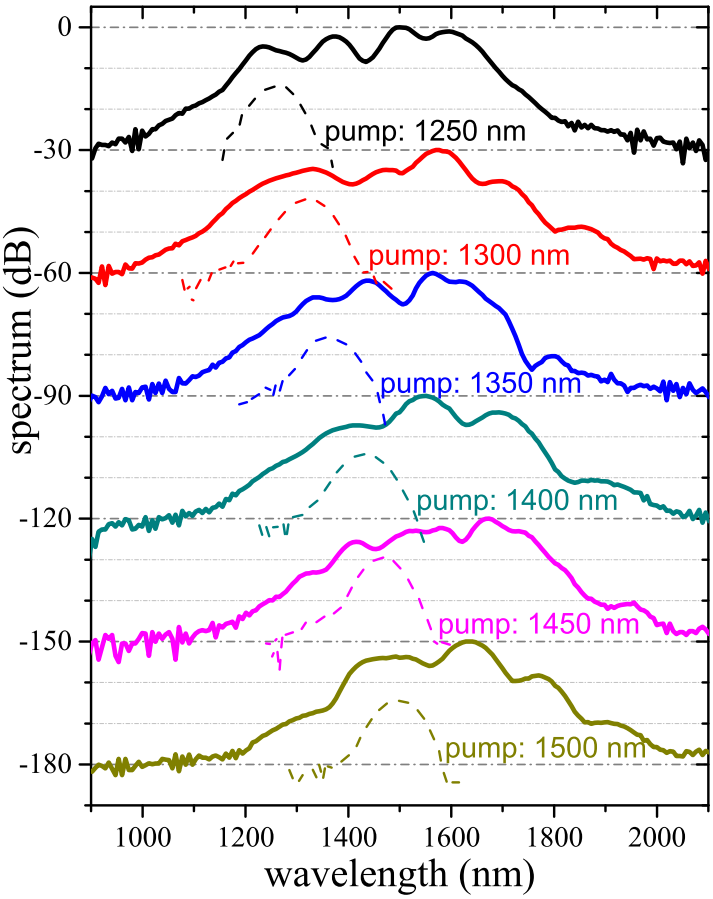

Fig. 4.7: Supercontinuum generations with pump at different wavelengths. All supercontinuum spectra are detected with the output power $P_{\text{avg,out}} \approx 10$ μW. The waveguide core width is 9 μm. Each energy spectrum data is normalized to the peak value and a 30-dB offset is inserted between two spectra in the stack.

On the other hand, It is noticed that all the spectral broadening here shows

asymmetry with respect to the pump wavelength and the spectrum is always significantly extended at the red side towards long wavelengths. This is because the LN has a large fraction $f_R > 50\%$ [12] of vibrational Raman response in the material cubic nonlinearity that gives rise to pulse spectral red shifting during the propagation [13].

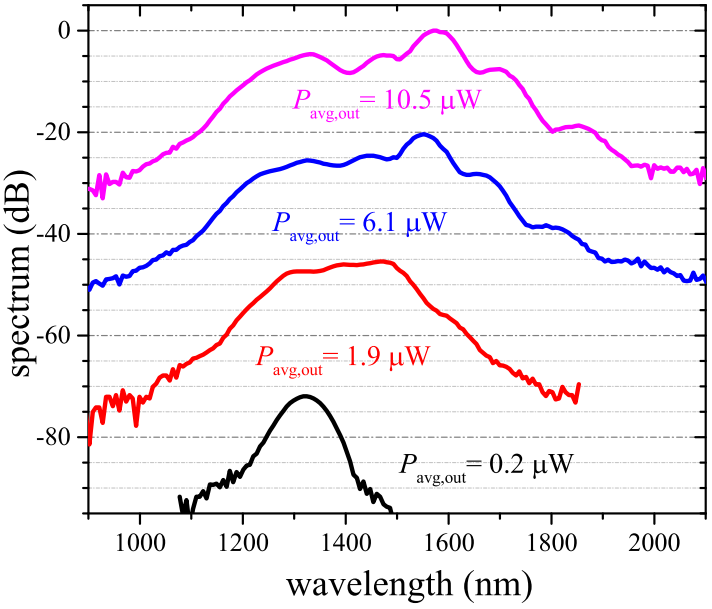

Fig. 4.8: Pulse spectral broadening with an increase of the incident pump power. The pump is at 1300 nm, the waveguide core width is 9 μm. All 4 spectra are normalized to the peak value of the most powerful spectrum (i.e. the pink one with $P_{\text{avg,out}} = 10.5$ μW) and between two spectra there is a 20-dB offset

The pulse spectral broadening is understood as the result of the SPM effects, in which the bandwidth is formulated as [14]:

$$\Delta\omega \propto \frac{\gamma_{\text{eff}} P_{\text{peak}} L}{\tau_{\text{FWHM}}} \tag{4.9}$$

where $\gamma_{\text{eff}} = \gamma_{\text{casc}} + \gamma_{\text{Kerr}}$ is the effective nonlinear fractor in the waveguide that comes from the competing between the cascaded self-defocusing nonlinearity $\gamma_{\text{casc}} \propto -\frac{d_{\text{eff}}^2}{\Delta k \cdot A_{\text{eff,SHG}}}$ and material intrinsic Kerr nonlinearity $\gamma_{\text{Kerr}} \propto \frac{c_{33}}{A_{\text{eff,SPM}}}$, see Chapter 4.2.1. The expression actually contains a premise that the pulse

profile does't change much during the spectral broadening, namely the pulse dispersion length L_{D} and the nonlinear length $L_{\mathrm{N}} = (\gamma_{\mathrm{eff}} P_{\mathrm{peak}})^{-1}$ have the relationship: $L_{\mathrm{D}} \gg L_{\mathrm{N}} > L$. d_{eff} and c_{33} are the quadratic and cubic nonlinear susceptibilities. Δk is the SHG phase mismatch parameter. $A_{\mathrm{eff,SHG}}$ and $A_{\mathrm{eff,SPM}}$ are effective mode areas corresponding to quadratic SHG and cubic SPM processes, and usually have $A_{\mathrm{eff,SHG}} \approx A_{\mathrm{eff,SPM}}$.

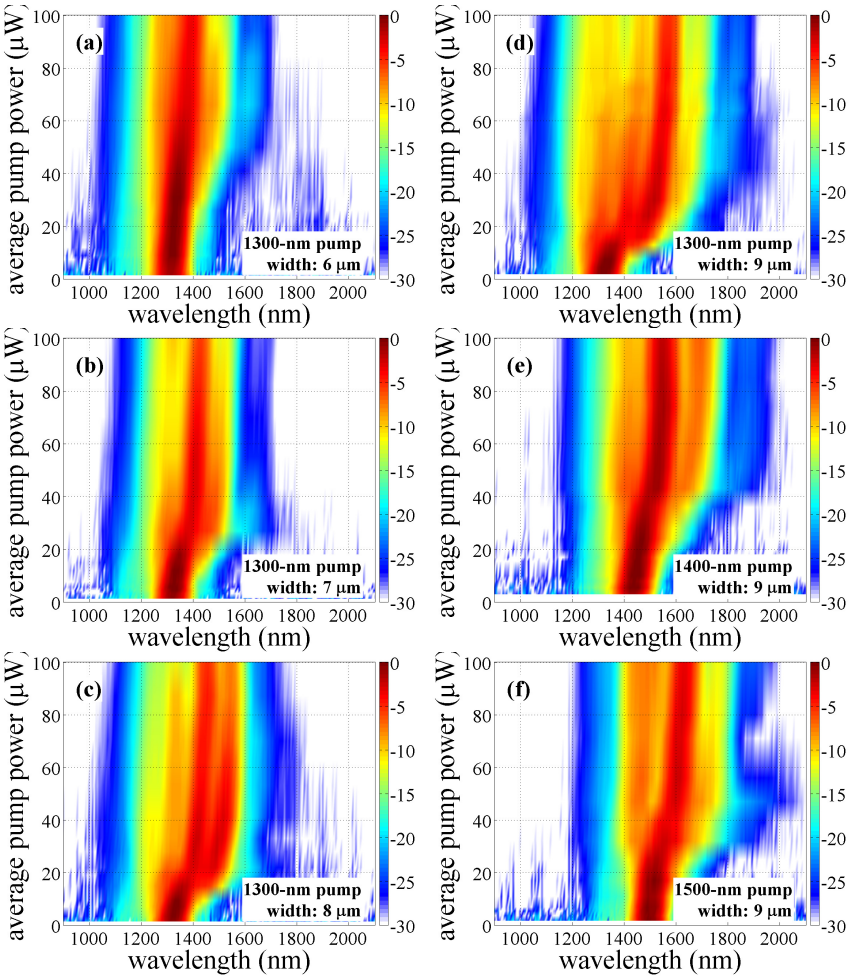

Fig. 4.9: pulse spectral evolution with respect to the average pump power, in waveguides with different core width and with different pump wavelengths.

Therefore, with an increase of the power, the spectrum bandwidth is expected to increase as well. Figure 4.8 demonstrates such a trend, but quantitatively, the bandwidth is not in proportional to the power. One main reason is that when the power is increased, the nonlinearity length will be shortened and have $L_{\mathrm{N}} < L$, which means the pulse profile has been significantly changed. Especially, when the self-defocusing nonlinearity meets the normal GVD, the pump pulse will propagate in solitons and temporally have soliton self-compressions. Besides, other reasons include that: 1) γ_{eff} has a spectral intensity distribution rather than being a constant, which means such spectral broadening efficiency really varies at different wavelengths; and 2) pulse will experience Raman-induced spectral shifting. All these factors will impact the pulse spectral broadening as well as the supercontinuum generation.

Detailed pulse spectral evolutions with respect to the pump power in different waveguides are shown in Fig. 4.9. It is noted that with a decrease of the waveguide core width, the pulse spectral broadening is degraded, which implies a reduction on the parameter γ_{eff}. Intuitively, the decrease on the core size will result in smaller $A_{\mathrm{eff,SHG}}$ and $A_{\mathrm{eff,SPM}}$ and therefore should have increased the nonlinear factor. But the truth is, the SHG phase mismatch parameter Δk is also increased (the phase mismatch parameter $\Delta\beta = \beta_2 - 2\beta_1$, where the propagation constant of the FW β_1 is increased more than that of the SH β_2 [7]), which decreases the cascaded nonlinearity γ_{casc} and therefore decreases the overall nonlinearity. On the other hand, when the waveguide is pumped at a longer wavelength, the spectral broadening is weakened because areas $A_{\mathrm{eff,SHG}}$ and $A_{\mathrm{eff,SPM}}$ are much increased when getting close to the cutoff boundary.

Numerical simulations are also studied regarding such APE waveguides. To simplify the model, the waveguide core is considered to have a rectangular shape with step index change to the CLN substrate. Then, we follow the steps as shown in chapter 4.2.1 to: 1) calculate the waveguide eigen-modes, including the mode effective RIs and the mode distribution; 2) estimate both cascaded and Kerr nonlinearities in the waveguide, including the calculation of effective mode areas $A_{\mathrm{eff,SHG}}$ and $A_{\mathrm{eff,SPM}}$; and 3) investigate the pulse propagation dynamics and ultra-fast nonlinear interactions by solving the generalized NWEF.

Figure 4.10 shows the simulation of the supercontinuum generation with a 1300-nm pump. The pulse energy is $P_{\mathrm{avg}} = 6\ \mu$W. It is relevant to mention that the waveguide mode has normal GVD in the guidance band until 2 μm. The simulation shows good agreement to the experiment on the output su-

percontinuum. Moreover, pulse temporal evolution is estimated as well, which reflects the soliton pulse propagation and the soliton self-compression effects. With material Raman response, soliton fission effects [15] is also observed. In our experiments right now, such temporal profiles can hardly be characterized by self-referenced detections e.g. an auto-correlator as the average output power is too low. Strong referenced detection as what is described in [16] may be a solution to the problem and we will figure it out in the future.

On the other hand, the pump pulse duration is also sensitive as the waveguide is as short as 5 mm. When launching longer pulses, e.g. on 100-fs-level, the waveguide chip should be much longer due to the increase of the dispersion length, which actually implies that a fiber laser, with mega-Hz repetition rate but 100-fs pulse duration, is not suitable for such a short waveguide.

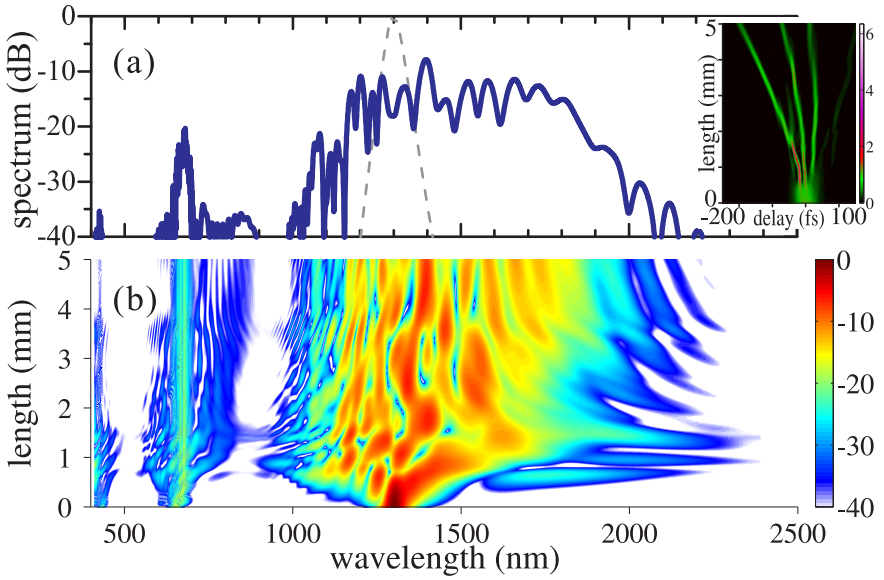

Fig. 4.10: Numerical simulation of supercontinuum generation at 1300 nm, the pump pulse has $\tau_{\mathrm{FWHM}} = 50$ fs, $P_{\mathrm{avg}} = 6\ \mu$W, $E = 6$ nJ, $L_{\mathrm{D}}(\lambda = 1300nm) = 4.63$ mm, $L_{\mathrm{N}} = 0.97$ mm, $\gamma_{\mathrm{casc}} = -47.4\ (\mathrm{km} \cdot \mathrm{W})^{-1}$, $\gamma_{\mathrm{Kerr}} = 38.8\ (\mathrm{km} \cdot \mathrm{W})^{-1}$. $f_{\mathrm{R}} = 55\%$, material dispersion of the substrate CLN is also taken into consideration; (a) supercontinuum generation at the output; (b) pulse spectral evolution during the propagation; inset in (a) pulse temporal evolution during the propagation.

4.3 Wafer Bonded LN Ridges Waveguides with Large RI Change

As a physical method, wafer bonding is robust. Besides bonding materials of similar properties, e.g. the LN/LT wafer bonding, recent investigations have emerged on the bonding among different classes of materials, especially bonding crystals with glasses, making e.g. LN/silica waveguides [17], chalcogenide/sapphire waveguides [18], etc., which actually opens the access to varieties of materials in the fabrication of quadratic nonlinear waveguides.

Here we investigate a LN/glass waveguide with similar ridge profile and step RI change to the LN/LT waveguide, but using a substrate material with a substantially lower RI than LN. With this design, 1) the waveguide guidance band is extensively extended towards long wavelengths entering the mid-IR, even with a tiny core size making the sub-wavelength waveguide; 2) the dispersion engineering is enabled, with which an all-normal dispersion profile of a waveguide mode can be achieved, as a result of the strong waveguide dispersion produced under the large RI change. Then, the full bandwidth of the cascading dominated self-defocusing nonlinearity can be used for the CQSC, despite the material ZDW which usually sets a limitation on the operational wavelength range in a bulk LN or in a LN waveguide with small RI change. Meanwhile, the pulse compression dynamics under the all-normal dispersion is purely nonlinear, which means linear interactions such as dispersive wave (DW) generations are not occurring, which otherwise are always accompanied with soliton formation. The waveguide with large RI change also allows for much tighter confinement compared to previous studies, implying that pump pulsed lasers with sub-nJ energy can lead to few-cycle solitary pulse formation. On the other hand, the waveguide does require imposing a moderate QPM pitch to overcome the competing self-focusing Kerr nonlinearity, in contrast to the LN/LT waveguide design.

In the following of this section, we investigate the mode profiles and dispersion landscape of such an LN waveguide design with a large RI change. We then numerically investigate the self-defocusing soliton formation in the near- and mid-IR beyond the material ZDW, under the waveguide-induced all-normal dispersion and the cascading dominated self-defocusing nonlinearity. We also investigate a design where a small anomalous dispersion region is sandwiched between two normal dispersion regions, and show few-cycle DW formation in

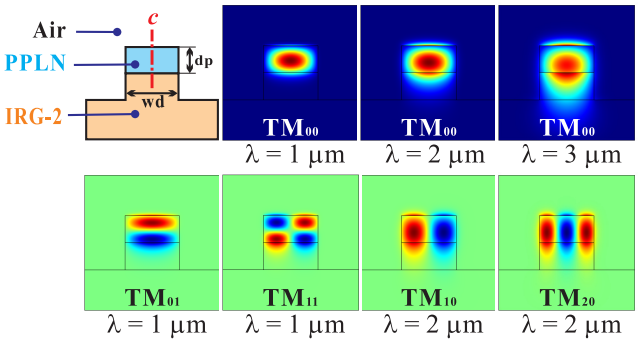

Fig. 4.11: waveguide structure and mode field distributions of eigen-modes, at different wavelengths; waveguide has wd = 4 μm, dp = 2 μm.

the mid-IR seeded by a near-IR soliton.

The waveguide structure is shown in Fig. 4.11. There are varieties of candidates for the substrate material which ought to have a much lower RI than LN and good transparency in the near- and mid-IR, e.g. the potassium titanyl phosphate (KTP), the rubidium titanyl phosphate (RTP), the lithium iodate (LI), etc. in the group of crystals, or the fused silica, the fused germania, the ZBLAN, etc. in the group of glasses [19]. Here, a glass with broadband infrared transmission, specifically the Schott IRG-2 germanate glass (transparency range $0.36 \sim 4.6\mu$m), is chosen as the waveguide substrate, see [19] for material details. The LN core layer is assumed to be bonded on the substrate and then the whole structure can be diced to have a standard ridge profile. The RI change in such a waveguide is as large as $\Delta n \approx 0.3$. Aiming at mid-IR pulse operations and making use of the strong waveguide dispersion, the waveguide size is designed to be around sub-wavelength. Eigenmodes, including both the mode propagation constants and transverse distributions, are calculated by using *Comsol Multiphiscs*. Extraordinary modes (with the polarization direction along the optic c-axis, marked as TM modes) at different wavelengths are shown in Fig. 4.11, while mode effective RIs are shown in Fig. 4.12(a). The guidance cutoff wavelength of such a waveguide can be easily extended to the mid-IR due the large RI change. Since the mode RIs are going down from the core RI to the substrate RI towards longer wavelengths, the large RI change implies a large SHG phase mismatch parameter, explaining why QPM is needed to ensure the strong cascading. Basically, waveguide dispersion al-

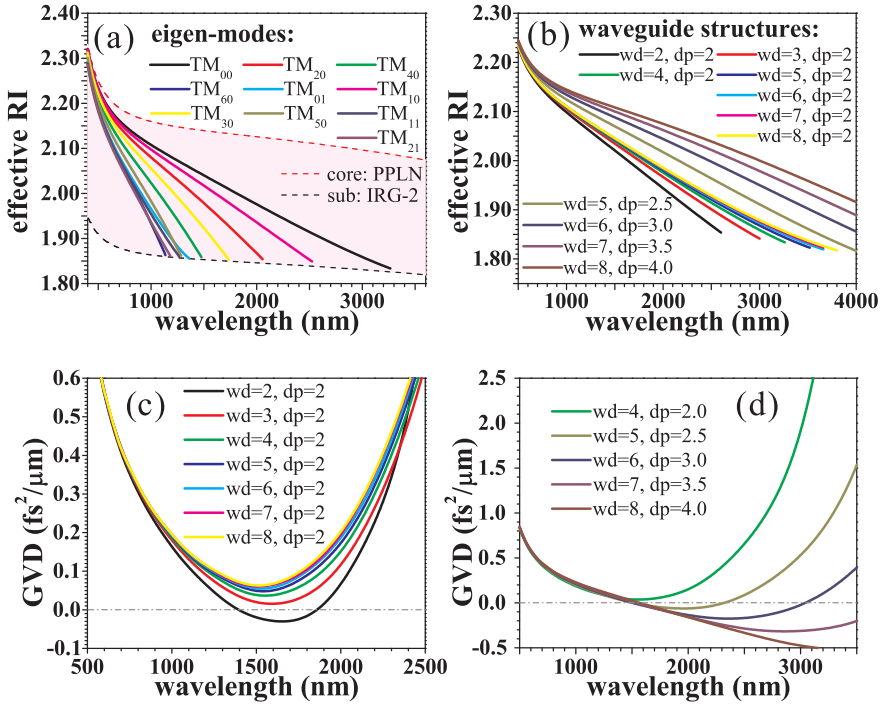

Fig. 4.12: waveguide eigen-modes and dispersion tailored by tuning the core size; (a) mode effective RIs in the waveguide with wd = 4 μm, dp = 2 μm; (b) variation of TM_{00} mode effective RI profiles under different core sizes and (c, d) variation of GVD profiles with different core sizes.

ways has an opposite trend to the material one, and with strong waveguide dispersion, the waveguide mode shows a typical "U"-shape GVD trend and is enabled to have normal dispersion at long wavelengths. Similar trends can also be found in step-indexed photonic crystals fibers (PCFs), which also have a large RI change [20]. Moreover, by tuning the core size (width and depth), the mode effective RI will be shifted (Fig. 4.12(b)) and the mode GVD profile is consequently tailored. When tuning the core width but fixing the height, the mode GVD profile is tuned mainly in the amplitude (see Fig. 4.12(c)) while the "U"-shape is almost preserved, with the bottom fixed at around 1.58 μm which is co-determined by the material GVD of both the core and the substrate. When enlarging the core size and keeping the aspect ratio, the GVD profile is tuned in both the amplitude and the trend (see Fig. 4.12(d)) as the

waveguide confinement is further enhanced and the waveguide-induced normal dispersion is shifted towards longer wavelengths. It is also noticed that, to some extent, an all-normal dispersion profile can be achieved while the cutoff wavelength remains over 3 μm.

On the other hand, the transmission loss is always concerned when taking about a waveguide. Generally, the transmission loss mainly includes: 1) the insertion loss when light is coupled into and out from the waveguide (e.g. light reflection on interfaces, the mode field mismatch, etc.); 2) the material loss; and 3) the waveguide loss due to the uncertainty of the structure (e.g. the core is non-uniform along the propagation axis). Besides the material and waveguide losses, the common feeling that a small dimension waveguide is "lossy" is mainly due to the intolerable insertion loss. With a sub-wavelength structure, the waveguide eigenmodes, no matter the fundamental mode or high-order modes, turn to have strong evanescent waves and therefore the mode transverse distribution is seriously mismatched to a normal incident laser beam that has a Gaussian distribution. But the insertion loss only occurs at the frontend of the waveguide and will not impact the whole pulse propagation dynamics. In the following text, the value of the pump pulse energy or the pulse peak power that we will mention actually refers to the effective pulse energy that is launched into the waveguide, with the insertion loss already been eliminated. The material loss can be ignored due to the good transparency of the material within the guidance band. Also, the waveguide loss is ignorable as the wafer bonding and the dicing technologies are supposed to give high certainty of the structure.

As for the nonlinearity, the mode overlap integrals $\bar{\Theta}^{(2)}_{\mathrm{j;TM_{00}TM_{00}}}(2\omega)$ and $\bar{\Theta}^{(3)}_{\mathrm{TM_{00};TM_{00}}\alpha_2\alpha_2}(\omega)$ are calculated in Fig. 4.13(a,b), which correspond to the SHG process and the Kerr SPM or cross-phase modulation (XPM) effects, respectively. The material susceptibilities involved are $\bar{\chi}^{(2)}_{\mathrm{e;ee}}$ and $\bar{\chi}^{(3)}_{\mathrm{e;eee}}$.

It is noticed that quadratic and cubic processes within the fundamental $\mathrm{TM_{00}}$ mode always have the highest integral value, namely the highest susceptibility, compared to processes among different modes in which the mode orthogonality leads to the decrease of the integral value. Moreover,towards longer wavelengths, the integral value is also decreased due to the reduction of the waveguide confinement.

Thus, cascaded quadratic nonlinearities produced by phase mismatched SHGs, between the $\mathrm{TM_{00}}$ FW and SHs among all modes, are estimated as:

$\gamma_{\mathrm{casc,j}} = \frac{\omega}{c}\tilde{n}_{2,\mathrm{casc,j}} \cdot (\theta^{(2)}_{\mathrm{j;TM_{00}TM_{00}}})^2$, where $\tilde{n}_{2,\mathrm{casc,j}} \propto -(\bar{\chi}^{(2)}_{e;ee})^2/\Delta k_{\mathrm{j}}$ is the cascaded nonlinear RI, $\Delta k_{\mathrm{j}} = k_{\mathrm{j}}(2\omega) - 2k_{\mathrm{TM_{00}}}(\omega)$ is the phase mismatch parameter and k_{j} is the mode propagation constant. The negative sign indicates a self-defocusing nonlinearity under the positive Δk_{j}. $\gamma_{\mathrm{casc,TM_{00}}}$ contributes most to the total cascaded quadratic nonlinearity, since $\theta^{(2)}_{\mathrm{TM_{00};TM_{00}TM_{00}}}$ is the largest among other SHGs. Analogous, SPM contributes most to the Kerr nonlinearity, which is. $\gamma_{\mathrm{Kerr,TM_{00}}} = \frac{\omega}{c}\tilde{n}_{2,\mathrm{Kerr}} \cdot \theta^{(3)}_{\mathrm{TM_{00};TM_{00}TM_{00}TM_{00}}}$.

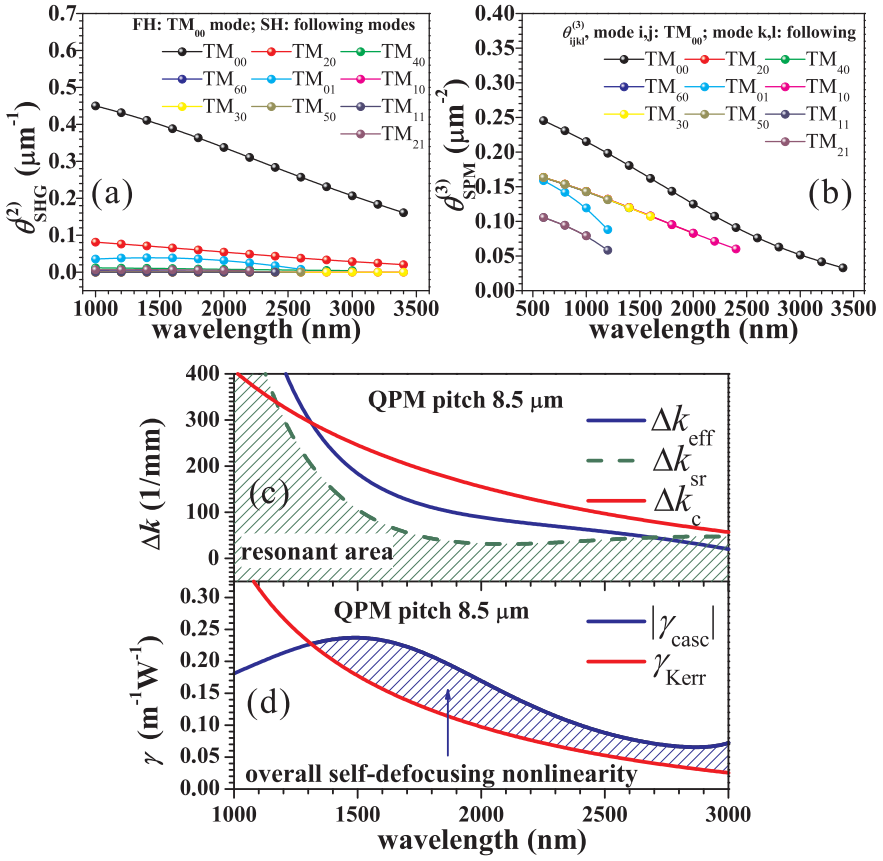

Fig. 4.13: (a) mode overlap integrals in SHG processes; (b) mode overlap integrals in self/cross phase modulations; (c) phase mismatch limits for overall self-defocusing nonlinearity and for clean soliton compressions; (d) nonlinear factors of both the cascaded quadratic nonlinearity and the Kerr nonlinearity. Waveguide has wd = 4 μm, dp = 2 μm.

Moreover, tuning the phase mismatch by QPM, the cascaded quadratic nonlinearity can be further enhanced. The goal is to reduce the phase mismatch to increase $\tilde{n}_{2,\mathrm{casc,TM_{00}}}$, but keep the effective phase mismatch nonzero and positive to ensure a self-defocusing cascaded nonlinearity.

The upper threshold Δk_c is defined from $\gamma_{\mathrm{casc,TM_{00}}} + \gamma_{\mathrm{Kerr,TM_{00}}} = 0$. The lower threshold Δk_sr is also defined with both FW and SH being set in the $\mathrm{TM_{00}}$ mode.

Figure 4.13(c) shows both Δk_c and Δk_sr. With a QPM pitch $\Lambda = 8.5$ μm, the phase mismatch is tuned to lie between the two limits. Correspondingly, $\gamma_{\mathrm{casc,TM_{00}}}$ and $\gamma_{\mathrm{Kerr,TM_{00}}}$ are shown in Fig. 4.13(d). An overall self-defocusing nonlinearity over a wide wavelength span $1.3 \sim 3.2$ μm is produced, with $|\gamma_{\mathrm{casc,TM_{00}}}| > \gamma_{\mathrm{Kerr,TM_{00}}}$. The phase-mismatch parameters of cascaded quadratic nonlinearities of higher-order modes, $\gamma_{\mathrm{casc,j}}$, are also tuned by QPM and may even find phase matching at short wavelengths, which will be discussed later in the paper. In the near- and mid-IR, these higher-order mode nonlinear factors are actually effectively self-focusing because the chosen QPM pitch makes the corresponding phase-mismatch parameters negative, but their contributions (strength) turns out to be quite weak compared to either $|\gamma_{\mathrm{casc,TM_{00}}}|$ or $\gamma_{\mathrm{Kerr,TM_{00}}}$. Therefore, within the compression window illustrated in Fig. 4.13(d) and recalling the all-normal dispersion profile provided in the waveguide, soliton formation in near- and mid-IR is accessible.

$\gamma_\mathrm{eff} = \gamma_{\mathrm{casc,TM_{00}}} + \gamma_{\mathrm{Kerr,TM_{00}}}$ again indicates the overall nonlinearity resulting from the competing. The nonlinear length is $L_{\mathrm{N,eff}} = (P_{\mathrm{in,TM_{00}}}\gamma_\mathrm{eff})^{-1}$, where $P_{\mathrm{in,TM_{00}}}$ is the peak power of the pump laser pulse in the $\mathrm{TM_{00}}$ mode. The dispersion length is $L_\mathrm{D} = T^2_{\mathrm{in,TM_{00}}}/|k^{(2)}_{\mathrm{TM_{00}}}|$, where $T_{\mathrm{in,TM_{00}}}$ is the pulse duration. Once more, the soliton number is estimated as: $N_\mathrm{eff} = \sqrt{L_\mathrm{D}/L_{\mathrm{N,eff}}}$.

The CQSC is then simulated by the NWEF model. In the LN waveguide with multiple modes, a group of NWEFs is used, each of them corresponds to a single mode and governs the electric field amplitude $\tilde{A}_\mathrm{j}$, while the transverse components $\tilde{B}_\mathrm{j}$ are degenerated through integrals. First, we show the self-defocusing soliton compression at 2 μm, see Fig. 4.14. The waveguide has wd $= 4$ μm, dp $= 2$ μm and provides all-normal dispersion within the guiding band. The QPM with pitch size $\Lambda = 8.5$ μm is applied so as to ensure a strong cascaded nonlinearity. The pump pulse, in the $\mathrm{TM_{00}}$ mode, has a full width at half maximum (FWHM) of 100 fs, similar to the thulium-fiber-based laser system used in [21]. The pulse peak power is 6 kW and therefore the pulse

energy is around 0.6 nJ, leading to an effective soliton order $N_{\text{eff}} \approx 3$.

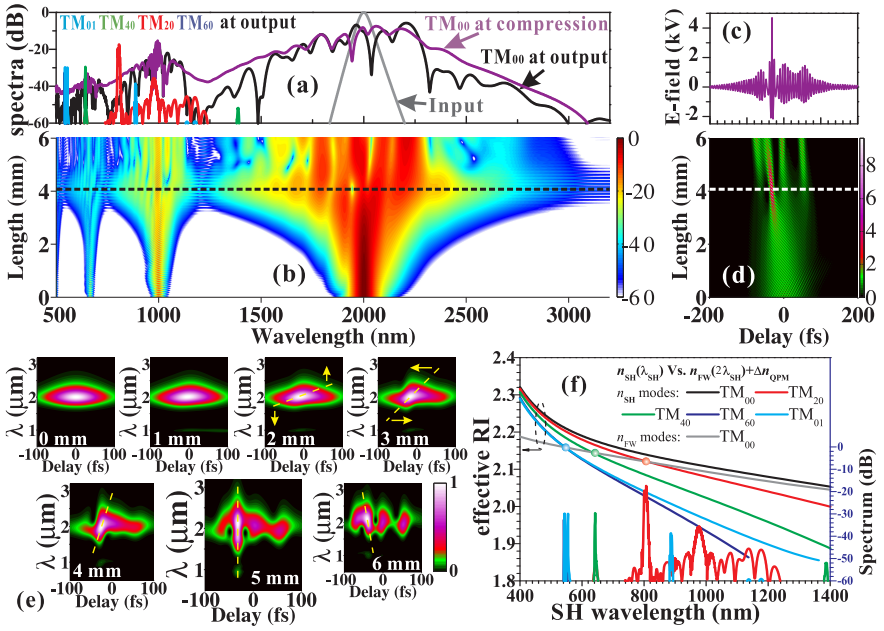

Fig. 4.14: numerical simulation of self-defocusing soliton compression at 2 μm in the LN waveguide; wd = 4 μm, dp = 2 μm, $\Lambda = 8.5$ μm, $\gamma_{\text{casc,TM}_{00}} = -0.169$ m^{-1}W^{-1}, $\gamma_{\text{Kerr,TM}_{00}} = 0.097$ m^{-1}W^{-1}, $k^{(2)}_{\text{TM}_{00}} = 0.151$ fs^2/μm; pump pulse has FWHM = 100 fs, energy 0.6 nJ, soliton order is $N_{\text{eff}} \approx 3$; modes taken into account are TM$_{00}$, TM$_{20}$, TM$_{40}$, TM$_{60}$ and TM$_{01}$; (a) spectra of the input pulse (TM$_{00}$ mode), the compressed pulse (TM$_{00}$ mode) and the output pulse (all modes); (b) pulse spectral evolution (TM$_{00}$ mode) with the first compression stage marked by the dash line; (c) TM$_{00}$ mode electric field amplitude at the first compression stage; (d) pulse temporal evolution (TM$_{00}$ mode); (e) pulse spectrogram evolution; (f) high-order mode SH radiations corresponding to phase matching positions.

Launched into the waveguide, the pulse spectrum is SPM broadened governed by the overall self-defocusing nonlinearity while a weak SH around 1 μm is accompanied due to the phase mismatched SHG process, see Fig. 4.14(a,b). The third harmonic and even higher order harmonics are also observed through both quadratic and cubic wave mixing processes. These harmonics look exactly like copies of the fundamental wave (FW) (in the frequency domain) but they

are much weaker due to much larger phase mismatch parameters. Therefore they will not impact the compression of the FW. Combined with the normal dispersion, the self-defocusing phase shift can be well compensated and the pulse, in time domain, is strongly compressed through the soliton self-compression effect to almost single-cycle, as is shown in Fig. 4.14(c,d).

As has been discussed in previous sections, LN has a strong Raman fraction ($f_{\mathrm{R}} \approx 50\%$, cf. also discussion [12]) which not only causes pulse spectral red shift, known as soliton self-frequency shift (SSFS) effects, but also gives rise to modulation instabilities impacting both the amplitude and the phase of the pulse spectrum [13,15]. The latter will further cause the pulse splitting, known as the Raman fission effects, if the soliton order is larger than unity. In Fig. 4.14(d), the Raman fission is observed after the first compression stage (marked with the white-dashed line). The soliton pulse is also red-shifted which is not obvious from the spectral figure but clues are found from the slight change in the temporal delay Fig. 4.14(d), as the red-shifted spectrum will have an increased group velocity (GV) when combined with the normal dispersion. Such a slight spectral red shift is actually from the competition between the Raman SSFS and cascading-induced self-steepening effects which cause spectral blue-shift due to the negative GV mismatch between the FW and the SH [22].

For a deeper understanding of such a soliton compression process, the pulse spectrogram evolution, with slices at different propagation distances, is shown in Fig. 4.14(e). The evolution starts with the domination of the nonlinearity which stretches the pulse spectrum while maintaining the temporal shape, resulting in a tilt on the spectrogram pattern, namely inducing the nonlinear phase shift. The slope of the tilt ($\frac{d\omega}{d\tau} = C$) reflects the pulse linear chirp (factor C) induced by the SPM. The normal dispersion also stretches the pulse but only on the temporal shape and then the tilt of the pattern is further adjusted with the nonlinear phase shift compensated. The tilt adjustment is $\frac{d\tau}{d\omega} = -k^{(2)}_{\mathrm{TM}_{00}} \cdot z$ (z is the propagation distance). The soliton compression is actually accomplished when the tilt of the pattern is turned from the initial horizonal state to the vertical state, while the compressed pulse will enter a relaxation stage upon further propagation as the tilt is overturned from the maximum compression vertical position. Typically a breather-kind of dynamics will then be observed with the soliton compressing and relaxing periodically and slowly entering into a steady state. The Raman fission is also clearly observed with mainly three fractions formed in the spectrogram pattern.

Moreover, while most energy remains in the TM_{00} mode, sharp-peak radiations are observed in high-order modes (Fig. 4.14(a)), which exactly correspond to the phase matching SHGs with SHs among high-order modes, see Fig. 4.14(f). The phase-matching condition scaled in RI is:

$$n_{\mathrm{SH,j}}(\lambda_{\mathrm{SH}}) = n_{\mathrm{FW,TM_{00}}}(2\lambda_{\mathrm{SH}}) + \Delta n_{\mathrm{QPM}}(\lambda_{\mathrm{SH}}) \tag{4.10}$$

where $\Delta n_{\mathrm{QPM}} = \frac{\lambda_{\mathrm{SH}}}{\Lambda}$ and λ_{SH} is the SH wavelength. However, due to their small modal nonlinear susceptibilities these radiations are weak in a similar way as the higher harmonics within the TM_{00} mode described above, and they will therefore not impact the soliton compression process either.

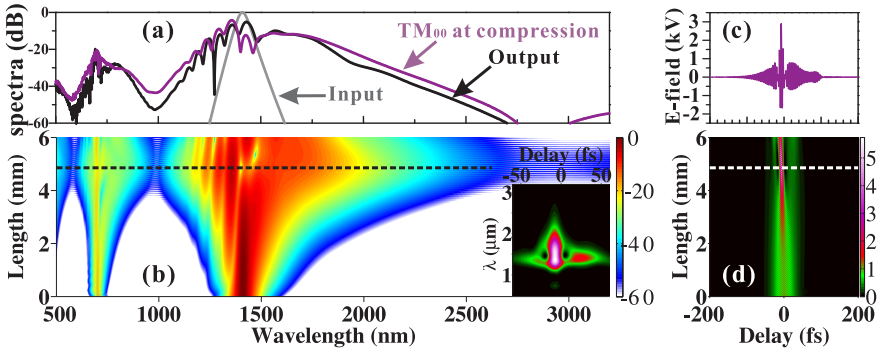

Fig. 4.15: self-defocusing soliton compression at 1.41 μm in the LN waveguide; waveguide has the same structure as Fig. 4.14; pump pulse has FWHM = 50 fs, energy 0.2 nJ, soliton order is $N_{\mathrm{eff}} \approx 1.5$; (a) TM_{00} mode spectra of the input pulse, the compressed pulse and the output pulse; (b) pulse spectral evolution (TM_{00} mode) with the first compression stage marked by the dash line; (c) TM_{00} mode electric field amplitude at the first compression stage; (d) pulse temporal evolution; insert: pulse spectrogram at the first compression stage.

The scenario of self-defocusing soliton compression also works at other wavelengths, e.g. at 1.41 μm shown in Fig. 4.15, at 1.58 μm shown in Fig. 4.16 and at 3 μm shown in Fig. 4.17, in which the soliton pulse can always be compressed to few-cycle and even single cycle. The waveguide for the 3 μm compression has a bigger size, wd = 5 μm, dp = 2.5 μm and the cutoff wavelength is extended to over 4 μm.

From these simulations we conclude that when having a small soliton order $1 < N_{\mathrm{eff}} < 2$, the compressed soliton has a quite clean temporal shape as well

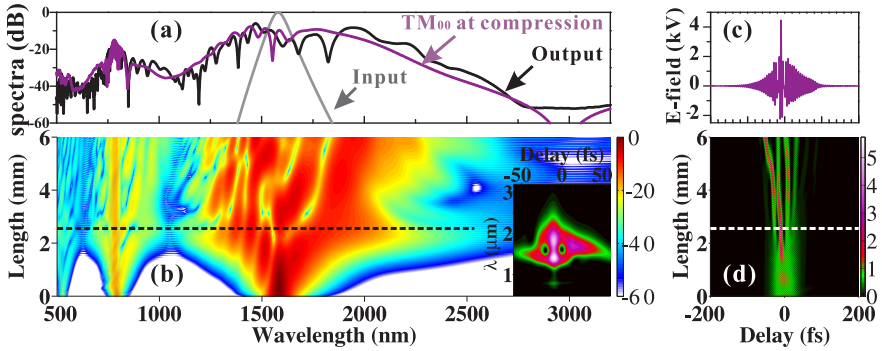

Fig. 4.16: self-defocusing soliton compression at 1.58 μm in the same LN waveguide; pump pulse has FWHM = 50 fs, energy 0.5 nJ, soliton order is $N_{\text{eff}} \approx 4$; (a) TM_{00} mode spectra of the input pulse, the compressed pulse and the output pulse; (b) pulse spectral evolution (TM_{00} mode) with the first compression stage marked by the dash line; (c) TM_{00} mode electric field amplitude at the first compression stage; (d) pulse temporal evolution; insert: pulse spectrogram at the first compression stage.

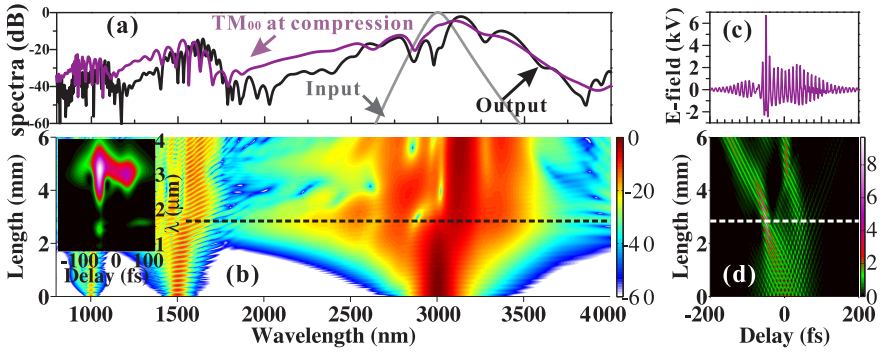

Fig. 4.17: numerical simulation of self-defocusing soliton compression at 3 μm in the LN waveguide; wd = 5 μm, dp = 2.5 μm, $\Lambda = 10$ μm, $\gamma_{\text{casc,TM}_{00}} = -0.063$ m^{-1}W^{-1}, $\gamma_{\text{Kerr,TM}_{00}} = 0.030$ m^{-1}W^{-1}, $k^{(2)}_{\text{TM}_{00}} = 0.531$ fs^2/μm; pump pulse has FWHM = 100 fs, energy 1.2 nJ, soliton order is $N_{\text{eff}} \approx 1.5$; (a) TM_{00} mode spectra of the input pulse, the compressed pulse and the output pulse; (b) pulse spectral evolution (TM_{00} mode) with the first compression stage marked by the dash line; (c) TM_{00} mode electric field amplitude at the first compression stage; (d) pulse temporal evolution (TM_{00} mode); insert: pulse spectrogram at the first compression stage.

as a clean pulse spectrogram pattern, due to the suppression of Raman fission effects. When the soliton order $N_{\text{eff}} > 2$, the compressed pulse will have a complex figure in both the pulse shape and the spectrogram pattern. The few-cycle soliton compression also leads to supercontinuum generation, which can easily span over an octave in the spectrum in the near- and mid-IR (at the -20 dB level).

If there are material and waveguide losses (additional to the insertion loss), e.g. $\alpha = 0.69$/cm for -3 dB/cm loss, soliton compressions as well as SCGs will be impacted. Since the soliton order is gradually decreased during the propagation, the anticipated pulse spectral broadening will shrink, which implies a degraded soliton compression.

We also investigate the spectral coherence of these soliton pulses. The pump pulse is assumed to contain a *one-photon-per-mode* (OPPM) noise figure ($\frac{h\omega}{\Delta\omega}e^{i\phi_{\text{rand}}}$, where h is the Planck constant, ω is the frequency, $\Delta\omega$ is the frequency resolution of the simulation window and ϕ_{rand} is a random phase between $0 \sim 2\pi$) [11].

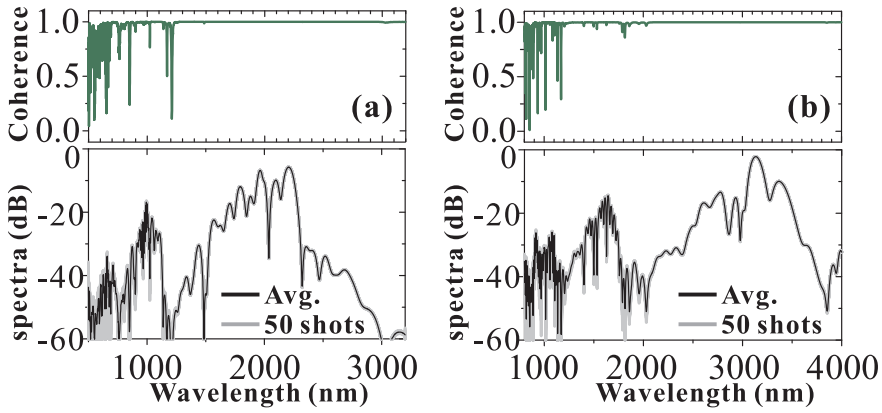

Fig. 4.18: coherence spectra for the output pulse spectrum in both the (a) 2-μm and (b) 3-μm compressions.

The first order spectral coherence $\tilde{g}_{12}^{(1)}$ is then calculated from several simulation shots, i.e.:

$$\tilde{g}_{12}^{(1)}(\omega) = \frac{\left|\left\langle \tilde{A}_s^*(\omega)\tilde{A}_l(\omega)\right\rangle\right|}{\sqrt{\left\langle\left|\tilde{A}_s(\omega)\right|^2\right\rangle\left\langle\left|\tilde{A}_l(\omega)\right|^2\right\rangle}},\ s \neq l \tag{4.11}$$

where s and l marks the simulation shot. The angle brackets indicate averaging over noise realizations.

The coherence of the output pulse spectrum in both the 2-μm and 3-μm compressions are shown in Fig. 4.18. The pulse spectrum in the near- and mid-IR is demonstrated to be highly coherent and the $\tilde{g}_{12}^{(1)}$ value is almost unity since the noise figure at lower frequency is weaker, while for shorter wavelengths where harmonics are generated, the coherence of the pulse spectrum is slightly reduced.

Such a high coherence is physically attributed to the low soliton order of the femtosecond pump that the noise-sensitive soliton fission regime and the pulse modulation instability (MI) are suppressed, compared to typical SCGs in PCFs which usually use picosecond pumps around the ZDW, with the soliton order over 100, so that strong soliton fission and MI is induced and the spectral coherence will be decreased [11]. Similar spectral high coherence is also observed in an all-nonlinear but non-solitary SCG process in [20] which is operated in the PCF designed to have all-normal dispersion and is dominated by the SPM from the traditional self-focusing Kerr nonlinearity.

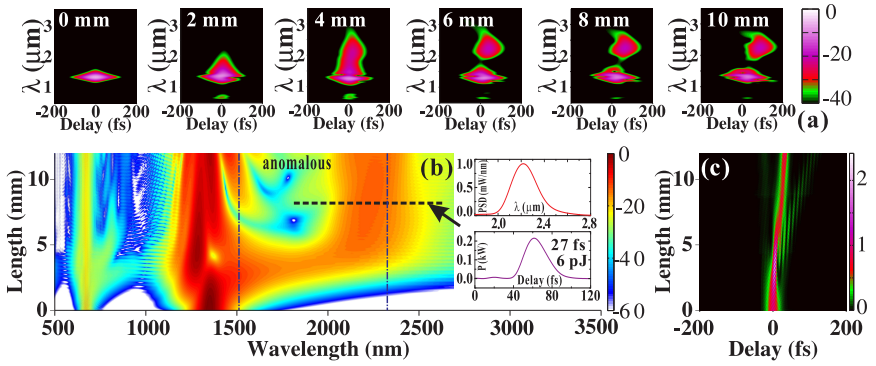

Fig. 4.19: broadband DW generation at 2.2 μm in the LN waveguide when pumping at 1.35 μm; wd = 5 μm, dp = 2.5 μm, $\Lambda = 9.8$ μm, $\gamma_{\mathrm{casc,TM_{00}}} = -0.217$ m^{-1}W^{-1}, $\gamma_{\mathrm{Kerr,TM_{00}}} = 0.152$ m^{-1}W^{-1}, $k^{(2)}_{\mathrm{TM_{00}}} = 0.049$ fs^2/μm; pump pulse has FWHM = 25 fs, energy 0.1 nJ, soliton order is $N_{\mathrm{eff}} \approx 1$; (a) pulse spectrogram evolution with slices at different propagation distance; (b) spectral evolution ($\mathrm{TM_{00}}$ mode); dash-dot lines mark the two ZDWs; (c) temporal evolution ($\mathrm{TM_{00}}$ mode); insert: DW pulse spectrum and temporal shape.

It is well-known that a soliton will radiate DWs when the dispersive phase (spectral propagation constant profile) is perturbed with high-order dispersion (third-order dispersion, fourth-order dispersion, etc.). In the present case that the soliton exists in the normal dispersion regime, the necessary condition for the DW generation is "the presence of an anomalous dispersion region". More precisely, according to the DW phase matching condition, DWs are predicted to be generated exactly in the anomalous dispersion region(s) if the major perturbation comes from the third-order dispersion. However, if presence of fourth-order dispersion, DWs can be generated either in anomalous or normal dispersion regions. The latter is actually revealed to be the SST effect in which the DW can actually form another soliton state, and an opposite dispersion region is considered as a necessary barrier [3].

Therefore, with an all-normal dispersion profile in the LN waveguide, DWs are suppressed for sure, see Fig. 4.15 and Fig. 4.16. The waveguide for the 3 μm compression actually has two ZDWs (1.51 μm and 2.30 μm), indicating an anomalous dispersion region sandwiched by two normal dispersion regions. However, DWs are still suppressed since the pumping wavelength is far away from the ZDWs and the DW phase-matching condition is not satisfied. Thus, without such linear radiations, the solitary pulse formation and compression dynamics is purely nonlinear.

On the other hand, when pumping close to one of the two ZDWs, DW generations are expected. Moreover, with the soliton spectral shifting and compression/relaxation breathing, the DW radiations can also form a few-cycle pulse [23].

We show a 2.2-μm pulse generation by means of such a breathing DW generation, see Fig. 4.19. The waveguide again has wd $= 5$ μm and dp $= 2.5$ μm. The QPM pitch is chosen to $\Lambda = 9.8$ μm to give an effective defocusing nonlinearity. The pump wavelength is chosen to 1.35 μm, which has phase matching to a DW at around 2.2 μm. The pump pulse has a FWHM of 25 fs so that an ultra-broadband spectrum is provided with large sideband energy at the DW position. The pulse energy is 0.1 nJ and the soliton order is $N_{\text{eff}} \approx 1$. The pulse spectrogram evolution is also investigated to help understanding the whole process, see Fig. 4.19(a) When launched into the waveguide, the soliton at 1.35 μm starts to transfer energy to the DW, and the soliton itself is spectrally blue shifted mainly due to a recoil effect [24, 25] (The cascading-induced blue shift and the Raman SSFS are almost balanced with each other). The soliton blue

shift is reflected by the temporal delay shown in Fig. 4.19(c). Meanwhile, the soliton is further compressed and more energy is transferred out to the DW, with a red-shifted DW position due to the phase-matching condition to the blue shifted soliton, see Fig. 4.19(b).

However, with energy continuously transferred out, the soliton is weakened with the soliton number going below the unity. Then, the soliton will self-adapt to maintain a soliton state by narrowing its pulse spectrum and broadening the temporal shape. A breath is therefore established, with the compression-induced spectral broadening and self-adaptive spectral narrowing, leaving a clean "DW pulse" pattern at 2.2 μm in the spectrogram. By applying a long-pass filter the DW-part of the spectrum is then filtered out so it can be analyzed in detail. It spans $2.0 \sim 2.6$ μm (at -10 dB level) and the pulse duration is estimated to be around 3.5-optical cycles (FWHM = 27 fs), see the insert in Fig. 4.19. The conversion efficiency is 6% leading to a pulse energy of 6 pJ.

It is noted that such a DW pulse is actually located in the anomalous GVD region and therefore it could not form a soliton. However, since the GVD in this regime is very weak, the temporal pulse shape will be almost unaffected even over a long propagation distance while spectral phase is accumulated by the self-defocusing nonlinearity.

The SST effect is also investigated in the same waveguide, with a more precise designing on the phase matching. The pump wavelength is set to be at 1.31 μm and the DW is therefore to be generated at 2.6 μm where the dispersion is also normal; thus, the DW can form a soliton state. We here keep the name "dispersive wave", as the phase-matching condition is found by intersecting the near-IR "parent" soliton dispersion curve, which is inherently dispersionless, with a dispersion curve that reflects the mode dispersion. Whether the formed DW is then energetic enough to form a soliton state that does not disperse, and thereby will not be a dispersive wave per se any more, is another matter. Moreover, both the parent soliton and the DW also have the same GV, as the GV-matching condition is satisfied, under which the energy transferred from the parent soliton to the DW will also be transferred back, reflecting a so-called soliton coupling effect [26]. Figure 4.20(a) shows how the soliton coupling evolves. Both the parent soliton and the DW spectra are periodically changed during the evolution, with the energy coupling in between (Fig. 4.20(b)). When having two solitons in the spectrogram, the temporal shape shows a interferometric signal (Fig. 4.20(c)).

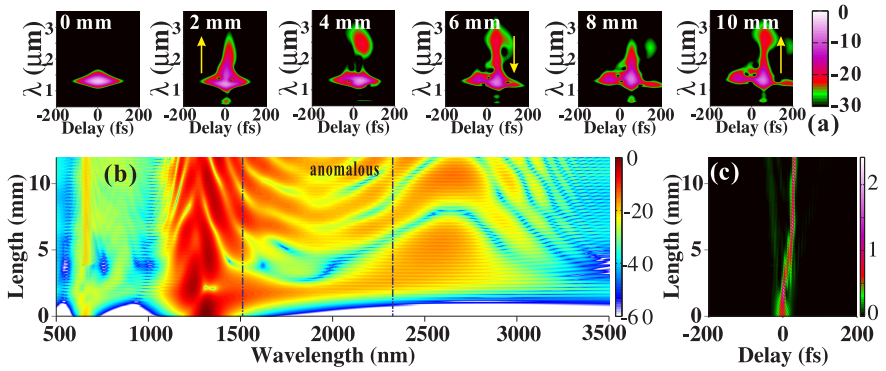

Fig. 4.20: soliton spectral tunneling effect with the pump at 1.31 μm and the DW pulse generated at 2.6 μm which is also solitonary; wd = 5 μm, dp = 2.5 μm, $\Lambda = 9.8$ μm, $\gamma_{\text{casc,TM}_{00}} = -0.204$ m^{-1}W^{-1}, $\gamma_{\text{Kerr,TM}_{00}} = 0.159$ m^{-1}W^{-1}, $k^{(2)}_{\text{TM}_{00}} = 0.063$ fs^2/μm; pump pulse has FWHM = 25 fs, energy 0.175 nJ, soliton order is $N_{\text{eff}} \approx 1$; (a) pulse spectrogram evolution with slices at different propagation distance; (b) spectral evolution (TM$_{00}$ mode); dash-dot lines mark the two ZDWs; (c) temporal evolution (TM$_{00}$ mode);

Compared to the SST effect, the 2.2-μm DW pulse generated in Fig. 4.19 cannot couple back to the near-IR soliton exactly because it is not GV-matched to the parent soliton, and it will therefore travel away from the parent soliton (this is quite unique to self-defocusing DW generations, see also the discussion in [27]). Through the SST, the parent soliton energy may be fully coupled to the DW pulse, provided that a spectral red-shift occurs, such as Raman SSFS [3]. However, with the cascading process, Raman SSFS is in most cases counterbalanced by cascading induced self-steepening effects, and the spectrum shows blue-shift dominated by the recoil effect, which unfortunately reduces the coupling efficiency. On the other hand, both cases are demonstrated to have also a high spectral coherence.

4.4 Conclusion

As a conclusion, in this chapter, we discussed the CQSC in quadratic nonlinear waveguides, which in general is a complementary solution to the CQSC in bulk crystals, as waveguide could provide good confinement on the laser beam and

therefore promote the efficiency of nonlinear interactions. Thus, laser pulses with small beam size, nJ-level energy and high repetition rate could be operated to the few-cycle regime.

we first investigated commonly used LN waveguides, in particular a LN/LT ridge waveguide which has step RI change that enables a clear waveguide profile and accurate theoretical analysis. These waveguides in common have a small RI change, limited either by the chemical fabrication technologies or by close properties between the core and substrate materials. The small RI change implies that the dispersion profile of the waveguide mode is kept similar to the material dispersion, having the same ZDW and being inherently phase mismatched in the noncritical SHG as well. Therefore, without QPM, strong cascading is produced, with which the material Kerr nonlinearity is counterbalanced and overall self-defocusing nonlinearity is accessed over a broadband wavelength range ($1100 \sim 3000$ nm). Then, the operational wavelength range of the CQSC is from 1100 nm to the ZDW at 1900 nm, covering the whole communication band, just like the bulk LN.

The CQSC in the LN/LT waveguide with 10-nJ laser pump pulses was numerically simulated at 1550 nm, with single-cycle solitary pulses being generated. When pumping with longer pulses, i.e. having a higher pulse energy (e.g. 30 nJ), octave spanning SCG dominated by the cascaded quadratic nonlinearity is accomplished. In APE waveguides, cascading based SCGs were experimentally observed as well. The proof of concept of CQSC in such small-RI-changed waveguides could extensively extend the application of quadratic waveguides, from phase matching based frequency conversions to QPM-free and phase mismatched ultrafast cascading applications.

we also proposed a LN ridge waveguide design with a large refractive index (RI) change, a design intended to extend the CQSC further into the mid-IR. The large RI change is suggested to come from bonding an LN wafer on top of a glass substrate with broadband IR transmission and substantially lower RI than LN. Compared to bulk LN or traditional low-RI LN waveguides, in which the dispersion trend limits the compression to be below the ZDW, the proposed design significantly extends the soliton regime of LN waveguides into the mid-IR. This occurs due to the strong waveguide dispersion that can significantly alter and even counterbalance the material dispersion. Thus, the normal dispersion regime can be extended well beyond the material ZDW. It is even possible to create an all-normal dispersion profile (within the waveg-

uide cutoff frequencies) by properly tuning the waveguide core size. Such an all-nonlinear and solitonic waveguide or fiber design has to our knowledge not been investigated before. The large RI change also has the benefit of supporting broadband guidance well into the mid-IR, and at the same time keep the waveguide core size small (in contrast to a broadband low-RI design [28]). The large confinement from the small core leads to a very low-energy (sub-nJ-level) soliton threshold, implying that the pump source can operate at much lower average powers or higher repetition rates than traditional LN waveguide designs. Moreover, effective self-defocusing nonlinearity is also found over a broadband range in near and mid-IR, through the cascaded phase mismatched SHG. But as the phase mismatch parameter is tailored large by the dispersion engineering, a moderate QPM pitch on the order of 10 μm has to be used.

CQSCs at 2 μm, 3 μm and other wavelengths were then numerically investigated, in which single-cycle pulses can be generated through the soliton self-compression effect, accompanied with octave-spanning supercontinuum generation in sub-cm length waveguides. Using a 100 fs pump pulse and keeping a low soliton order, the pulse spectrum was demonstrated to be highly coherent. We attribute this to the purely nonlinear soliton dynamics and the suppression of the soliton fission and the modulation instability. For designs where the dispersion profile have multiple ZDWs, e.g. an anomalous-dispersion region could be found sandwiched between two normal-dispersion regimes. In this scenario DW generations as well as the SST effect were investigated. The DWs could manifest as few-cycle pulses under a breathing regime induced by the spectral soliton shift and compression/relaxation processes of the parent soliton. As for the SST effect, the group-velocity matching enables the energy coupling between the DW and the parent soliton, and in this case the wavelength of the DW phase-matching point pulse is actually located in the long-wavelength normal dispersion range beyond the anomalous dispersion regime, and therefore may form a solitary wave packet.

Executing such a large-RI-changed waveguide design should not pose too many obstacles, and it therefore has a number of exciting advantages over traditional designs, both from a nonlinear science viewpoint and from an application viewpoint. Such waveguides could lead to more effective ways of generating few-cycle pulses and highly coherent SCG with low-energy femtosecond pulses in near and mid-IR.

Bibliography

[1] C. Langrock, S. Kumar, J. McGeehan, A. Willner, and M. Fejer, "All-optical signal processing using $\chi^{(2)}$ nonlinearities in guided-wave devices," Lightwave Technology, Journal of **24**, 2579–2592 (2006).

[2] R. Schiek, Y. Baek, and G. I. Stegeman, "Second-harmonic generation and cascaded nonlinearity in titanium-indiffused lithium niobate channel waveguides," J. Opt. Soc. Am. B **15**, 2255–2268 (1998).

[3] V. Serkin, V. Vysloukh, and J. Taylor, "Soliton spectral tunnelling effect," Electron. Lett. **29**, 12–13(1) (1993).

[4] C. R. Phillips, C. Langrock, J. S. Pelc, M. M. Fejer, I. Hartl, and M. E. Fermann, "Supercontinuum generation in quasi-phasematched waveguides," Opt. Express **19**, 18754–18773 (2011).

[5] V. Ulvila, C. R. Phillips, L. Halonen, and M. Vainio, "Frequency comb generation by a continuous-wave-pumped optical parametric oscillator based on cascading quadratic nonlinearities," Opt. Lett. **38**, 4281–4284 (2013).

[6] O. Tadanaga, T. Yanagawa, Y. Nishida, H. Miyazawa, K. Magari, M. Asobe, and H. Suzuki, "Efficient 3-μm difference frequency generation using direct-bonded quasi-phase-matched $LiNbO_3$ ridge waveguides," Appl. Phys. Lett. **88**, 061101 (2006).

[7] K. Okamoto, "Fundamentals of optical waveguides," (2010).

[8] M. Bache, "Designing microstructured polymer optical fibers for cascaded quadratic soliton compression of femtosecond pulses," J. Opt. Soc. Am. B **26**, 460–470 (2009).

[9] G. Agrawal, "Nonlinear fiber optics," (2013).

[10] M. Bache, J. Moses, and F. W. Wise, "Scaling laws for soliton pulse compression by cascaded quadratic nonlinearities," J. Opt. Soc. Am. B **24**, 2752–2762 (2007).

[11] J. M. Dudley, G. Genty, and S. Coen, "Supercontinuum generation in photonic crystal fiber," Rev. Mod. Phys. **78**, 1135–1184 (2006).

[12] M. Bache and R. Schiek, "Review of measurements of Kerr nonlinearities in lithium niobate: the role of the delayed Raman response," ArXiv e-prints p. 1211.1721 (2012).

[13] V. N. Serkin, T. L. Belyaeva, G. H. Corro, and M. A. Granados, "Stimulated Raman self-scattering of femtosecond pulses. i. soliton and non-soliton regimes of coherent self-scattering," Quantum Electronics **33**, 325 (2003).

[14] G. Agrawal, *Nonlinear Fiber Optics*, Academic Press (Academic Press, 2013).

[15] V. N. Serkin, T. L. Belyaeva, G. H. Corro, and M. A. Granados, "Stimulated raman self-scattering of femtosecond pulses. I. soliton and non-soliton regimes of coherent self-scattering," Quant. Electron. **33**, 325 (2003).

[16] T. C. Wong, M. Rhodes, and R. Trebino, "Single-shot measurement of the complete temporal intensity and phase of supercontinuum," Optica **1**, 119–124 (2014).

[17] P. Rabiei, J. Ma, S. Khan, J. Chiles, and S. Fathpour, "Heterogeneous lithium niobate photonics on silicon substrates," Opt. Express **21**, 25573–25581 (2013).

[18] A. Herzog, B. Hadad, V. Lyubin, M. Klebanov, A. Reiner, A. Shamir, and A. A. Ishaaya, "Chalcogenide waveguides on a sapphire substrate for mid-IR applications," Opt. Lett. **39**, 2522–2525 (2014).

[19] M. Bass, C. DeCusatis, J. Enoch, V. Lakshminarayanan, G. Li, C. MacDonald, V. Mahajan, and E. Van Stryland, *Handbook of Optics, Third Edition Volume IV: Optical Properties of Materials, Nonlinear Optics, Quantum Optics (set)*, Handbook of Optics (McGraw-Hill Education, 2009).

[20] A. M. Heidt, "Pulse preserving flat-top supercontinuum generation in all-normal dispersion photonic crystal fibers," J. Opt. Soc. Am. B **27**, 550–559 (2010).

[21] C. R. Phillips, C. Langrock, J. S. Pelc, M. M. Fejer, J. Jiang, M. E. Fermann, and I. Hartl, "Supercontinuum generation in quasi-phase-matched $LiNbO_3$ waveguide pumped by a Tm-doped fiber laser system," Opt. Lett. **36**, 3912–3914 (2011).

[22] H. Guo, X. Zeng, B. Zhou, and M. Bache, "Nonlinear wave equation in frequency domain: accurate modeling of ultrafast interaction in anisotropic nonlinear media," J. Opt. Soc. Am. B **30**, 494–504 (2013).

[23] M. Bache, O. Bang, B. B. Zhou, J. Moses, and F. W. Wise, "Optical cherenkov radiation by cascaded nonlinear interaction: an efficient source of few-cycle energetic near- to mid-IR pulses," Opt. Express **19**, 22557–22562 (2011).

[24] N. Akhmediev and M. Karlsson, "Cherenkov radiation emitted by solitons in optical fibers," Phys. Rev. A **51**, 2602–2607 (1995).

[25] D. V. Skryabin, F. Luan, J. C. Knight, and P. S. J. Russell, "Soliton self-frequency shift cancellation in photonic crystal fibers," Science **301**, 1705–1708 (2003).

[26] H. Guo, S. Wang, X. Zeng, and M. Bache, "Understanding soliton spectral tunneling as a spectral coupling effect," Photon. Technol. Lett., IEEE **25**, 1928–1931 (2013).

[27] M. Bache, O. Bang, B. B. Zhou, J. Moses, and F. W. Wise, "Optical Cherenkov radiation in ultrafast cascaded second-harmonic generation," Phys. Rev. A **82**, 063806 (2010).

[28] H. Guo, X. Zeng, B. Zhou, and M. Bache, "Few-cycle solitons and supercontinuum generation with cascaded quadratic nonlinearities in unpoled lithium niobate ridge waveguides," Opt. Lett. **39**, 1105–1108 (2014).

Chapter 5

Conclusions and Outlooks

5.1 Conclusions

In this thesis, we investigated the Ph.D. project *cascaded quadratic soliton compression (CQSC) in waveguide structures.*

CQSC is proposed as a one-step pulse compression scheme which can be used as a subsequent component after commercial femto-second pulsed laser systems, e.g. the solid state laser system and the fiber laser system. It makes use of the property of the self-compression of high order solitons, with the spontaneous cancelation between the nonlinear and dispersive effects in the medium. In quadratic waveguides, the nonlinearity is produced through the cascaded phase mismatched second harmonic generation process, which equivalently induces an intensity-related nonlinear phase shift just like the cubic Kerr nonlinearity. More importantly, such Kerr-like cascaded nonlinearity can be flexibly tuned in both the amplitude and the sign, making possible of the CQSC under the self-defocusing effects and in the normal dispersion region, in oppose to most compression schemes in Kerr materials.

The waveguide structure imposed on the quadratic crystals provides confinement on the laser beam so that the spatial diffraction effects and the spatio-temporal effects in the few-cycle regime can be suppressed, making it capable to operate low energy, high repetition rate pulsed lasers with moderate long durations. Therefore, femtosecond fiber lasers with nano-joule energy, mega-hertz repetition rate and $\sim$ 100 fs pulse duration can be compressed to few-cycle or even single cycle. The structural design on the waveguide also enables the dispersion engineering with which the overall normal dispersion can be achieved and tuned at targeted laser wavelength for the self-defocusing CQSC.

Quadratic nonlinear waveguides with both small and large refractive index (RI) changes were investigated, including the analysis on waveguide eigenmodes, the dispersion engineering and the estimation of the waveguide nonlinearity. Numerical model nonlinear wave equation in frequency domain (NWEF) was derived to solve the electric field dynamics of the propagated laser pulses, which helps to prove the concept of CQSC in both quadratic bulk crystals and waveguides. In quadratic waveguides with a small RI change ($\Delta n \ll 0.1$), e.g. the anneal proton exchanged (APE) lithium niobate (LN) waveguides or wafer bonded lithium niobate lithium tantalite (LN/LT) ridge waveguide, CQSC as well as self-defocusing soliton induced supercontinuum generations was demonstrated. The waveguide was turned out to be naturally suitable in producing the strong and self-defocusing Kerr-like effects without the help of quasi-phase-

matching (QPM) technology. The operational wavelength range covers the communication band in the near-infrared range. In waveguides with a large RI change ($\Delta n > 0.1$), the guidance band of the waveguide is substantively extended into the mid-infrared range while flexible dispersion engineering is evoked. All normal dispersion profiles could then be achieved, with which the CQSC could actually operate a mid-infrared pulse at e.g. 3 μm. Few-cycle, mid-infrared laser pulses can also be generated through the dispersive wave generation fed by a near-infrared solitary pulse.

The generation of high intensity and few-cycle laser pulses in near and mid-infrared ranges is of great interests to a variety of applications, e.g. the time-resolved spectroscopy.

5.2 Outlooks

During the project, we noticed that today *wafer bonding* is being used in the fabrication of optical waveguides including the quadratic waveguide, which is a physical method compared to commonly used chemical fabrication methods (such as APE). Wafer bonding is robust as materials from different classes can be bonded together, making e.g. LN/silica waveguides [1], chalcogenide/s-apphire waveguides [2], etc. To quadratic waveguides, wafer bonding could promise that 1) a variety of materials that has excellent optical properties such as wide transparency and high nonlinearity can be accessed; 2) the RI change can be made large with a substrate having much lower RI, like the LN/silica waveguide, therefore the dispersion engineering can make effect; and 3) the damage threshold is much higher than chemically fabricated waveguides.

In the thesis, we have numerically investigated the wafer bonded LN/LT waveguide [3, 4] which has a ridge waveguide structure with step-index-change profile. We also proposed a LN/glass waveguide, analogous to the LN/silica waveguide, that is supposed to accomplish the mid-infrared CQSC. But actually, LN is not a typical mid-infrared crystal. Its transparency window is only to $\sim$4 μm. Meanwhile, the strong Raman fraction in LN is always a problem to the CQSC.

Therefore, the future research is suggested to focus on the wafer bonded quadratic waveguides with novel mid-infrared crystals other than LN, e.g. the lithium thioindate (LIS) that has been discussed in chapter 3 as a mid-infrared candidate to the CQSC. LIS is in the same class to LN, but has a much wider

transparency window in the mid-infrared range and a much lower fraction of the Raman effects. On the other hand, QPM can also be applied on LIS to help boosting the cascaded nonlinearity.

We are also looking forward to more applications based on the mid-infrared quadratic waveguides other than the CQSC.

Bibliography

[1] P. Rabiei, J. Ma, S. Khan, J. Chiles, and S. Fathpour, "Heterogeneous lithium niobate photonics on silicon substrates," Opt. Express **21**, 25573–25581 (2013).

[2] A. Herzog, B. Hadad, V. Lyubin, M. Klebanov, A. Reiner, A. Shamir, and A. A. Ishaaya, "Chalcogenide waveguides on a sapphire substrate for mid-IR applications," Opt. Lett. **39**, 2522–2525 (2014).

[3] Y. Nishida, H. Miyazawa, M. Asobe, O. Tadanaga, and H. Suzuki, "0-db wavelength conversion using direct-bonded QPM-Zn:$LiNbO_3$ ridge waveguide," IEEE Photon. Technol. Lett. **17**, 1049–1051 (2005).

[4] O. Tadanaga, T. Yanagawa, Y. Nishida, H. Miyazawa, K. Magari, M. Asobe, and H. Suzuki, "Efficient 3-μm difference frequency generation using direct-bonded quasi-phase-matched $LiNbO_3$ ridge waveguides," Appl. Phys. Lett. **88**, 061101 (2006).

Appendix A

MATLAB Solvers: NWEF, CWEs and NLS-like Equation

A.1 NWEF for Type-0/Isotropic interactions

```
function [EV, ET, EW, W] = ...
    NWEF_Type0(T, Z, w0, w_span, E, alpha, beta, gamma, fr, RW, vg, qpm_k)
% Hairun Guo, 29-10-2013
% nonlinear wave equation in frequency domain, single equation for Type-0
% or isotropic interactions, including both quadratic and cubic nonlinear
% induced polarizations.
% ========================================================================
%  input:          (physical)
%      T: {nx1} temporal delay grid
%      Z: {1xm} propagation grid
%     w0: {1x1} central angular frequency
% w_span: {1x2} concerned frequency range
%      E: {nx1} intial E-field [V/m]
%
%  alpha: {nx1} attenuation factor
%   beta: {nx1} full dispersive phase profile
%  gamma: {nx2} nonlinear factor
%         gamma(:,1) = chi_2.*W.^2./(2*c^2*beta) [1/V]
%         gamma(:,2) = chi_3.*W.^2./(2*c^2*beta) [m/V^2]
%         chi_2: quadratic material susceptibility or modal susceptibility
%         chi_3: cubic material susceptibility or modal susceptibility
%
%     fr: {1x1} Raman fraction
%     RW: {nx1} Raman response spectra
%     vg: {1x1} pulse group velocity at frequency w0
%  qpm_k: {1x1} detuned phase mismatch if having QPM structure
%         qpm_k = 2*pi/pitch
%
% output:
%     EV: {nxm} temporal E-field complex envelope
%     ET: {nxm} temporal E-field (real-valued)
%     EW: {nxm} spectral profile
%      W: {nx1} frequency grid
% ========================================================================

n = length(T); dT = T(2)-T(1);          % grid parameters
V = 2*pi*(-n/2:n/2-1)'/(n*dT);          % frequency grid

L = 1i*beta + alpha;                    % linear operator

w1 = find(V >= w_span(1),1,'first');
w2 = find(V <= w_span(2),1, 'last');
W = V(w1:w2);
isw = (abs(V)>=w_span(1) & abs(V)<=w_span(2));

isw = fftshift(isw);
L  = fftshift(L);
gamma = fftshift(gamma,1);              % shift to fft domain
RW = fftshift(RW);                      % frequency domain Raman
E = fftshift(E,1);
```

```
% === set error control options
options = odeset('RelTol', 1e-5, 'AbsTol', 1e-12, ...
                 'NormControl', 'on', ...
                 'OutputFcn', @(z,y,flag) report(z,y,flag,Z(end)));
[Z, ET] = ode45(@(z, Ew) rhs(z, Ew, dT, L, gamma, fr, RW, qpm_k), ...
                Z, fft(E).*dT, options);% run integrator

% === process output of integrator
EW = zeros(w2-w1+1, length(Z));
for i = 1:length(Z)
    Ew = ET(i,:).*isw.'.*exp(-L.'*Z(i)+1i*vg^-1*Z(i).*fftshift(V,1).');
                                        % change variables
    ET(i,:) = fftshift(real(ifft(Ew)./dT));
    Ew = fftshift(Ew);
    EW(:,i) = Ew(w1:w2);
end
ET = ET.';
EV = envelope(ET,V,w0);

% === define function to return the RHS of Eq. (3.13)
function R = rhs(z, Ew, dT, L, gamma, fr, RW, qpm_k)
Et = real(ifft(Ew.*exp(-L*z))./dT);     % time domain field
Es = Et.^2;                             % time domain square

QN = -1i.*gamma(:,1).*fft(Es).*dT.*square(qpm_k*z+pi/2);
                                        % 2nd order nonlinearity

if fr <eps                              % no Raman case
    RS = 0;
else
    RS = fr*fft(Et.*real(ifft(RW.*fft(Es).*dT)./dT)).*dT;
end                                     % Raman scattering

CN = -1i.*gamma(:,2).*((1-fr)*fft(Et.*Es).*dT + RS);

R = (QN+CN).*exp(L*z);                  % full RHS

% === define function to print ODE integrator status
function status = report(z, ~, flag, zl)
status = 0;
if isempty(flag)
    fprintf('%05.1f %% complete\n', z/zl*100);
end

function [EV] = envelope(ET, W, w0)
% ET: real valued field in time domain,  [-T T]
% W : frequecny axis vector,       [-Ws/2 Ws/2]
% w0: center frequency,
% EV: complex field envelope
format long

[n, m] = size(ET);
EW = fftshift(fft(fftshift(ET,1)),1);
```

```
[~,W_grid] = meshgrid(zeros(1,m),(W>0));
EW = (W_grid).*EW;

n0 = find(W<=w0,1,'last');

EW = [EW(n0:n,:); EW(1:n0-1,:)];
EV = 2*(fftshift(ifft(EW),1));
```

A.2 CWEs for SHG process

```
function [AT1, AT2, AW1, AW2, W] =...
    CWEs_SHG(T, Z, w0, w_span, A, alpha, beta, gamma, fr, RW, eta, B, dk)
% Hairun Guo, 29-10-2013
% coupled wave equations for SHG process.
% [Ref] M. Bache, J. Moses, and F. W. Wise, "Scaling laws for soliton pulse
% compression by cascaded quadratic nonlinearities," J. Opt. Soc. Am. B 24,
% 2752-2762 (2007).
% ============================================================================
%  input:          (physical)                |       (dimensionless)
%      T: {nx1} temporal delay grid          |  T/T01,  T0: FH pulse duration
%      Z: {1xm} propagation grid             |  Z/LD1, LD1: FH dispersion length
%     w0: {1x1} FH angular frequency         |  w0*T01
% w_span: {1x2} concerned frequency range    |  w_span.*T0
%      A: {nx2} intial pulse [W^0.5/m]       |  A/sqrt(I1),
%                                            |    I1: FH initial peak power
%  alpha: {nx2} attenuation factor           |  alpha*LD1
%   beta: {nx2} full dispersion              |  beta/GVD1
%  gamma: {nx2} nonlinear factor             |
%               gamma(:,1) [W^-0.5]          |  LD1*gamma(:,1)*I1^0.5 = ...
%                                            |                    dk^0.5*N_casc
%               gamma(:,2) [m/W]             |  LD1*gamma(:,2)*I1 = N_Kerr^2
%     fr: {1x1} Raman fraction               |  fr
%     RW: {nx1} Raman response function      |  RW./T0
%    eta: {1x1} n1/n2                        |
%      B: {1x1} 2 or 2/3, type-0 or type-I   |
% output:                                    |
%     AT: {nxm} temporal profile             |  AT./sqrt(I1)
%     AW: {nxm} spectral profile             |  AW./sqrt(I1)./T01
%      W: {nx1} frequency grid               |  W*T01
% ============================================================================

n = length(T); dT = T(2)-T(1);          % grid parameters
V = 2*pi*(-n/2:n/2-1)'/(n*dT);          % frequency grid
W = [V+w0 V+2*w0];                      % the absolute frequency grid
isw = [(W(:,1)>=w_span(1,1) & W(:,1)<=w_span(2,1)) ...
       (W(:,2)>=w_span(1,2) & W(:,1)<=w_span(2,2))];
                                        % spectral boundary
```

```
L = 1i.*beta + alpha/2;                 % linear operator
S = [1+V./w0 1+0.5.*V./w0];             % self steepening term

isw = fftshift(isw,1);
L = fftshift(L,1);
S = fftshift(S,1);
gamma = fftshift(gamma,1);              % shift to fft space
RW = fftshift(RW);

% === set error control options
options = odeset('RelTol', 1e-5, 'AbsTol', 1e-12, ...
                 'NormControl', 'on', ...
                 'OutputFcn', @(z,y,flag) report(z,y,flag,Z(end)));
[Z, Y] = ode45(@(z, AW) rhs(z, AW, dT, L, S, gamma, fr, RW, eta, B, dk), ...
               Z, fft(A).*dT, options);% run integrator

% === process output of integrator
[mY nY] = size(Y.');
AT1 = zeros(mY/2,nY);
AT2 = AT1;
AW1 = AT1;
AW2 = AT1;
for i = 1:length(Z)
    AW = Y(i,:).*isw(1:end).*exp(-L(1:end)*Z(i));
    AT1(:,i) = ifft(AW(  1:n  ))./dT;   % time domain output
    AT2(:,i) = ifft(AW(n+1:end))./dT;
    AW1(:,i) = fftshift(AW(  1:n  ));   % change variables
    AW2(:,i) = fftshift(AW(n+1:end));
end

% === define function to return the RHS of Eq. (3.13)
function R_v = rhs(z, AW_v, dT, L, S, gamma, fr, RW, eta, B, dk)
n = length(AW_v)/2;
AW = reshape(AW_v,n,2);

AT = ifft(AW.*exp(-L*z))./dT;           % time domain field
AT1 = AT(:,1);  AT2 = AT(:,2);

FH2 = fft(conj(AT1).*AT2).*dT.*exp(-1i*dk*z);
SH2 = fft(AT1.^2)        .*dT.*exp( 1i*dk*z);
FH3 = fft(AT1.*(abs(AT1).^2+B*eta   *abs(AT2).^2)).*dT;
SH3 = fft(AT2.*(abs(AT2).^2+B*eta^-1*abs(AT1).^2)).*dT;

if (abs(fr) < eps)                      % no Raman case
    FH_RS = 0;
    SH_RS = 0;
else
    FH_RS = fft(AT1.*ifft(RW.*fft(abs(AT1).^2+eta   *abs(AT2).^2).*dT)./dT).*dT;
    SH_RS = fft(AT2.*ifft(RW.*fft(abs(AT2).^2+eta^-1*abs(AT1).^2).*dT)./dT).*dT;
end
R1 = ...
    -1i*gamma(:,1).*S(:,1).*FH2 ...
    -1i*gamma(:,2).*S(:,1).*((1-fr).*FH3+2/3*fr.*FH_RS);
R2 = ...
```

```
    -1i  *gamma(:,1).*S(:,2).*SH2 ...
    -1i*2*gamma(:,2).*S(:,2).*((1-fr).*SH3+2/3*fr.*SH_RS)*eta^2;
R = [R1 R2].*exp(L*z);
R_v = reshape(R, 2*n, 1);

% === define function to print ODE integrator status
function status = report(z, ~, flag, zl)
status = 0;
if isempty(flag)
    clc;
    fprintf('%05.1f %% complete\n', z/zl*100);
end
```

A.3 Full NLS-like Equation Degenerated from SHG CWEs

```
function [AT, AW, W] = ...
    NLSE_like(T, Z, w0, w_span, A, alpha, beta, gamma, fr, RW, eta, B)
% Hairun Guo, 29-10-2013
% nonlinear schordinger like equation includes attenuation, XPM and Raman
% scattering.
% ============================================================================
%  input:          (physical)                |       (dimensionless)
%      T: {nx1} temporal delay grid          |  T/T0, T0: pulse duration
%      Z: {1xm} propagation grid             |  Z/LD, LD: dispersion length
%     w0: {1x1} central angular frequency    |  w0*T0
% w_span: {1x2} concerned frequency range    |  w_span.*T0
%      A: {nx1} intial pulse [W^0.5/m]       |  A/sqrt(I),
%                                            |    I: initial peak intensity
%  alpha: {nx1} attenuation factor           |  alpha*LD
%   beta: {nx1} full dispersion              |  beta/GVD
%  gamma: {nx2} nonlinear factor [m/W]       |  LD*gamma*I = N^2,
%                                            |    N: soliton order
%     fr: {1x2} cascading & Raman fraction   |  fr
%     RW: {nx2} response spectra             |  RW/T0
%    eta: {1x1} XPM prefactor n1/n2/Dk       |  eta/LD
%      B: {1x1} type-0:     2                |
%               type-I:   3/2                |
% output:                                    |
%     AT: {nxm} temporal profile             |  AT./sqrt(I)
%     AW: {nxm} spectral profile             |  AW./sqrt(I)./T0
%      W: {nx1} frequency grid               |  W*T0
% ============================================================================

if length(beta(1,:)) ~= 1
    error('haig: check dimensions of beta !');
end
if length(gamma(1,:)) ~= 2
```

```
    error('haig: check dimensions of gamma !');
end
if length(fr) ~=2
    error('haig: check dimensions of fr !');
end
if length(RW(1,:)) ~= 2
    error('haig: check dimensions of RT !');
end
if nargin <11
    B = 2;                                  % type-0
end
if nargin <10
    eta = 0;
end

n = length(T); dT = T(2)-T(1);              % grid parameters
V = 2*pi*(-n/2:n/2-1)'/(n*dT);              % frequency grid

W = V + w0;                                 % the absolute frequency grid
isw = (W>=w_span(1) & W<=w_span(2));

L = 1i*beta + alpha/2;                      % linear operator

S1 = (V +   w0)./   w0 ;
S2 = (V + 2*w0)./(2*w0);                    % self steepening term

isw = fftshift(isw);
L  = fftshift(L);
S1 = fftshift(S1);
S2 = fftshift(S2);                          % shift to fft space
gamma = fftshift(gamma,1);                  % shift to fft space
RW = fftshift(RW,1);                        % frequency domain Raman

% === set error control options
options = odeset('RelTol', 1e-5, 'AbsTol', 1e-12, ...
                 'NormControl', 'on', ...
                 'OutputFcn', @(z,y,flag) report(z,y,flag,Z(end)));
[Z, Y] = ode45(@(z, AW) rhs(z, AW, dT, L, S1, S2, gamma, fr, RW, eta, B), ...
               Z, fft(A).*dT, options);% run integrator

% === process output of integrator
AT = zeros(size(Y.'));
AW = AT;
for i = 1:length(Z)
    AW(:,i) = Y(i,:).*isw.'.*exp(-L.'*Z(i));
                                            % change variables
    AT(:,i) = ifft(AW(:,i))./dT;            % time domain output
    AW(:,i) = fftshift(AW(:,i));            % scale
end



% === define function to return the RHS of Eq. (3.13)
function R = rhs(z, AW, dT, L, S1, S2, gamma, fr, RW, eta, B)
```

```
AT = ifft(AW.*exp(-L*z))./dT;           % time domain field
IT = abs(AT).^2;                        % time domain intensity
ST = AT.^2;                             % time domain square
CA = ifft(S2.*(fr(1)*fft(ST).*dT.*RW(:,1))))./dT;
                                        % time domain cascading term
R1 = -1i.*gamma(:,1).*S1.*fft(conj(AT).*CA).*dT;
                                        % right hand term 1

if eta <eps                             % no XPM
    XPM = 0;
else
    XPM = eta.*abs(gamma(:,1)).*fft(AT.*CA.^2).*dT;
end                                     % frequency domain XPM term

if fr(2) <eps                           % no Raman case
    RS = 0;
else
    RS = fr(2)*ifft((fft(IT).*dT + ...
                eta.*abs(gamma(:,1)).*fft(CA.^2).*dT).*RW(:,2))./dT;
end                                     % Raman scattering

CU = (1-fr(2))*fft(AT.*IT).*dT+B*XPM + fft(AT.*RS).*dT;
R2 = -1i.*gamma(:,2).*S1.*CU;

R = (R1+R2).*exp(L*z);                  % full RHS

% === define function to print ODE integrator status
function status = report(z, ~, flag, zl)
status = 0;
if isempty(flag)
    fprintf('%05.1f %% complete\n', z/zl*100);
end
```

A.4 NWEF Simulation of CQSC in LIS Crystal

A.4.1 Material Dispersion Properties

```
function [k, dk] = LIS_Wave_Vec_Z(omega, mdim)
% ref: Sandrine Fossier, et al., J. Opt. Soc. Am. B 21, 1981-2007 (2004)

format long

c = 0.299792458; % um/fs
tmp = 4*pi^2*c^2;
ndim = length(omega);

a1 = 7.256327;
a2 = 0.15072;
a3 = 0.06823652;
```

```
a4 = 2626.10840;
a5 = 983.0503;

Wave_Vec_z = 'W/C*sqrt(A1 + A2*W^2/(Tmp-A3*W^2) + A4*W^2/(Tmp-A5*W^2))';

kFHz = subs(Wave_Vec_z, ...
            {'A1', 'A2', 'A3', 'A4', 'A5', 'Tmp', 'C', 'W'},...
            {a1, a2, a3, a4, a5, tmp, c, omega});
kSHz = subs(Wave_Vec_z, ...
            {'A1', 'A2', 'A3', 'A4', 'A5', 'Tmp', 'C', 'W'},...
            {a1, a2, a3, a4, a5, tmp, c, 2*omega});

k = struct('fhz', kFHz, 'shz', kSHz);

if (mdim > 0) && (~mod(mdim,1))
    FHz = zeros(mdim,ndim);
    SHz = zeros(mdim,ndim);
    for i = 1:mdim
        DkDw_z = diff(Wave_Vec_z,'W');

        Wave_Vec_z = DkDw_z;

        FHz(i,:) = subs(Wave_Vec_z, ...
                        {'A1', 'A2', 'A3', 'A4', 'A5', 'Tmp', 'C', 'W'},...
                        {a1, a2, a3, a4, a5, tmp, c, omega});
        SHz(i,:) = subs(Wave_Vec_z, ...
                        {'A1', 'A2', 'A3', 'A4', 'A5', 'Tmp', 'C', 'W'},...
                        {a1, a2, a3, a4, a5, tmp, c, 2*omega});

    end
    dk = struct('fhz', FHz, 'shz', SHz);
end
```

A.4.2 Raman Spectrum

```
function [hRw] = HRW(w)

format long

ta1 = 20;
tb1 = 1200;
fR1 = 1;

hRw = fR1*(ta1^2+tb1^2)./(tb1^2-ta1^2.*(w.*tb1-1i).^2);
```

A.4.3 Main Function

```
clear
clc
close all
format long

c = 0.299792458;      % [um/fs]
c0   = 299792458;     % Vacuum speed of light in m/s
mu0  = 4e-7*pi;       % [N/A^2]
eps0 = 1/(c0^2*mu0); % [F/m]

% ---- reference ----
lambda = 2;   z1 = 10000;  FWHM = 100; % fs
I_in = 600e-14; % 1GW/cm^2 = 1e-14 V^2*F/(fs*um^2)
qpm_k = 0;
% ------------------
f = c/lambda;
omega = 2*pi*f;
[k, dk] = LIS_Wave_Vec_Z(omega,2);
n_z   = k.fhz*c/omega;
k_z   = k.fhz;
dk_z  = dk.fhz(1);
ddk_z = dk.fhz(2);

delta_k = k.shz - 2*k.fhz;

Ec  = sqrt(I_in)/sqrt(eps0*1e-6*n_z*c/2); % [V/um]
t0 = FWHM/(2*log(1+2^0.5)); % Guassan: exp(-t^2/T0^2)

% ---- time ----
t_span = 5800; % fs
nt = 2^(ceil(log2(10*t_span*f))); % ---- 10 points for each cycle ----
% nt = 2^16;
dt = t_span/nt;
t  = -t_span/2:dt:t_span/2-dt;

% ---- frequency ----
w_span = 2*pi/dt; % fs^-1
dw = w_span/nt;
w  = -w_span/2:dw:w_span/2-dw;

% ---- physical range ----
lambda_range = [0.45 8];
% ----------------------
omega_range  = sort(2*pi*c./lambda_range);
w1 = find(w >=  omega_range(1), 1,'first');
w2 = find(w <=  omega_range(2), 1, 'last');
w3 = find(w >= -omega_range(2), 1,'first');
w4 = find(w <= -omega_range(1), 1, 'last');
w_left  = w(w3:w4);              w_left_sh  = 2*w_left;
w_right = w(w1:w2);              w_right_sh = 2*w_right;

% ---- wave vector ----
k = LIS_Wave_Vec_Z(w,0);
k_left  = k.fhz(w3:w4);          k_left_sh  = k.shz(w3:w4);
```

```
k_right = k.fhz(w1:w2);          k_right_sh = k.shz(w1:w2);
delta_k_left  = k_left_sh  - 2*k_left  + qpm_k;
delta_k_right = k_right_sh - 2*k_right - qpm_k;
n_left  = k_left*c./w_left;      n_left_sh  = k_left_sh*c./w_left_sh;
n_right = k_right*c./w_right;    n_right_sh = k_right_sh*c./w_right_sh;
k = zeros(1,nt);
k(w3:w4) = k_left;
k(w1:w2) = k_right;

% ---- quadratic nonlinearity ----
d33_left = 15.6e-12*(2/pi)^(qpm_k~=0);
d33_right = 15.6e-12*(2/pi)^(qpm_k~=0);
n2_casc_left  = ...
  -2*d33_left .^2.*w_left ./(c.*n_left .^2.*n_left_sh *eps0*c0.*delta_k_left);
n2_casc_right = ...
  -2*d33_right.^2.*w_right./(c.*n_right.^2.*n_right_sh*eps0*c0.*delta_k_right);

% ----cubic nonlinearity ----
% ----Raman scattering ----
fr = 0.2;
hrw = HRW(w);
c33_left  =  44.44e-22;
c33_right =  44.44e-22;
n2_cubic_left  = 3/4*c33_left ./(c0*eps0.*n_left.^2);
n2_cubic_right = 3/4*c33_right./(c0*eps0.*n_right.^2);

gamma = zeros(2,nt);
% ---- 2*deff*w^2/(2*c^2*k) ----
gamma(1,w1:w2) = 2*d33_right.*w_right.^2./(2*c^2.*k_right)*1e6;
gamma(1,w3:w4) = 2*d33_left .*w_left .^2./(2*c^2.*k_left )*1e6;
% ---- c33*w^2/(2*c^2*k) ----
gamma(2,w1:w2) = c33_right.*w_right.^2./(2*c^2.*k_right)*1e12;
gamma(2,w3:w4) = c33_left .*w_left .^2./(2*c^2.*k_left )*1e12;

E = Ec*sech(t/t0).*cos(omega*t);
height = Ec*sum(sech(t/t0))*dt/2;

if qpm_k~=0
    dz = 2*pi/qpm_k/2;
else
    dz = pi/delta_k/2;
end
nz = ceil(zl/dz);
z = 0:dz:dz*nz;

LD = t0^2./abs(ddk_z);
N_right = sqrt(LD*I_in*1e27*w_right./c.*(abs(n2_casc_right) - ...
     (1-fr)*n2_cubic_right));
N = interp1(w_right, N_right, omega);

fprintf('Soliton order : %.2f\n', N);
fprintf('Soliton length: %.2f mm\n', pi/2*LD/1000);
fprintf('Crystal length: %.2f mm\n', zl/1000);
fprintf('Total steps : %d\n', nz+1);
```

```
tic;
[EV, ET, EW, ~] = NWEF_Type0(t.', z, omega, omega_range, E.', 0, k.', ...
     gamma.', fr, hrw.', dk_z^-1, qpm_k);
toc;
wl = linspace(lambda_range(1),lambda_range(2),w2-w1+1);
w_redef = 2*pi*c./wl;
[Z,W]  = meshgrid(z,w_right);
[~,WI] = meshgrid(z,w_redef);
EWL = interp2(Z,W,EW,Z,WI,'cubic');

%load MyColormaps
fig1 = figure('Position',[50 100 1000 400]);
axes1 = axes('Parent', fig1,...
             'Position',[0.07 0.15 0.87 0.80],...
             'FontWeight','bold',...
             'FontSize',14,...
             'FontName','Times New Roman',...
             'CLim',[-60 0],...
             'Tick','out');
xlim(axes1,[lambda_range(1) lambda_range(2)]*1000);
ylim(axes1,[0 max(z)/1000]);
box(axes1,'off');
hold(axes1,'all');

img1 = image(wl*1000, z.'/1000, 10*log10(abs(EWL.'./height).^2),...
               'Parent',axes1,...
               'CDataMapping','scaled');
set(fig1,'Colormap',jet);
colorbar('Peer', axes1,...
         [0.95 0.15 0.01 0.80],...
         'FontSize', 14,...
         'FontName', 'Times New Roman',...
         'XColor', [0 0 0],...
         'YColor', [0 0 0]);
xlabel('Wavelength (nm)');ylabel('Length (mm)');

fig2 = figure('Position',[50 500 1000 400]);
axes2 = axes('Parent', fig2,...
             'Position',[0.07 0.15 0.87 0.80],...
             'FontWeight','bold',...
             'FontSize',14,...
             'FontName','Times New Roman',...
             'CLim',[-60 0],...
             'Tick','out');
xlim(axes2,[omega_range(1) omega_range(2)]);
ylim(axes2,[0 max(z)/1000]);
box(axes2,'off');
hold(axes2,'all');

img2 = image(w_right, z.'/1000, 10*log10(abs(EW.'./height).^2),...
               'Parent',axes2,...
               'CDataMapping','scaled');
set(fig2,'Colormap',jet);
```

```
colorbar('Peer', axes2,...
         [0.95 0.15 0.01 0.80],...
         'FontSize', 14,...
         'FontName', 'Times New Roman',...
         'XColor', [0 0 0],...
         'YColor', [0 0 0]);
xlabel('frequency (rad/fs)');ylabel('Length (mm)');

fig3 = figure('Position',[1100 100 400 400]);
axes3 = axes('Parent', fig3,...
             'Position',[0.15 0.15 0.75 0.80],...
             'FontWeight','bold',...
             'FontSize',14,...
             'FontName','Times New Roman',...
             'CLim',[0 max(max(abs(EV).^2))./Ec^2],...
             'Tick','out');
xlim(axes3,[-500 500]);
ylim(axes3,[0 max(z)/1000]);
box(axes3,'off');
hold(axes3,'all');

img3 = image(t, z.'/1000, abs(EV.').^2./Ec^2,...
               'Parent',axes3,...
               'CDataMapping','scaled');
set(fig3,'Colormap',pulse);
colorbar('Peer', axes3,...
         [0.91 0.15 0.02 0.80],...
         'FontSize', 14,...
         'FontName', 'Times New Roman',...
         'XColor', [0 0 0],...
         'YColor', [0 0 0]);
xlabel('Frequency (rad/fs)');ylabel('Length (mm)');
```

Appendix B

Crystal Susceptibilities with Light Deviated from Principal Axes

Here we briefly introduce the calculation of crystal linear/nonlinear susceptibilities when light is propagated with deviation from principal axes [1]. Frame (x, y, z) is assigned to mark the principal axes, i.e. the optic axis/axes of the crystal, while frame (x', y', z') marks the light propagation, in which axis z' indicates the light propagation direction and axes x' and y' are polarization directions. The transition between (x, y, z) and (x', y', z') could be normalized as a two-angle rotation (φ, θ) where angle φ marks the frame rotation with respect to axis z and θ is the angle between z and z', see Fig. B.1.

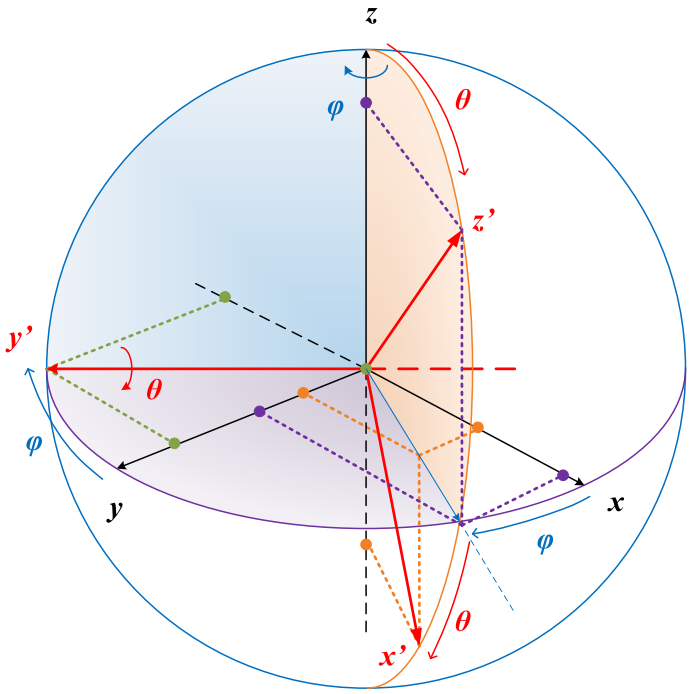

Fig. B.1: normalized two-angle rotation from crystal principal axes (x, y, z) to light propagation frame (x', y', z').

Therefore, the transition between the two frames is:

$$\begin{bmatrix} x' \\ y' \\ z' \end{bmatrix} = \mathscr{R} \begin{bmatrix} x \\ y \\ z \end{bmatrix}, \quad \begin{bmatrix} x \\ y \\ z \end{bmatrix} = \mathscr{R}^{-1} \begin{bmatrix} x' \\ y' \\ z' \end{bmatrix} \tag{B.1}$$

where the transition matrix is:

$$\begin{aligned}
\mathscr{R} &= \begin{bmatrix} r_{11} & r_{12} & r_{13} \\ r_{21} & r_{22} & r_{23} \\ r_{31} & r_{32} & r_{33} \end{bmatrix} = \begin{bmatrix} \cos\varphi\cos\theta & \sin\varphi\cos\theta & -\sin\theta \\ -\sin\varphi & \cos\varphi & 0 \\ \cos\varphi\sin\theta & \sin\varphi\sin\theta & \cos\theta \end{bmatrix} \\
\mathscr{R}^{-1} &= \begin{bmatrix} r_{11}^{-1} & r_{12}^{-1} & r_{13}^{-1} \\ r_{21}^{-1} & r_{22}^{-1} & r_{23}^{-1} \\ r_{31}^{-1} & r_{32}^{-1} & r_{33}^{-1} \end{bmatrix} = \begin{bmatrix} \cos\theta\cos\varphi & -\sin\varphi & \sin\theta\cos\varphi \\ \cos\theta\sin\varphi & \cos\varphi & \sin\theta\sin\varphi \\ -\sin\theta & 0 & \cos\theta \end{bmatrix}
\end{aligned} \tag{B.2}$$

Since $\mathscr{R}^T = \mathscr{R}^{-1}$ (i.e. $r_{nm} = r_{mn}^{-1}$), matrix $\mathscr{R}$ is orthogonal.

In the principal frame, crystal linear/nonlinear susceptibilities are predetermined as material fundaments. For example, fundamental permittivities reflecting the refractive indices of an uniaxial crystal is defined as:

$$\tilde{\boldsymbol{\varepsilon}}_{\boldsymbol{r}} = 1 + \tilde{\boldsymbol{\chi}}^{(1)} = \begin{bmatrix} \tilde{\varepsilon}_{x;x} & 0 & 0 \\ 0 & \tilde{\varepsilon}_{y;y} & 0 \\ 0 & 0 & \tilde{\varepsilon}_{z;z} \end{bmatrix} \tag{B.3}$$

where $\tilde{\boldsymbol{\chi}}^{(1)}$ includes linear susceptibilities.

Without nonlinearities, the electric flux density is written as $\tilde{\mathbf{D}} = \varepsilon_0 \tilde{\boldsymbol{\varepsilon}}_{\boldsymbol{r}} \tilde{\mathbf{E}}$. In the propagation frame, we have:

$$\tilde{\mathbf{D}}' = \mathscr{R}\tilde{\mathbf{D}} = \varepsilon_0 \mathscr{R}\tilde{\boldsymbol{\varepsilon}}_{\boldsymbol{r}}\mathscr{R}^{-1}\tilde{\mathbf{E}}' = \varepsilon_0(\mathscr{R}\tilde{\boldsymbol{\varepsilon}}_{\boldsymbol{r}}\mathscr{R}^T)\tilde{\mathbf{E}}' \tag{B.4}$$

Therefore the transited permittivity matrix is $\tilde{\boldsymbol{\varepsilon}}'_{\boldsymbol{r}} = \mathscr{R}\tilde{\boldsymbol{\varepsilon}}_{\boldsymbol{r}}\mathscr{R}^T$.

For tetragonal, trigonal and hexagonal crystals which have $\tilde{\varepsilon}_{x;x} = \tilde{\varepsilon}_{y;y}$, the transited permittivity matrix is expanded as:

$$\tilde{\varepsilon}'_r = \begin{bmatrix} \tilde{\varepsilon}_{x;x}\cos^2\theta + \tilde{\varepsilon}_{z;z}\sin^2\theta & 0 & (\tilde{\varepsilon}_{x;x} - \tilde{\varepsilon}_{z;z})\cos\theta\sin\theta \\ 0 & \tilde{\varepsilon}_{x;x} & 0 \\ (\tilde{\varepsilon}_{x;x} - \tilde{\varepsilon}_{z;z})\cos\theta\sin\theta & 0 & \tilde{\varepsilon}_{x;x}\sin^2\theta + \tilde{\varepsilon}_{z;z}\cos^2\theta \end{bmatrix} \tag{B.5}$$

Since z' is the propagation direction, $\tilde{D}'_z = 0$, we have:

$$\tilde{E}'_z = -\frac{(\tilde{\varepsilon}_{x;x} - \tilde{\varepsilon}_{z;z})\cos\theta\sin\theta}{\tilde{\varepsilon}_{x;x}\sin^2\theta + \tilde{\varepsilon}_{z;z}\cos^2\theta}\tilde{E}'_x \tag{B.6}$$

Hence:

$$\begin{aligned}
\tilde{D}'_x &= \tilde{\varepsilon}_0 \frac{\tilde{\varepsilon}_{x;x}\tilde{\varepsilon}_{z;z}}{\tilde{\varepsilon}_{x;x}\sin^2\theta + \tilde{\varepsilon}_{z;z}\cos^2\theta}\tilde{E}'_x \\
\tilde{D}'_y &= \tilde{\varepsilon}_0\tilde{\varepsilon}_{x;x}\tilde{E}'_y
\end{aligned} \tag{B.7}$$

The light fraction that is polarized along the axis x' is then defined as extraordinary light where the corresponding refractive index is dependent on the angle θ:

$$n_e \triangleq \sqrt{\tilde{\varepsilon}'_{x;x}} = \sqrt{\frac{\tilde{\varepsilon}_{x;x}\tilde{\varepsilon}_{z;z}}{\tilde{\varepsilon}_{x;x}\sin^2\theta + \tilde{\varepsilon}_{z;z}\cos^2\theta}} \tag{B.8}$$

while the y' polarized light fraction is ordinary light where the refractive index is angle independent, i.e. $n_o = \sqrt{\tilde{\varepsilon}'_{y;y}} = \sqrt{\tilde{\varepsilon}_{x;x}}$.

Now we look into the quadratic nonlinearity. The quadratic nonlinear induced polarization in the propagation frame is:

$$\tilde{\mathbf{P}}'^{(2)} = \mathscr{R}\tilde{\mathbf{P}}^{(2)} = \mathscr{R}\varepsilon_0\tilde{\boldsymbol{\chi}}^{(2)}F[\mathbf{EE}] = \varepsilon_0(\mathscr{R}\tilde{\boldsymbol{\chi}}^{(2)}\mathscr{D}^{-1})F[\mathbf{E}'\mathbf{E}'] \tag{B.9}$$

where $\tilde{\boldsymbol{\chi}}^{(2)}$ is the matrix of quadratic nonlinear susceptibilities, which is usually given as the "**d**-tensor", i.e.: (where the Kleinman law are applied)

$$\begin{aligned}\tilde{\boldsymbol{\chi}}^{(2)} &= \begin{bmatrix} \tilde{\chi}^{(2)}_{x;xx} & \tilde{\chi}^{(2)}_{x;yy} & \tilde{\chi}^{(2)}_{x;zz} & \tilde{\chi}^{(2)}_{x;yz} & \tilde{\chi}^{(2)}_{x;xz} & \tilde{\chi}^{(2)}_{x;xy} \\ \tilde{\chi}^{(2)}_{y;xx} & \tilde{\chi}^{(2)}_{y;yy} & \tilde{\chi}^{(2)}_{y;zz} & \tilde{\chi}^{(2)}_{y;yz} & \tilde{\chi}^{(2)}_{y;xz} & \tilde{\chi}^{(2)}_{y;xy} \\ \tilde{\chi}^{(2)}_{z;xx} & \tilde{\chi}^{(2)}_{z;yy} & \tilde{\chi}^{(2)}_{z;zz} & \tilde{\chi}^{(2)}_{z;yz} & \tilde{\chi}^{(2)}_{z;xz} & \tilde{\chi}^{(2)}_{z;xy} \end{bmatrix} \\ &= 2\begin{bmatrix} d_{11} & d_{12} & d_{13} & 2d_{14} & 2d_{15} & 2d_{16} \\ d_{21} & d_{22} & d_{23} & 2d_{24} & 2d_{25} & 2d_{26} \\ d_{31} & d_{32} & d_{33} & 2d_{34} & 2d_{35} & 2d_{36} \end{bmatrix}\end{aligned} \tag{B.10}$$

where:

$$\begin{aligned}\mathbf{EE} &= [\ E_xE_x \quad E_yE_y \quad E_zE_z \quad E_yE_z \quad E_xE_z \quad E_xE_y\ ]^T \\ \mathbf{E}'\mathbf{E}' &= [\ E'_xE'_x \quad E'_yE'_y \quad E'_zE'_z \quad E'_yE'_z \quad E'_xE'_z \quad E'_xE'_y\ ]^T\end{aligned} \tag{B.11}$$

For each element d_{mn}, the first subscript, $m = 1, 2, 3$, indicates the target electric field component, E_x, E_y, E_z, while the second subscript, $n = 1, \cdots, 6$, indicates the combination type of two contributed electric field components in the quadratic nonlinear process. The pre-factor 2 in front of the d matrix is the consequence of historical conversions. Note that compared to the definition in the textbook, some elements in d matrix have extra pre-factors of 2, which is actually shifted from the vector **EE** which used to be defined as:

$$\mathbf{EE} = [\ E_xE_x \quad E_yE_y \quad E_zE_z \quad 2E_yE_z \quad 2E_xE_z \quad 2E_xE_y\ ]^T$$

Since we have $\mathbf{E} = \mathscr{R}^{-1}\mathbf{E}'$, matrix $\mathscr{D}^{-1}$ can be easily obtained as:

$$\mathscr{D}^{-1}[\mathbf{E}'\mathbf{E}'] = \begin{cases} \sum\limits_{k,l=1,2,3} r_{1k}^{-1} r_{1l}^{-1} E'_k E'_l \\ \sum\limits_{k,l=1,2,3} r_{2k}^{-1} r_{2l}^{-1} E'_k E'_l \\ \sum\limits_{k,l=1,2,3} r_{3k}^{-1} r_{3l}^{-1} E'_k E'_l \\ \sum\limits_{k,l=1,2,3} r_{2k}^{-1} r_{3l}^{-1} E'_k E'_l \\ \sum\limits_{k,l=1,2,3} r_{1k}^{-1} r_{3l}^{-1} E'_k E'_l \\ \sum\limits_{k,l=1,2,3} r_{1k}^{-1} r_{2l}^{-1} E'_k E'_l \end{cases} \tag{B.12}$$

Therefore, the quadratic nonlinear susceptibility matrix in the propagation frame is:

$$\tilde{\boldsymbol{\chi}}'^{(2)} = \mathscr{R}\tilde{\boldsymbol{\chi}}^{(2)}\mathscr{D}^{-1} \tag{B.13}$$

which can be calculated by *Mathematica*. For example, trigonal crystals within group $3m$ have following d matrix:

$$\begin{bmatrix} 0 & 0 & 0 & 0 & 2d_{15} & -2d_{22} \\ -d_{22} & d_{22} & 0 & 2d_{15} & 0 & 0 \\ d_{31} & d_{31} & d_{33} & 0 & 0 & 0 \end{bmatrix}, \; d_{31} = d_{15} \tag{B.14}$$

Therefore, we have:

$$d'_{e;oo} \triangleq \frac{1}{2}\tilde{\chi}'^{(2)}_{y;xx} = -d_{31}\sin\theta + d_{22}\cos\theta\sin 3\varphi \tag{B.15}$$

and,

$$d'_{e;ee} \triangleq \frac{1}{2}\tilde{\chi}'^{(2)}_{x;xx} = -3d_{31}\cos^2\theta\sin\theta - d_{33}\sin^3\theta - d_{22}\cos^3\theta\sin 3\varphi \tag{B.16}$$

Analogously, the cubic nonlinear induced polarization in the propagation frame is:

$$\tilde{\mathbf{P}}'^{(3)} = \varepsilon_0(\mathscr{R}\tilde{\boldsymbol{\chi}}^{(3)}\mathscr{C}^{-1})F[\mathbf{E}'\mathbf{E}'\mathbf{E}'] \tag{B.17}$$

where the material cubic nonlinear susceptibility matrix is $\tilde{\boldsymbol{\chi}}^{(3)} = \mathbf{C}_{[3\times 10]}$: (with the Kleinman law been applied)

$$\begin{bmatrix} c_{11} & c_{12} & c_{13} & 3c_{14} & 3c_{15} & 3c_{16} & 3c_{17} & 3c_{18} & 3c_{19} & 6c_{110} \\ c_{21} & c_{22} & c_{23} & 3c_{24} & 3c_{25} & 3c_{26} & 3c_{27} & 3c_{28} & 3c_{29} & 6c_{210} \\ c_{31} & c_{32} & c_{33} & 3c_{34} & 3c_{35} & 3c_{36} & 3c_{37} & 3c_{38} & 3c_{39} & 6c_{310} \end{bmatrix} \tag{B.18}$$

For each element, c_{mn}, the first subscript, $m = 1, 2, 3$, represents the target electric field component, i.e. E_x, E_y, E_z, and the second subscript, $n = 1, \cdots, 10$, marks the type of combination of three contributed electric field components, i.e. xxx, yyy, zzz, xxy, xxz, yyx, yyz, zzx, zzy, xyz, respectively. For example:

$$c_{18} = \tilde{\chi}^{(3)}_{x;zzx} = \tilde{\chi}^{(3)}_{x;xzz} = \tilde{\chi}^{(3)}_{x;zxz} = \tilde{\chi}^{(3)}_{z;zxx} = c_{35} \tag{B.19}$$

Pre-factors in such the C matrix are shifted from the vector **EEE**, which is:

$$\begin{aligned}\mathbf{EEE} = \Big[\; & E_xE_xE_x \quad E_yE_yE_y \quad E_zE_zE_z \quad E_xE_xE_y \quad E_xE_xE_z \\ & E_yE_yE_x \quad E_yE_yE_z \quad E_zE_zE_x \quad E_zE_zE_y \quad E_xE_yE_z \; \Big]^T\end{aligned} \tag{B.20}$$

Correspondingly, we have:

$$\begin{aligned}\mathbf{E'E'E'} = \Big[\; & E'_xE'_xE'_x \quad E'_yE'_yE'_y \quad E'_zE'_zE'_z \quad E'_xE'_xE'_y \quad E'_xE'_xE'_z \\ & E'_yE'_yE'_x \quad E'_yE'_yE'_z \quad E'_zE'_zE'_x \quad E'_zE'_zE'_y \quad E'_xE'_yE'_z \; \Big]^T\end{aligned} \tag{B.21}$$

The transition matrix $\mathscr{C}^{-1}$ is obtained as:

$$\mathscr{C}^{-1}[\mathbf{E'E'E'}] = \begin{cases} \sum\limits_{k,l,s=1,2,3} r^{-1}_{1k} r^{-1}_{1l} r^{-1}_{1s} E'_k E'_l E'_s \\ \sum\limits_{k,l,s=1,2,3} r^{-1}_{2k} r^{-1}_{2l} r^{-1}_{2s} E'_k E'_l E'_s \\ \sum\limits_{k,l,s=1,2,3} r^{-1}_{3k} r^{-1}_{3l} r^{-1}_{3s} E'_k E'_l E'_s \\ \sum\limits_{k,l,s=1,2,3} r^{-1}_{1k} r^{-1}_{1l} r^{-1}_{2s} E'_k E'_l E'_s \\ \sum\limits_{k,l,s=1,2,3} r^{-1}_{1k} r^{-1}_{1l} r^{-1}_{3s} E'_k E'_l E'_s \\ \sum\limits_{k,l,s=1,2,3} r^{-1}_{2k} r^{-1}_{2l} r^{-1}_{1s} E'_k E'_l E'_s \\ \sum\limits_{k,l,s=1,2,3} r^{-1}_{2k} r^{-1}_{2l} r^{-1}_{3s} E'_k E'_l E'_s \\ \sum\limits_{k,l,s=1,2,3} r^{-1}_{3k} r^{-1}_{3l} r^{-1}_{1s} E'_k E'_l E'_s \\ \sum\limits_{k,l,s=1,2,3} r^{-1}_{3k} r^{-1}_{3l} r^{-1}_{2s} E'_k E'_l E'_s \\ \sum\limits_{k,l,s=1,2,3} r^{-1}_{1k} r^{-1}_{2l} r^{-1}_{3s} E'_k E'_l E'_s \end{cases} \tag{B.22}$$

Hence, the effective cubic nonlinear susceptibility matrix in the propagation frame is:

$$\tilde{\boldsymbol{\chi}}'^{(3)} = \mathscr{R}\tilde{\boldsymbol{\chi}}^{(3)}\mathscr{C}^{-1} \tag{B.23}$$

Trigonal crystals within group $3m$ have **C** matrix:

$$\begin{bmatrix} c_{11} & 0 & 0 & 0 & 3c_{15} & c_{11} & -3c_{15} & 3c_{18} & 0 & 0 \\ 0 & c_{11} & 0 & c_{11} & 0 & 0 & 0 & 0 & 3c_{18} & -6c_{15} \\ c_{15} & 0 & c_{33} & 0 & 3c_{18} & -3c_{15} & 3c_{18} & 0 & 0 & 0 \end{bmatrix} \tag{B.24}$$

Therefore, we have:

$$\begin{aligned} \tilde{\chi}^{(3)}_{e;eee} &\triangleq \tilde{\chi}'^{(3)}_{x;xxx} \\ &= c_{11}\cos^4\theta - 4c_{15}\cos^3\theta\sin\theta\cos 3\varphi + 6c_{18}\cos^2\theta\sin^2\theta + c_{33}\sin^4\theta \end{aligned} \tag{B.25}$$

$$\tilde{\chi}^{(3)}_{o;ooo} \triangleq \tilde{\chi}'^{(3)}_{y;yyy} \equiv c_{11} \tag{B.26}$$

and,

$$\begin{aligned} \tilde{\chi}^{(3)}_{o;eeo} = \tilde{\chi}^{(3)}_{e;ooe} \triangleq \tilde{\chi}'^{(3)}_{x;yyx} = \tilde{\chi}'^{(3)}_{y;xxy} \\ = c_{11}\cos^2\theta + 3c_{15}\sin 2\theta\cos 3\varphi + 3c_{18}\sin^2\theta \end{aligned} \tag{B.27}$$

Bibliography

[1] P. Butcher and D. Cotter, *The Elements of Nonlinear Optics*, Cambridge Studies in Modern Optics (Cambridge University Press, 1991).

Appendix C

Understanding Soliton Spectral Tunneling as A Coupling Effect

C.1 Introduction

Dispersive waves (DWs), also known as soliton induced optical Cherenkov radiations (OCRs) [1], are generated when temporal solitons are perturbed by higher-order dispersion [2]. This phenomenon was experimentally verified soon after its proposal [3–5]. Physically, DW is a resonant wave having phase matching (PM) to the launched soliton. The spectral position of such a wave can be well predicted through a PM topology (showing resonant wavelengths as a function of the soliton wavelength) [6]. DWs play an important role in the attractive octave-spanning supercontinuum generation (SCG) in fiber structures as they dominate the blue-shifted edge of the spectrum while the Raman induced soliton self-frequency shift (SSFS) leads to the red-shifted edge [7]. Usually, soliton induced DWs are generated in normal group velocity dispersion (GVD) regions which are opposite to the solitons [8,9], and they also have different group velocity (GV) than the solitons.

However, by properly tailoring the dispersion profile, such DWs can also be turned into soliton waves. One exact case is the so-called soliton spectral tunneling (SST) effect which was proposed and investigated [10–14] as a soliton spectral switching phenomenon. Fundamentally, SST is driven by the Raman induced SSFS to continuously shed off energy to the DW, and it also requires a potential barrier in the GVD profile [10], [11], [14] so that both the launched soliton and the generated DW have the same sign of GVD and the DW finally forms another soliton wave. A typical GVD barrier is a normal GVD region sandwiched by two anomalous ones, which is realizable in photonic crystal fibers (PCFs), with the waveguide dispersion reducing the material dispersion and forming multiple zero-dispersion wavelengths (ZDWs). Poletti et al. designed an index-guiding holey fiber to form the GVD barrier which can be tuned over a wide wavelength span and has potentials for SST [15]. Manili et al. reported their DW generation experiments in a dual concentric core microstructured fiber which has three ZDWs [16]. But unfortunately the SST effect was not observed as the GVD barrier was so strong that the transferred wave could not pass through to form a soliton wave. Moreover, recent investigations on the SST effect [17,18] showed that along with the above mentioned PM condition, GV matching between the launched and switched solitons is another significant premise for decent soliton switching with high efficiency and broad bandwidth.

In this appendix chapter, we propose an idea that such a GV-matching DW generation as well as the SST effect can be generally understood as a

spectral soliton coupling from an initial state to its eigenstate. Analogous to a spatial waveguide in which eigenmodes are supported under a certain phase profile (determined by the spatial refractive index profile), for fundamental temporal solitons, an eigenstate is also supported under a dispersive phase profile determined by the wave number profile and the soliton phase changes induced by both the dispersion and the nonlinearity are counterbalanced. DW generation and SST are usually invoked by launching a local soliton state but not the eigenstate, therefore spectral soliton coupling between this initial state and the eigenstate can occur, in which the local soliton will shed off energy to other wavelength positions. A GV-matching condition is essential to tell whether the transferred wave is solitary or dispersive as it defines the dispersive wave number profile. If the transferred wave is GV-matched to the launched soliton, the wave number profile performs like a spectral coupler structure and the transferred wave can form a soliton state, while when GV-mismatched, the profile is a leaking structure and the transferred wave performs as leakage from the launched soliton, namely forming linear dispersive waves.

C.2 Soliton Eigenstate and Coupling Effect

We begin with the demonstration of the soliton eigenstate. The nonlinear wave equation in frequency domain (NWEF) [19,20] is chosen as the numerical model as it focuses on the spectrum of the electric field. With only the dispersion and the cubic phase modulation (self-phase modulation (SPM) and cross-phase modulation (XPM)) terms included, NWEF is written as:

$$\frac{\partial}{\partial z}\tilde{E} + i\beta\tilde{E} + i\gamma F[|E|^2 E] = 0 \tag{C.1}$$

where $\tilde{E}$ is the electric field written in frequency domain, β refers to the wave number profile, $\gamma(\omega) = \frac{\omega}{c} n_2 / A_{\text{eff}}(\omega)$ is the frequency-dependent nonlinear coefficient in which the pulse self-steepening is automatically included. F indicates the Fourier transform. The dispersive phase profile is determined with the initial wave number β_0 and the global GV $v_{g,0}$ eliminated from the physical wave number, i.e. $\beta_{\text{eig}}(\omega) = \beta(\omega) - \beta_0 - \omega \cdot v_{g,0}^{-1}$. Shown in Fig. C.2(a), a coupler-like wave number profile is demonstrated to support a soliton eigenstate which consists of two spectral peaks corresponding to coupler channels.

If only a one-peak hyperbolic secant shape (sech-shape) soliton, corresponding to one channel of the wave number coupler, is launched, soliton spectral

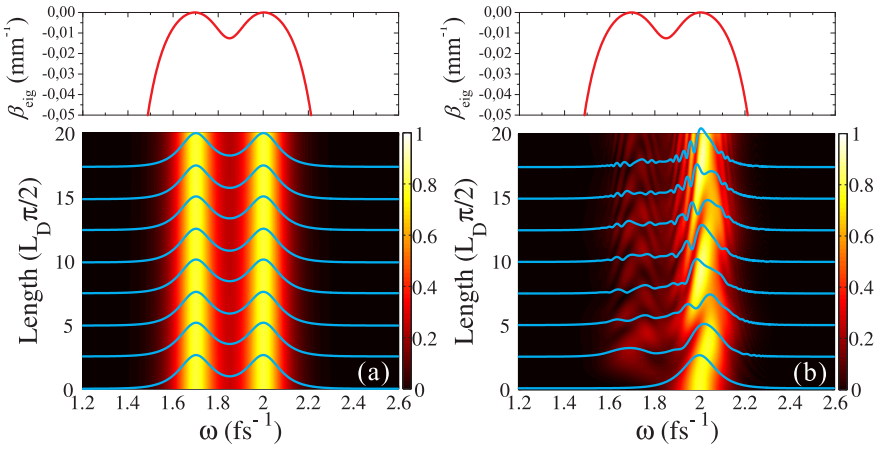

Fig. C.1: (a) soliton eigenstate of a coupler-like wave number profile. Note that the wave number profile has an explicit expression with respect to the soliton eigenstate according to Eq.(C.1);(b) soliton coupling from the initial state towards the eigenstate. The launched soliton is sech-shape, the soliton order is set to unity, $T_0 = 10$ fs (FWHM = 17.63 fs). Spectral evolutions are linear scaled. Y-axes in spectrum evolutions are scaled as soliton length defined as $\frac{\pi}{2}L_{\mathrm{D}}$, L_{D} is dispersion length. n_2 and A_{eff} are assumed to be dispersionless here.

coupling is supposed to be observed as shown in Fig. C.2(b): the soliton sheds off energy into the adjacent channel and forms another wave. Meanwhile, the launched soliton itself will experience a spectral recoil effect [1, 21] away from the coupling. The energy coupled out will also be coupled back since the transferred wave is GV-matched to the launched soliton. Therefore the launched soliton will be pulled back to its original position and invokes the coupling over again. The transferred wave here is formed due to the DW PM condition, but it is not a DW but actually a soliton wave which travels together with the launched soliton (GV-matching), it is fed by the launched soliton but unfortunately the energy is low due to the recoil effect.

Including material Raman effects (not included in Eq.(1)) which always accompany the self-action of high-power femtosecond pulses in a variety of media [22,23], SST effect is observed as shown in Fig. C.2(a). Since the Raman response induces SSFS which is always red-shifted and could balance the recoil effect, the launched soliton can be kept at its position and the soliton coupling

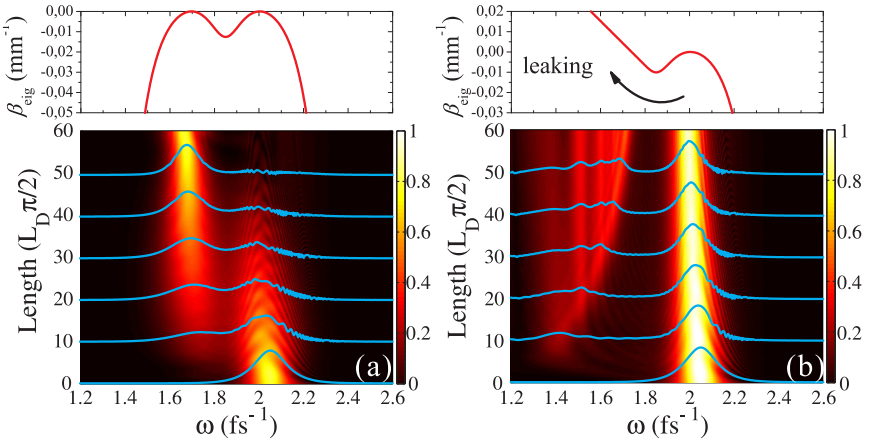

Fig. C.2: (a) SST effect with extra 20% material Raman effects. The Raman spectral response is chosen from Ref. [8]; (b) soliton leaking in a leaking wave number profile, commonly known as the DW generation.

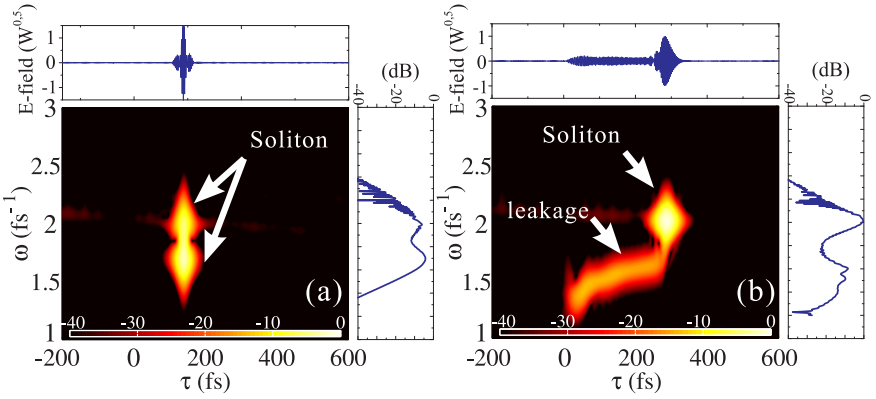

Fig. C.3: (a) and (b) are XFROG patterns of Fig. C.2(a) and Fig. C.2(b) at half propagation distance, with the corresponding spectra and profiles of the electric field; Gate function in the XFROG pattern has a hyperbolic secant shape with $T_0 = 10$ fs. XFROG patterns are logarithmic scaled.

continuously occurs until it is fully coupled into the adjacent channel to form a new soliton. Afterwards, the new soliton will also experience the Raman induced SSFS, which means the back coupling are greatly suppressed since the soliton will be red-shifted away from the coupling. The XFROG pattern of

the SST also shows that the generated soliton is always GV-matched to the launched one, see Fig. C.2(a).

However, in a leaking structure of the dispersive wave number profile where the transferred wave is GV-mismatched to the launched soliton, SST will not occur, see Fig. C.2(b). In the XFROG pattern, waves are gradually radiated as the leakage from the launched soliton, leaving a long tail in the pattern, see Fig. C.2(b).

In fact, the GV-matching condition helps turning the commonly-known DW PM condition into a soliton PM condition. The PM condition of the DW generated at ω_d can be written as:

$$\beta(\omega_d) = \beta_{sol,\omega_s}(\omega_d) \tag{C.2}$$

where $\beta_{sol,\omega_s}(\omega) = \beta(\omega_s) + (\omega - \omega_s)v_{g,s}^{-1} + q_s$ determines the non-dispersive soliton phase with spectrum centered at ω_s, q_s is the soliton wave number and, for fundamental solitons, its contribution is minimal and can be ignored. Therefore, the above equation can be expanded as:

$$\beta(\omega_d) + (\omega - \omega_d) \cdot v_{g,s}^{-1} = \beta(\omega_s) + (\omega - \omega_s)v_{g,s}^{-1} \tag{C.3}$$

With a GV-matching condition, $v_{g,d} = v_{g,s}$, the above equation finally becomes $\beta_{sol,\omega_s}(\omega) = \beta_{sol,\omega_d}(\omega)$, implying the phase matching within the whole frequency domain between two solitons located at ω_s and ω_d. Actually, a symmetric coupler-like wave number profile is exactly corresponding to such a soliton PM condition, with both the DW PM and the GV-matching conditions fulfilled between the launched and transferred solitons.

C.3 Examples in Photonic Crystal Fibers

In practice, PCFs with designed pitch size Δ and hole size d can achieve flexible dispersion profiles with multiple controlled ZDWs. For example, in Fig. C.4, a solid-core index-guiding PCF with a triangular air-hole pattern in the cladding can form a concave-like dispersion profile with 3 ZDWs. Such a dispersion profile is actually produced by the mode coupling between the core and the air-hole cladding around a resonant wavelength.

The wave number profile of such a PCF structure is plotted in Fig. C.5, by eliminating a global β_0 and $v_{g,0}$, showing a coupler-like profile, with two peaks located at 1.52 μm and 1.85 μm. Under such a profile, a sech-shape soliton

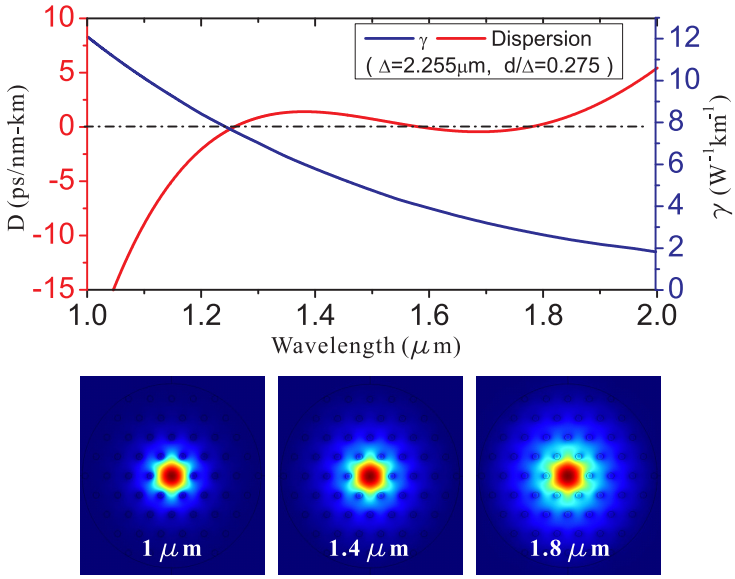

Fig. C.4: Solid-core index guiding PCF's dispersion and effective nonlinear coefficient γ versus wavelength, estimated by means of Comsol software. The inserts are the mode field distribution corresponding to different wavelengths. Core diameter can be estimated as $2\Delta - d = 3.89$ μm.

centered at 1.4 μm is launched, which is actually slightly detuned from the short-wavelength coupler peak. Hence, during the propagation, the launched soliton will start with the Raman induced SSFS, red-shifting towards the first coupler peak where the coupling is invoked. Then, strong soliton coupling occurs with most of the energy transferred into the second coupler channel, shown by the full NWEF model [19] in Fig. C.5(a). The XFROG pattern in Fig. C.5(c) again proves the GV-matching between the launched and transferred solitons. The proportion of the soliton energy transfer is around 60%, lower than the ideal SST because the nonlinear coefficient γ has a reduction in long wavelengths due to an increase in the effective mode area.

With a different pitch size, the wave number profile shows a leaking structure. Therefore, soliton leaking occurs instead of coupling, see Fig. C.5(b). Although from the spectral evolution the transferred waves still have strong peaks, they are actually not soliton waves but just leakage-like DWs, proved by the XFROG pattern in Fig. C.5(d).

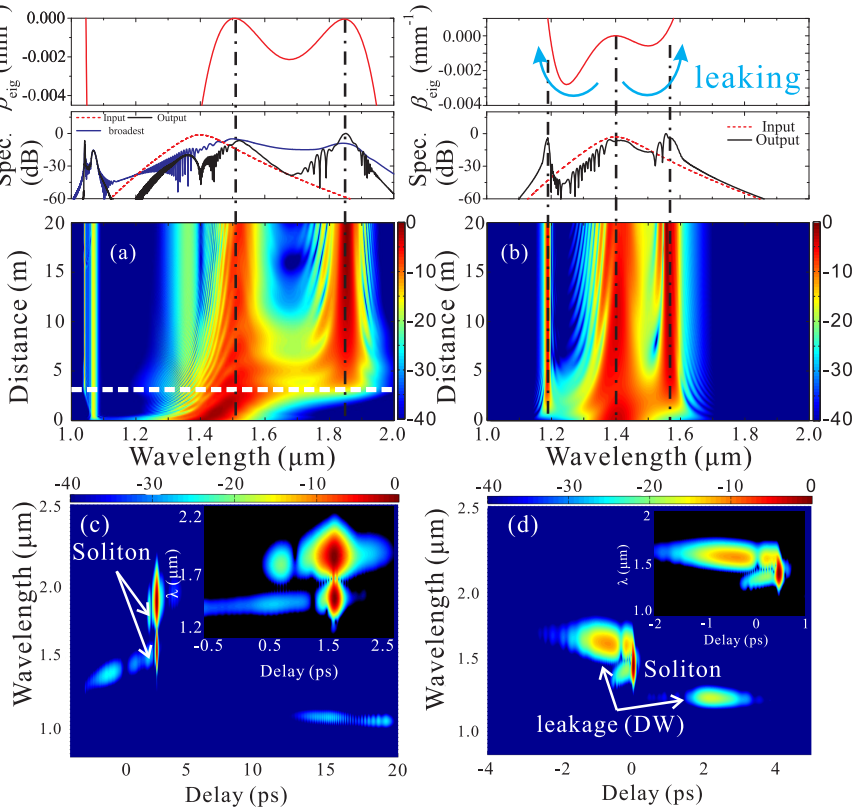

Fig. C.5: Full NWEF simulations on the spectral evolutions of a 25 fs (FWHM) single sech-shape soliton centered at 1.4 μm under the coupler-like and leaking phase profiles: (a) coupler-like structure with $\Delta = 2.255$ μm and (b) leaking structure with $\Delta = 2.235$ μm. The input, output spectra of both cases and broadest spectrum during the SST (position marked by white dashed line) are shown. The input soliton pulse has a peak power 380 W, soliton length $\frac{\pi}{2}L_{\mathrm{D}}$ is 0.22 m, the material Kerr nonlinearity is $n_2 = 2.6 \times 10^{-20}$ m^2/W, Raman fraction is 24.5%. (c) and (d) XFROG pattern of (a) and (b) at a propagation length of 20 m. The gate function in XFROG pattern also has a FWHM = 25 fs. Spectral evolutions and XFROG patterns are all logarithmic scaled.

The soliton coupling effect as well as the soliton state of the transferred wave is also demonstrated through the temporal profile of the pulses, see Fig. C.6. Shown in Fig. C.6(a, b), the soliton pulse in the first channel (1.52 μm)

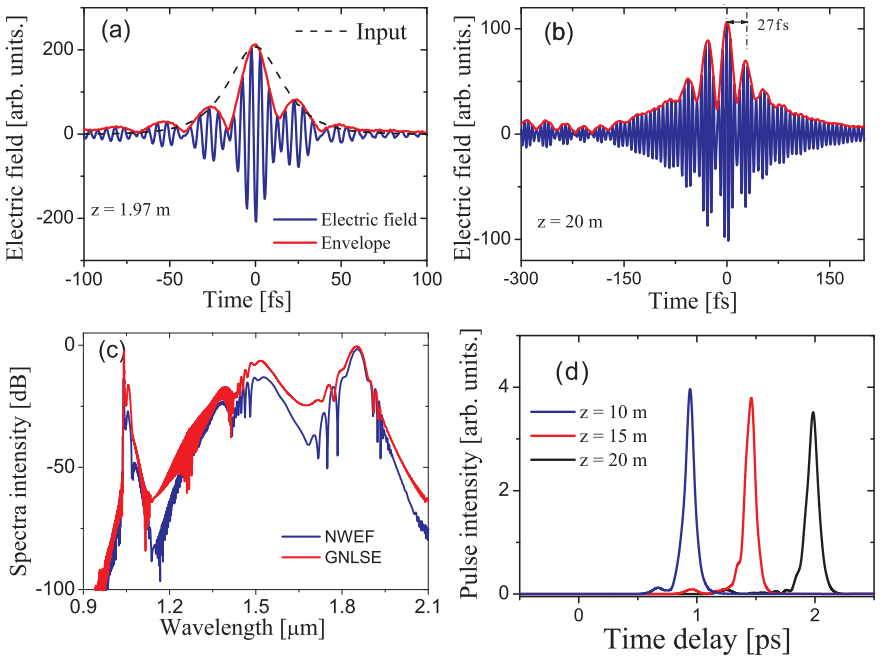

Fig. C.6: NWEF simulations on the temporal profile of the 25 fs (FWHM) single sech-shape soliton centered at 1.4 μm under the coupler-like phase profiles: (a, b) the electric field and the envelope profile of the pulses at (a) the beginning of the energy transfer, defined as the pulse most-compressed position (marked by white dashed line in Fig. C.5(a)), and at (b) the end of the 20-meter-propagation, respectively. (c) spectral comparison between the NWEF model and GNLSE model. (d) filtered out soliton wave at the transferred wavelength, the transferred soliton has a soliton length around 2.56 m, FWHM around 100 fs.

and the transferred wave at the second channel (1.85 μm) are beating during the propagation and give rise to beating modulation on the electric field of the pulses. The beating length is 27 fs, corresponding to the frequency difference between the two waves. Such beating process can only occur when the two waves always have the same group velocity, i.e. GV-matching, from the beginning of the energy transfer to the end of the propagation.

Moreover, by filtering the spectrum to isolate the transferred wave, we can investigate the alleged soliton properties of the tunneled wave: its temporal

pulse profiles at different stages of propagation are shown in Fig. C.6(d). Although there is a clear drop in the peak intensity and a slight temporal broadening during propagation, this is attributed to a relaxation effect of the soliton as it will self-adapt to the GVD profile by adjusting the pulse duration and peak intensity gradually during the propagation. Its characteristic soliton length is calculated to be 2.56 m, i.e. much shorter than the distances considered here, which supports the notion that this is a soliton. Indeed, a DW would at the same propagation distances be dramatically reduced in intensity and broadened in time due to its dispersive nature. We also checked the results by using the more commonly-used GNLSE [7] and we got very similar results, see Fig. C.6(c).

C.4 Conclusion

In conclusion, here we pointed out that a fundamental soliton eigenstate is always supported under a dispersive phase profile, in which the phase shifts on pulse induced by both the dispersion and the nonlinearity are counterbalanced. A coupler-like phase is demonstrated to support a two-peak-shape soliton eigenstate. When launching only a single sech-shape soliton corresponding to one channel of such a phase coupler, soliton coupling is expected to occur. Physically, coupler-like wave number profile implies a soliton PM condition which is beyond the commonly-known DW PM condition by including another essential premise, GV-matching condition, which means the generated DW is turned into another soliton wave. When having a leaking structure of the wave number profile, i.e. GV mismatched, the launched soliton will have a leakage-like radiation instead of transferring to another soliton, which is exactly the commonly observed DW generation. Such soliton coupling and soliton leaking effects in realistic PCF structures are also presented as vivid examples.

Bibliography

[1] N. Akhmediev and M. Karlsson, "Cherenkov radiation emitted by solitons in optical fibers," *Phys. Rev. A,* vol. 51, no. 3, pp. 2602–2607, 1995.

[2] P. Wai, C. Menyuk, Y. Lee, and H. Chen, "Nonlinear pulse propagation in the neighborhood of the zero-dispersion wavelength of monomode optical fibers," *Opt. Lett.,* vol. 11, no. 7, pp. 464–466, 1986.

[3] P. Beaud, W. Hodel, B. Zysset, and H. Weber, "Ultrashort pulse propagation, pulse breakup, and fundamental soliton formation in a single-mode optical fiber," *IEEE J. Quant. Electron.,* vol. 23, no. 11, pp. 1938–1946, 1987.

[4] A. Gouveia-Neto, M. E. Faldon, and J. Taylor, "Solitons in the region of the minimum group-velocity dispersion of single-mode optical fibers," *Opt. Lett.,* vol. 13, no. 9, pp. 770–772, 1988.

[5] F. Wise, I. Walmsley, and C. Tang, "Simultaneous formation of solitons and dispersive waves in a femtosecond ring dye laser," *Opt. Lett.,* vol. 13, no. 2, pp. 129–131, 1988.

[6] S. Stark, F. Biancalana, A. Podlipensky, and P. Russell, "Nonlinear wavelength conversion in photonic crystal fibers with three zero-dispersion points," *Phys. Rev. A,* vol. 83, no. 2, pp. 023808(5), 2011.

[7] J. Dudley, G. Genty, and S. Coen, "Supercontinuum generation in photonic crystal fiber," *Rev. Mod. Phys.,* vol. 78, no. 4, pp. 1135–1184, 2006.

[8] S. Roy, S. Bhadra, and G. Agrawal, "Effects of higher-order dispersion on resonant dispersive waves emitted by solitons," *Opt. Lett.,* vol. 34, no. 13, pp. 2072–2074, 2009.

[9] J. Yuan, X. Sang, Q. Wu, C. Yu, et al., "Efficient red-shifted dispersive wave in a photonic crystal fiber for widely tunable mid-infrared wavelength generation." *Laser Phys. Lett.,* vol. 10, no. 4, pp. 045405(5), 2013.

[10] V. Serkin, V. Vysloukh, and J. Taylor, "Soliton spectral tunnelling effect," *Electron. Lett.,* vol. 29, no. 1, pp. 12–13, 1993.

[11] V. Vysloukh, V. Serkin, A. Danileiko, and E. Samarina, "Influence of the dispersion-spectrum inhomogeneities on the Raman self-conversion of the frequency of femtosecond optical solitons," *Quant. Electron.,* vol. 25, no. 11, pp. 1095–1100, 1995.

[12] E. Tsoy and C. Sterke, "Theoretical analysis of the self-frequency shift near zero-dispersion points: Soliton spectral tunneling," *Phys. Rev. A,* vol. 76, no. 4, pp. 043804(9), 2007.

[13] B. Kibler, P. Lacourt, F. Courvoisier, and J. Dudley, "Soliton spectral tunnelling in photonic crystal fibre with sub-wavelength core defect," *Electron. Lett.,* vol. 43, no. 18, pp. 967–968, 2007.

[14] T. Belyaeva, V. Serkin, C. Hernandez-Tenorio, and F. Garcia-Santibañez, "Enigmas of optical and matter-wave soliton nonlinear tunneling," *J. Mod. Opt.,* vol. 57, no. 12, pp. 1087–1099, 2010.

[15] F. Poletti, P. Horak, and D. Richardson, "Soliton spectral tunneling in dispersion-controlled holey fibers," *Photon. Tech. Lett., IEEE* vol. 20, no. 16, pp. 1414-1416, 2008.

[16] G. Manili, A. Tonello, D. Modotto, M. Andreana, et al., "Gigantic dispersive wave emission from dual concentric core microstructured fiber," *Opt. Lett.,* vol. 37, no. 19, pp. 4101–4103, 2012.

[17] S. Wang, J. Hu, H. Guo, and X. Zeng, "Optical cherenkov radiation in an As_2S_3 slot waveguide with four zero-dispersion wavelengths," *Opt. Express,* vol. 21, no. 3, pp. 3067–3072, 2013.

[18] S. Roy, D. Ghosh, S. Bhadra, and G. Agrawal, "Role of dispersion profile in controlling emission of dispersive waves by solitons in supercontinuum generation," *Opt. Commun.,* vol. 283, no. 15, pp. 3081–3088, 2010.

[19] H. Guo, X. Zeng, and M. Bache, "Generalized nonlinear wave equation in frequency domain," *arXiv preprint,* 1301.1473, 2013.

[20] H. Guo, X. Zeng, B. Zhou, and M. Bache, "Nonlinear wave equation in frequency domain: accurate modeling of ultrafast interaction in anisotropic nonlinear media," *J. Opt. Soc. Am. B,* vol. 30, no. 3, pp. 494–504, 2013.

[21] D. Skryabin, F. Luan, J. Knight, and P. Russell, "Soliton self-frequency shift cancellation in photonic crystal fibers," *Science,* vol. 301, no. 5640, pp. 1705–1708, 2003.

[22] V. Serkin, T. Belyaeva, G. Corro, and M. Granados, "Stimulated Raman self-scattering of femtosecond pulses. I. Soliton and non-soliton regimes of coherent self-scattering," *Quant. Electron.,* vol. 33, no. 4, pp. 325–330, 2003.

[23] V. Serkin, T. Belyaeva, G. Corro, and M. Granados, "Stimulated Raman self-scattering of femtosecond pulses. II. The self-compression of Schrödinger solitons in a spectrally inhomogeneous dispersion medium," *Quant. Electron.,* vol. 33, no. 5, pp. 456–459, 2003.

Appendix D

Publications during Ph.D. Study (First Authored)

1. **H. Guo**, B. Zhou, X. Zeng, and M. Bache, "Highly coherent mid-IR supercontinuum by self-defocusing solitons in lithium niobate waveguides with all-normal dispersion," Opt. Express **22**, 12211-12225 (2014).

2. **H. Guo**, X. Zeng, B. Zhou, and M. Bache, "Few-cycle solitons and supercontinuum generation with cascaded quadratic nonlinearities in unpoled lithium niobate ridge waveguides," Opt. Lett. **39**, 1105-1108 (2014).

3. **H. Guo**, S. Wang, X. Zeng, and M. Bache, "Understanding Soliton Spectral Tunneling as a Spectral Coupling Effect," IEEE Photon. Technol. Lett. **25**, 1928-1931 (2013).

4. **H. Guo**, X. Zeng, B. Zhou, M. Bache, H. Guo, X. Zeng, B. Zhou, and M. Bache, "Nonlinear wave equation in frequency domain: accurate modeling of ultrafast interaction in anisotropic nonlinear media," J. Opt. Soc. Am. B **30**, 494-504 (2013).

5. **H. Guo**, X. Zeng, and M. Bache, "Generalized Nonlinear Wave Equation in Frequency Domain," arXiv preprint, 1301.1473 (2013).

6. **H. Guo**, X. Zeng, B. Zhou, M. Bache, "Critical Boundary of Cascaded Quadratic Soliton Compression in PPLN," in CLEO Technical Digest (Optical Society of America, 2012), paper JW4A.45.

7. **H. Guo**, X. Zeng, B. Zhou, and M. Bache, "Near- and Mid-IR Few-cycle Self-defocusing Soliton Compression in PPLN Waveguide," in 2013 Conference on Lasers and Electro-Optics - International Quantum Electronics Conference, (Optical Society of America, 2013), paper CD_11_3.

8. **H. Guo**, X. Zeng, B. Zhou, and M. Bache, "Soliton Delay Driven by Cascading and Raman Responses," in 2013 Conference on Lasers and Electro-Optics - International Quantum Electronics Conference, (Optical Society of America, 2013), paper IF_P_9.

9. **H. Guo**, B. Zhou, X. Zeng, and M. Bache, "Experiments on Cascaded Quadratic Soliton Compression in Unpoled LN Waveguide," in CLEO: 2014, OSA Technical Digest (Optical Society of America, 2014), paper JTu4A.14.

10. **H. Guo**, X. Zeng, B. Zhou, and M. Bache, "Low-energy Self-defocusing Soliton Compression at Optical Communication Wavelengths in Unpoled

Lithium Niobate Ridge Waveguide," in CLEO: 2014, OSA Technical Digest (Optical Society of America, 2014), paper SW1E.4.